Numerički proračun performansi rotora NASA 67

Žužul, Josip

Master's thesis / Diplomski rad

2017

Degree Grantor / Ustanova koja je dodijelila akademski / stručni stupanj: **University of Zagreb, Faculty of Mechanical Engineering and Naval Architecture / Sveučilište u Zagrebu, Fakultet strojarstva i brodogradnje**

Permanent link / Trajna poveznica: https://urn.nsk.hr/urn:nbn:hr:235:942499

UNIVERSITY OF ZAGREB
Faculty of Mechanical Engineering and Naval Architecture

MASTER’S THESIS

Josip Žužul

Zagreb, 2017

UNIVERSITY OF ZAGREB
Faculty of Mechanical Engineering and Naval Architecture

NUMERICAL EVALUATION OF THE PERFORMANCE CURVE FOR THE NASA ROTOR 67

Supervisor:
Prof. Hrvoje Jasak, PhD

Student:
Josip Žužul

Zagreb, 2017

I hereby declare that this thesis is entirely the result of my own work except where otherwise indicated. I have fully cited all used sources and I have only used the ones given in the list of references.

I would like to express my sincere gratitude to Professor Hrvoje Jasak for being the supervisor of the thesis. Without his assistance, encouragement and valuable comments, this thesis would not be possible.

I am truly thankful to Gregor Cvijetić, whose suggestions, comments and creativity during the work on the thesis will never be forgotten. He significantly contributed to the successful completion of the thesis.

I would also like to thank my friends and colleagues for all the support and encouragement during the work on the thesis. Special thanks goes to my colleagues from the 8th floor for the positive work environment with numerous discussions and plenty of fun times. It was my pleasure to be a part of the 8th floor CFD group.

Finally, I would like to thank to my family and especially to my girlfriend Maša for all the support, patience and understanding during the work on the thesis.

Thank you all,
Josip Žužul

SVEUČILIŠTE U ZAGREBU
FAKULTET STROJARSTVA I BRODOGRADNJE
Središnje povjerenstvo za završne i diplomske ispite
Povjerenstvo za diplomske ispite studija strojarstva za smjerove:
procesno-energetski, konstrukcijski, brodostrojarski i inženjersko modeliranje i računalne simulacije

Sveučilište u Zagrebu Fakultet strojarstva i brodogradnje	
Datum	Prilog
Klasa:	
Ur.broj:	

DIPLOMSKI ZADATAK

Student: **Josip Žužul** Mat. br.: 0035188132

Naslov rada na hrvatskom jeziku: **Numerički proračun performansi rotora NASA 67**

Naslov rada na engleskom jeziku: **Numerical evaluation of the performance curve for the NASA Rotor 67**

Opis zadatka:
Numerical simulation of steady turbulent compressible flow in rotating turbomachinery using OpenFOAM has proven to be challenging for a number of years. For stable, efficient and accurate simulations, it is necessary to set up the correct combination of numerous numerical parameters, including handling of the multiple rotating frames of reference, choice of the energy equation, boundary conditions and numerical discretisation parameters.

In this study, compressible turbulent flow in the NASA Rotor 67 axial-flow fan shall be simulated using the new formulation of the compressible flow solver. The objective of the study is to assemble the performance curve giving total pressure ratio as a function of the mass flow rate for a given rotational speed.

The candidate shall perform the following tasks within this project:

- describe a CFD model capable of simulating steady turbulent compressible transonic flow in rotating turbomachinery,
- collect the available experimental and reference numerical data for the NASA Rotor 67 geometry,
- prepare a computational mesh for the NASA Rotor 67 geometry (rotor only) using Pointwise meshing software,
- perform simulations of the flow through the fan stage at 16043 RPM for two operating points (one at nominal conditions and one close to stall conditions), selected based on the available experimental data. Describe the results in terms of mass flow, total pressure ratio, fan torque, axial force, power and efficiency,
- illustrate the details of the flow at various radial and axial sections and the flow in the tip gap. If possible, compare the detailed flow results against available experimental or reference numerical data;
- if possible, perform flow simulations at additional operating points at the same angular velocity in order to assemble a single fan performance curve for a given angular velocity.

The Thesis shall list the bibliography and any assistance received during this study.

Zadatak zadan: Rok predaje rada: Predviđeni datumi obrane:
19. siječnja 2017. 23. ožujka 2017. 29., 30. i 31. ožujka 2017.

Zadatak zadao: Predsjednica Povjerenstva:

Prof. dr. sc. Hrvoje Jasak Prof. dr. sc. Tanja Jurčević Lulić

Table of Contents

List of Figures

List of Tables

Nomenclature

Greek letters

σ	Cauchy Stress Tensor	Pa
τ	Viscous stress tensor	Pa
γ	Diffusion coefficient	m^2 / s^2
$\Gamma_{\omega,\mathrm{eff}}$	Effective diffusivity of specific turbulence dissipation rate	m^2 / s
$\Gamma_{\mathrm{k,eff}}$	Effective diffusivity of turbulence kinetic energy	m^2 / s
λ	Thermal conductivity	W / (m K)
μ	Dynamic viscosity	Pa s
ν	Molecular kinematic viscosity	m^2 / s
ω	Angular velocity; Eddy turn-over time	s^{-1}
Φ	Arbitrary turbulent quantity	-
ϕ	Transported scalar variable	-
Φ''	Fluctuating component of an arbitrary turbulent quantity	-
ψ	Compressibility	s^2 / m^2
ρ	Fluid density	kg / m^3
$\widetilde{\Phi}$	Favre-Averaged arbitrary turbulent quantity	-
μ_{t}	Turbulent (eddy) viscosity	Pa s
η_{ad}	Adiabatic efficiency	-
κ	Specific heat ratio	-
Π	Total pressure ratio	-

Latin letters

$\dot{m}$	Mass flow rate	kg/s
$\mathbf{g}$	Gravitational acceleration	m / s^2

$\mathbf{I}$	Identity (unit) tensor	-
$\mathbf{R}$	Reynolds Stress Tensor	Pa
$\mathbf{u}$	Velocity vector	m / s
$\mathbf{u}_{\mathrm{rel}}$	Relative velocity vector	m / s
$\widetilde{\mathbf{u}}$	Favre-Averaged velocity	m / s
e	Total specific energy	J / kg
e_{M}	Mechanical (kinetic) energy	J / kg
F_1	Blending Function	-
F_{23}	Blending Function	-
F_2	Blending Function	-
F_3	Optional term for rough wall flows	-
i	Rothalpy	J / kg
k	Turbulent kinetic energy	m^2 / s^2
p	Static pressure	Pa
q_v	Volumetric sources and sinks of the scalar field	-
R	Individual gas constant	J / (kg K)
r	Radius	m
S_{H}	Source term of enthalpy	W / m^3
T	Static temperature	K
t	Time	s
u	Internal (thermal) energy	J / kg
u_{Θ}	Tangential component of the absolute velocity vector	m / s
y	Distance to wall	m
$\boldsymbol{A}$	Antisymmetric part of the velocity gradient tensor	s^{-1}

$\boldsymbol{S}$	Symmetric part of the velocity gradient tensor	s^{-1}
a	Speed of sound	m / s
F	Axial force	N
I	Turbulence intensity	-
M	Mach number	-
M_{rel}	Relative Mach number	-
N	Number of rotor blades	-
P	Power	W
p_0	Total pressure	Pa
p_{ref}	Reference pressure	Pa
Q	Q-contour	s^{-1}
T_{F}	Fan torque	N m
T_0	Total temperature	K
T_{ref}	Reference temperature	K
u_{tip}	Blade tip velocity	m/s
n	Rotational speed	rpm

Abbreviations

CAD	Computer Aided Design
CFD	Computational Fluid Dynamics
GGI	General Grid Interface
MRF	Multiple Reference Frame
NASA	National Aeronautics and Space Administration
PDE	Partial Differential Equation
RANS	Reynolds Averaged Navier-Stokes Equations
SST	Shear Stress Transport
LES	Large Eddy Simulation
DNS	Direct Numerical Simulation

Abstract

Computational Fluid Dynamics (CFD) is nowadays frequently used for the analysis of complex fluid flows for industrial and academic purposes. In order to improve and expand CFD codes which are capable of solving wide range of physical phenomena, new code formulations have to be developed and validated on a large number of test cases with comprehensive experimental data. Within this thesis, a new formulation of compressible, turbulent flow solver for rotating turbomachinery, implemented in open-source CFD package `foam-extend` is tested. For problems of emphasized transonic and compressible character of a flow in rotating turbomachinery, commonly used test case is a transonic NASA Rotor 67 axial-flow turbofan, due to the availability of detailed experimental data provided by National Aeronautics and Space Administration (NASA).

In order to perform numerical simulations of the NASA Rotor 67, a case needs to be prepared within the preprocessing steps which include geometry and mesh generation. As a first step, geometry in terms of 3D Computer Aided Design (CAD) model is generated using a Solidworks CAD software. The created CAD model is a basis for the second step - generation of a spatially discretised grid of finite volumes, which was done using a meshing software Pointwise. Since NASA Rotor 67 turbofan has 22 equally spaced blades, only one blade passage is examined in order to reduce computational cost. This can be done by using a special, cyclic and periodic boundary condition which require identical cyclic mesh boundaries. Because of highly twisted rotor blades and cyclic boundary condition requirement, generated mesh is commonly of insufficient quality. Thus, to avoid bad mesh quality and to carry out a simulation for a single blade passage, the General Grid Interface (GGI) is used within the `foam-extend` CFD package. GGI allows the use of the non-conformal mesh boundaries in order to overcome grid quality issues.

After successfully accomplished preprocessing steps, a number of numerical simulations is performed with the so-called "frozen rotor" approach in order to assemble a performance curve for NASA Rotor 67 turbofan at the nominal angular velocity. Results are presented in terms of graphical representations of flow field quantities at various sections of the domain. Furthermore, overall computed turbofan characteristics like power, efficiency, mass flow and total pressure ratio are also shown.

Additionally, a basic working principle of turbocompressors and turbofans is presented along with the restrictions for stable operating range. Furthermore, an overview of common instabilities which occur in turbocompressors is also given. Finally, the adequate formulation of a CFD model capable of solving turbulent, transonic and compressible flow is presented.

Keywords: *CFD*, *foam-extend*, *Transonic Turbofan*, *NASA Rotor 67*, *Mesh Generation*, *CAD Generation*

Sažetak (Abstract in Croatian)

Računalna dinamika fluida danas je neizostavni segment analize kompleksnih strujanja fluida, kako za industrijske, tako i za akademske svrhe. Kako bi se povećala primjenjivost numeričkih kódova za rješavanje širokog spektra problema moderne fizike, potrebno je razvijati nove formulacije kódova koje se potom validiraju na velikom broju testnih simulacija s poznatim detaljnim eksperimentalnim podacima. U sklopu ovog rada, testirana je nova formulacija numeričkog kôda za stlačivo, turbulentno strujanje u rotirajućim turbostrojevima, implementirana u sklopu softverskog paketa `foam-extend`. Za probleme s izraženim transoničnim i kompresibilnim karakterom strujanja u turbostrojevima, često korišten testni primjer je aksijalni NASA Rotor 67 turboventilator zbog dostupnosti detaljnih eksperimentalnih podataka od NASA-e.

Kako bi se provela numerička simulacija NASA Rotora, potrebno je prethodno izraditi 3D model NASA Rotor 67 turboventilatora, te izraditi mrežu konačnih volumena. 3D CAD model turboventilatora izrađen je u softverskom paketu SolidWorks. CAD model je temelj sljedeće faze, a to je izrada prostorno diskretizirane mreže konačnih volumena u softverskom paketu Pointwise. Zbog činjenice da NASA Rotor 67 turboventilator ima 22 rotorske lopatice, analiziran je jedan međulopatični prolaz s namjerom reduciranja računalnih resursa. Uobičajena metoda je korištenje posebnog periodičkog rubnog uvjeta koji zahtijeva konformne periodičke mreže. Kako zbog velikog uvijanja lopatice po visini, tako i zbog zahtjeva konformne mreže na periodičnim granicama, izrađena mreža je često nedovoljne kvalitete. Stoga je u svrhu izbjegavanja mreže loše kvalitete i provedbe simulacije u jednom međulopatičnom prolazu, korišteno tzv. *General Grid Interface* (GGI) sučelje unutar softverskog paketa `foam-extend`. GGI sučelje omogućava korištenje nekonformnih mreža na periodičkim granicama kako bi se prevladali problemi neadekvatne mreže u međulopatičnim prolazima.

Kako bi se izradila radna karakteristika NASA Rotora na nominalnoj brzini vrtnje, potrebno je provesti veći broj numeričkih simulacija. Rezultati su prezentirani u vidu grafičkih prikaza fizikalnih veličina na različitim presjecima unutar domene. Prezentirane su i globalne karakteristike poput snage, iskoristivosti, masenog protoka i omjera totalnog tlaka.

Dodatno je dan kratak pregled osnovnih principa rada turbokompresora i turboventilatora uz osvrt na ograničenja za stabilan režim rada. Prikazan je i kratak pregled čestih nestabilnosti koje se pojavljuju prilikom strujanja u turbokompresorima. Cjelokupni rad zaokružen je prikazom korištene formulacije matematičkog modela za numeričko rješavanje kompleksnih režima strujanja kao što je stlačivo, turbulentno i transonično strujanje u turbostrojevima.

Ključne riječi: *CFD*, *foam-extend*, *Transonični turboventilator*, *NASA Rotor 67*, *Generiranje mreže konačnih volumena*, *3D CAD modeliranje*

Prošireni sažetak (Extended Abstract in Croatian)

U sklopu ovog rada provedene su numeričke simulacije strujanja u međulopatičnom kanalu transoničnog aksijalnog turboventilatora NASA Rotor 67 pomoću nove inačice numeričkog rješavača za stlačiva, transonična i turbulenta strujanja fluida u turbostrojevima. Numerički proračun proveden je unutar softverskog paketa `foam-extend`, specijaliziranog za računalnu analizu strujanja fluida.

Uvod

Implementacija novih formulacija numeričkih kódova za rješavanje strujanja fluida iziskuje proces validacije na velikom broju testnih simulacija s ciljem usporedbe rezultata dobivenih numeričkim postupkom s rezultatima eksperimenta. Kod turbostrojeva s izraženim transoničnim i turbulentnim karakterom strujanja, jedan od najčešće korištenih testnih primjera je NASA Rotor 67 transonični aksijalni turboventilator zbog javno dostupnih detaljnih eksperimentalnih podataka od strane NASA-e. Ideja rada je provesti numerički proračun unutar paketa `foam-extend` pomoću nove formulacije numeričkog rješavača za stlačiva strujanja u turbostrojevima (`steadyCompressbileMRFFoamRothalpy`), koji energetsku jednadžbu rješava korištenjem rotalpije kao konzervacijske veličine. Kako bi se stvorili uvjeti za provođenje numeričkog proračuna, prethodno je potrebno definirati 3D model opstrujavanog ventilatora u odgovarajućem CAD paketu te na temelju generirane geometrije kreirati prostorno diskretiziranu mrežu konačnih volumena. Provedene su numeričke simulacije za dvije radne točke - radna točka koju karakterizira najveća iskoristivost te radna točka u blizini zastoja strujanja. Rezultati provedenih numeričkih proračuna prezentirani su u vidu grafičkih prikaza fizikalnih veličina na različitim presjecima unutar domene. Dodatno, prezentirane su i globalne karakteristike turboventilatora: snaga, iskoristivost, maseni protok i prirast totalnog tlaka.

Matematički model

Matematički model kojim se opisuje strujanje stlačivog fluida definiran je jednadžbom očuvanja mase, jednadžbom očuvanja količine gibanja te jednadžbom očuvanja energije. U sklopu ovog rada korišten je numerički rješavač koji koristi modificiranu energetsku jednadžbu na način da je jednadžba očuvanja energije prezentirana u vidu očuvanja rotalpije. Rotalpija je termodinamička veličina karakteristična za stlačivi fluid koja je konzervirana unutar reda rotorskih lopatica, odnosno reda statorskih lopatica, ali nije konzervirana unutar stupnja. Efekt rotacije je uzet u obzir korištenjem engl. *Multiple Reference Frames* metode (MRF metode), koja podrazumijeva uvođenje dodatnih članova u jednadžbu očuvanja količine gibanja. Takav pristup omogućava korištenje nepomične numeričke mreže u prostoru bez uvođenja rotacije mreže što smanjuje računalno vrijeme potrebno za provedbu numeričkog proračuna. Konzervacijske jednadžbe su stoga prikazane u skladu s MRF modelom:

- jednadžba očuvanja mase

$$\frac{\partial \rho}{\partial t} + \nabla \bullet (\rho \mathbf{u}) = 0, \tag{1}$$

- jednadžba očuvanja količine gibanja

$$\frac{\partial (\rho \mathbf{u})}{\partial t} + \nabla \bullet (\rho \mathbf{u}_{\mathrm{rel}} \otimes \mathbf{u}) + \boldsymbol{\omega} \times (\rho \mathbf{u}) = -\nabla p + \nabla \bullet \boldsymbol{\tau} + \rho \mathbf{g}, \tag{2}$$

- jednadžba očuvanja energije (konzervacija rotalpije)

$$\nabla \bullet (\rho i \mathbf{u}_{\mathrm{rel}}) = -\nabla \bullet (\rho \omega r u_{\Theta} \mathbf{u}_{\mathrm{rel}}) - \nabla \bullet (p \mathbf{u}) + \nabla \bullet (\boldsymbol{\tau} \cdot \mathbf{u}) + \nabla \bullet (\lambda \nabla T) + S_{\mathrm{H}}. \tag{3}$$

Kako bi se riješio navedeni sustav jednadžbi potrebno je uvesti još jednu dodatnu, konstitutivnu relaciju za povezivanje gustoće s ostatkom sustava. U tu svrhu koristi se jednadžba stanja idealnog plina,

$$\rho = \frac{p}{RT} = \psi p. \tag{4}$$

Kod geometrija s periodičkim elementima kao što je slučaj turboventilatora NASA Rotor 67, često korišten pristup je generiranje numeričke mreže koja opisuje strujanje unutar jednog međulopatičnog kanala. Na taj se način drastično reduciraju zahtijevani računalni resursi za provedbu numeričke simulacije, pri čemu točnost rezultata nije smanjenja. S obzirom da su rotorske lopatice aksijalnih turbostrojeva često značajno uvinute po visini, generirane numeričke mreže su najčešće nedovoljne kvalitete. Iz tog su razloga generirane nekonformne površinske mreže na granicama domene čime je povećavana kvaliteta volumenske mreže, dok su granice povezane pomoću interpolacijskog sučelja za nekonformne mreže. Stoga je u svrhu poboljšanja kvalitete numeričke mreže korišteno sučelje za povezivanje nekonformnih mreža unutar paketa `foam-extend` - `ggi` sučelje, odnosno njena inačica za površinske mreže na periodičkim geometrijama tzv. `cyclicGgi` sučelje. Prikaz `cyclicGgi` sučelja je dan na Slici (1).

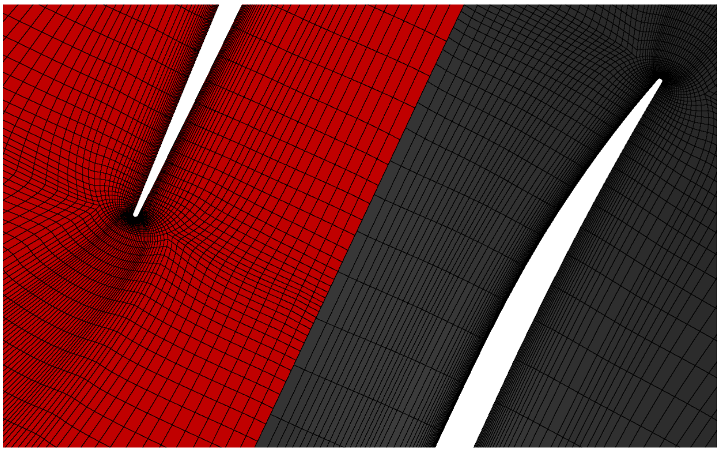

Slika 1: `cyclicGgi` sučelje za povezivanje periodičkih nekonformnih mreža.

NASA Rotor 67

NASA Rotor 67 je aksijalni, transonični turboventilator koji je razvijen u cilju ispitivanja trodimenzionalnih aerodinamičkih fenomena u turbostrojevima velikih brzina vrtnje. Na njemu su provedena eksperimentalna ispitivanja te su poznati detaljni parametri toka, kao i geometrija lopatica te strujnog kanala. NASA Rotor 67 turboventilator prikazan je na Slici (2).

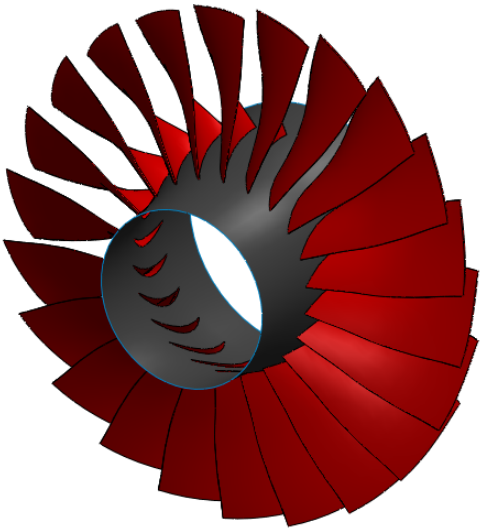

Slika 2: CAD model NASA Rotor 67 transoničnog turboventilatora.

Turboventilator ima 22 lopatice te radi na nominalnoj brzini od 16 043 okretaja u minuti. Pritom je ostvareni nominalni maseni protok od 33,25 kg/s s pripadajućim omjerom totalnog tlaka od 1,63. Na ulazu u turboventilator referentni totalni tlak i totalna temperatura iznose 101 325 Pa i 288,15 K. Obodna brzina na vrhu lopatice iznosi 429 m/s, dok je pripadajući relativni Machov broj 1,38. Između rotorske lopatice i kućišta nalazi se zazor od približno 1 mm koji je izvor gubitaka zbog prestrujavanja. Promjer kućišta na ulazu u domenu iznosi 0,514 m, dok na izlazu iznosi 0,485 m. S druge strane, promjer bubnja na ulazu iznosi 0,193 m, dok je na izlazu iz domene 0,232 m. Adijabatska iskoristivost turboventilatora u nominalnoj radnoj točki iznosi 93%.

Generacija geometrije i numeričke domene

Geometrija 3D modela NASA Rotora generirana je unutar Solidworks CAD paketa prema podacima prezentiranima u NASA-inom ispitivanju. Na Slici (3a) prikazana je geometrija rotorske lopatice i bubnja, dok je na Slici (3b) prikazana kompletna geometrija analiziranog međulopatičnog kanala koja predstavlja osnovu za generiranje prostorno diskretizirane mreže konačnih volumena.

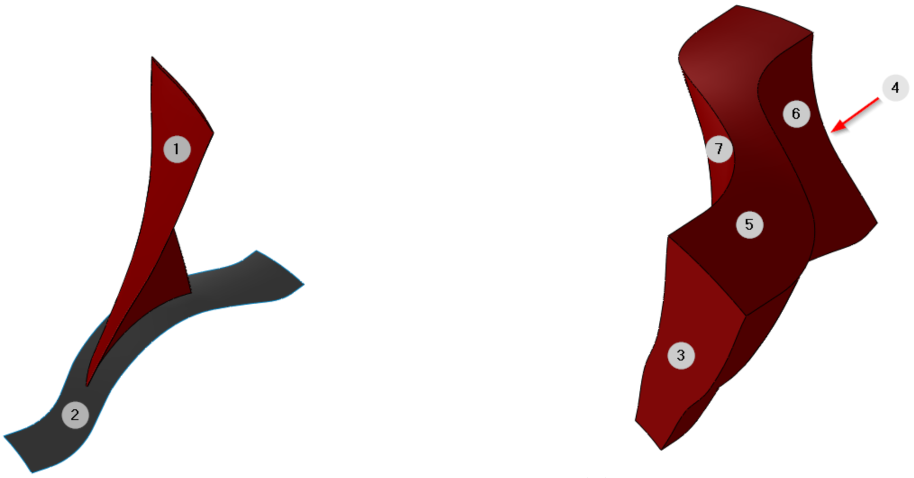

(a) Rotorska lopatica i bubanj.

(b) Kompletna geometrija NASA Rotora 67.

Slika 3: 3D geometrijski model aksijalnog turboventilatora NASA Rotor 67.

Na temelju izrađene geometrije generirana je numerička mreža u softverskom paketu Pointwise. Generirana je u potpunosti strukturirana heksaedarska mreža koju karakterizira veća točnost numeričkih rezultata s obzirom na nestrukturiranu numeričku mrežu. U sklopu ovog rada mreža je generirana ručno. Slika (4a) prikazuje površinsku mrežu na pretlačnoj strani rotorske lopatice, dok je na Slici (4b) prikazan detalj numeričke mreže u zazoru između rotorske lopatice i kućišta u neposrednoj blizini napadnog brida lopatice. Kako je u sklopu ovog rada između ostalog potrebno napraviti i analizu strujanja u zazoru, generirana je fina mreža koju čini 20 redova ćelija unutar zazora od približno 1 mm.

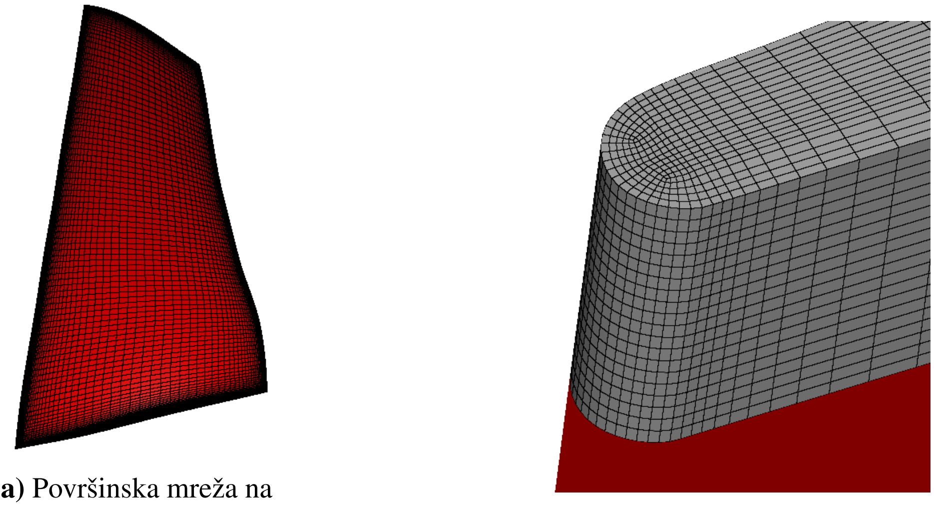

(a) Površinska mreža na rotorskoj lopatici.

(b) Detalj mreže u zazoru kod napadnog brida.

Slika 4: Prikaz generirane numeričke mreže NASA Rotor 67 turboventilatora.

U skladu s numeracijom danom na Slici (3), u Tablici (1) su deklarirani nazivi fizikalnih rubnih uvjeta generirane numeričke domene.

Tablica 1: Deklaracija granica numeričke mreže.

Patch ID	Patch name	Patch type
1	rotorBlade	`wall`
2	hub	`wall`
3	inlet	`patch`
4	outlet	`patch`
5	shroud	`wall`
6	rotorCyclic1	`cyclicGgi`
7	rotorCyclic2	`cyclicGgi`

Površinska numerička mreža na kućištu prikazana je na Slici (5). Budući da volumenska mreža prati konturu površinske mreže na kućištu, dodatni presjeci mreže nisu prikazivani. Slika (5b) prikazuje detalj površinske numeričke mreže oko napadnog brida rotorske lopatice. Uz samu lopaticu generirano je 20 finih redova ćelija (prikazano na Slici (5) sivom bojom) kako bi se numeričkim proračunom obuhvatili svi važniji detalji strujanja.

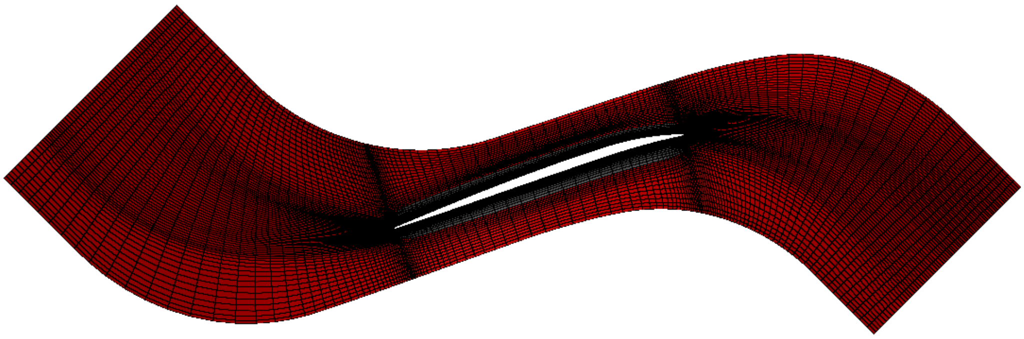

(a) Prikaz numeričke mreže na kućištu.

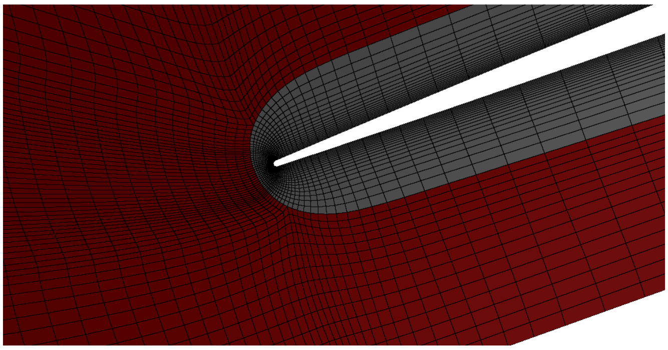

(b) Detalj numeričke mreže kod napadnog brida rotorske lopatice (na kućištu).

Slika 5: Prikaz generirane površinske numeričke mreže na kućištu NASA Rotor 67 turboventilatora.

Prezentirana numerička mreža korištena je za provedbu numeričkih simulacija za sve radne točke u sklopu ovog rada. Mreža zadovoljava sve kriterije kvalitete prema alatu `checkMesh` u sklopu paketa `foam-extend`.

Rubni uvjeti

Kako bi se sustav parcijalnih diferencijalnih jednadžbi koje opisuju strujanje fluida jednoznačno riješio, potrebno je zadati rubne uvjete na rubovima numeričke domene. Rubni uvjeti korišteni za sve numeričke simulacije unutar ovog rada prezentirani su u Tablici (2). Kako su u sklopu rada provedene numeričke simulacije strujanja u više radnih točaka, potrebno je naglasiti da su razne radne točke dobivene promjenom raspodjele mapiranog statičkog tlaka na `outlet` granici. Osim rubnih uvjeta prezentiranih u Tablici (2), korišteni su i rubni uvjeti `turbulentIntensityKineticEnergyInlet` na `inlet` i `outlet` granici za kinetičku energiju turbulencije te `turbulentMixingLengthFrequencyInlet` na `inlet` i `outlet` granici za polje specifične disipacije kinetičke energije turbulencije.

Tablica 2: Korišteni rubni uvjeti za tlak, brzinu, rotalpiju i temperaturu.

Patch	**Pressure BC**	**Velocity BC**	**Rothalpy BC**	**Temperature BC**
rotorBlade	`zeroGradient`	`fixedValue`	`zeroGradient`	`zeroGradient`
hub	`zeroGradient`	`fixedValue`	`zeroGradient`	`zeroGradient`
inlet	ITP	PDIOV	`fixedValue`	ITT
outlet	TVMFV	`inletOutlet`	`inletOutlet`	`inletOutlet`
shroud	`zeroGradient`	`fixedValue`	`zeroGradient`	`zeroGradient`
rotorCyclic1	`cyclicGgi`	`cyclicGgi`	`cyclicGgi`	`cyclicGgi`
rotorCyclic2	`cyclicGgi`	`cyclicGgi`	`cyclicGgi`	`cyclicGgi`

TVMFV – `timeVaryingMappedFixedValue`,
PDIOV – `pressureDirectedInletOutletVelocity`,
ITP – `isentropicTotalPressure`,
ITT – `isentropicTotalTemperature`.

Nominalna radna točka

Rezultati numeričke simulacije NASA Rotora 67 u nominalnoj radnoj točki prezentirani su u vidu usporedbe kontura relativnog Machovog broja na presjecima visine raspona od 10%, 30% i 70% s rezultatima eksperimenta. Usporedbe kontura relativnog Machovog broja za nominalnu radnu točku mogu se vidjeti na Slikama (6), (7) i (8). Može se primijetiti kako se radi o dobrom slaganju vrijednosti relativnog Machovog broja.

Budući da su polja strujanja relativno slična, biti će prikazana samo polja strujanja na visini raspona od 10% od kućišta. Prikazane su slike polja tlaka i temperature - Slika (9), brzine i relativnog Machovog broja - Slika (10) te kinetičke energije turbulencije i turbulentne viskoznosti - Slika (11). Polje temperature prati konture tlaka što je u skladu s jednadžbom stanja idealnog plina. S obzirom na konture relativnog Machovog broja, strujanje na ulazu je nadzvučno, kroz međulopatični kanal je transonično, dok je na izlazu podzvučno. U slučaju opisa strujanja shodno vrijednosti Machovog broja (definiranog na temelju magnitude vektora apsolutne brzine), strujanje je na ulazu podzvučno, kroz međulopatični kanal transonično te na izlazu podzvučno. Na temelju prikaza polja kinetičke energije turbulencije i turbulentne viskoznosti može se jasno uočiti vrtložni trag.

(a) Eksperiment [1]. **(b)** Numerička simulacija.

Slika 6: Usporedba kontura relativnog Machovog broja između eksperimenta i numeričke simulacije na presjeku visine raspona od 10% za nominalnu radnu točku.

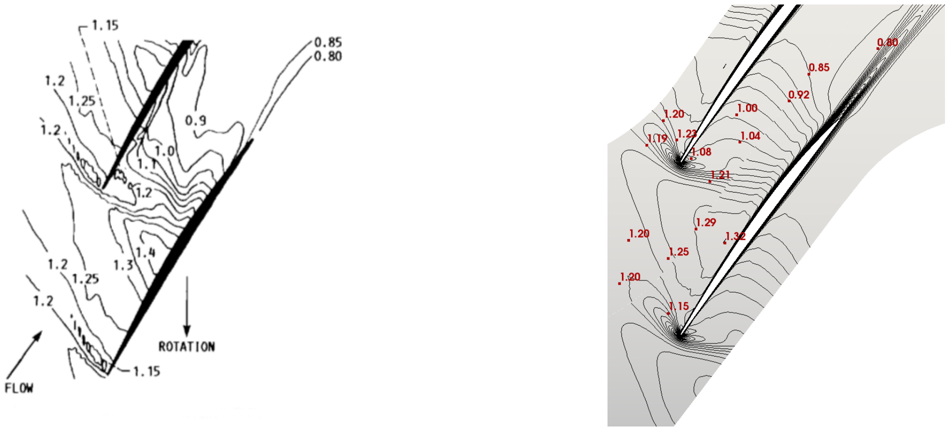

(a) Eksperiment [1]. **(b)** Numerička simulacija.

Slika 7: Usporedba kontura relativnog Machovog broja između eksperimenta i numeričke simulacije na presjeku visine raspona od 30% za nominalnu radnu točku.

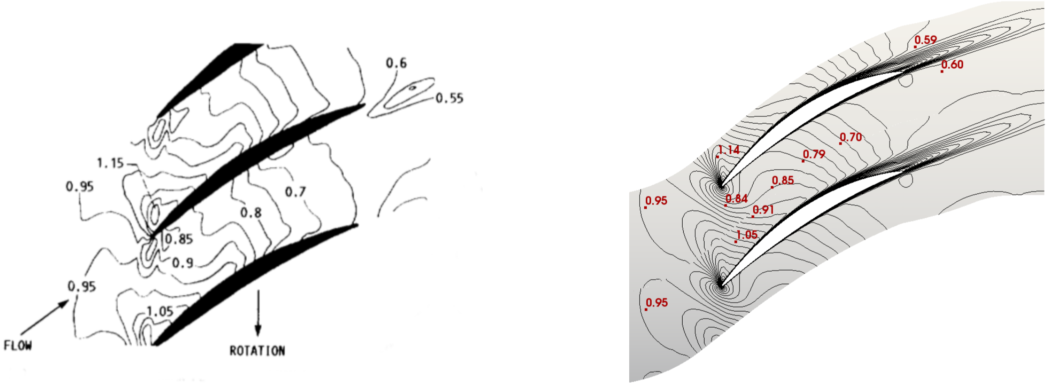

(a) Eksperiment [1]. **(b)** Numerička simulacija.

Slika 8: Usporedba kontura relativnog Machovog broja između eksperimenta i numeričke simulacije na presjeku visine raspona od 70% za nominalnu radnu točku.

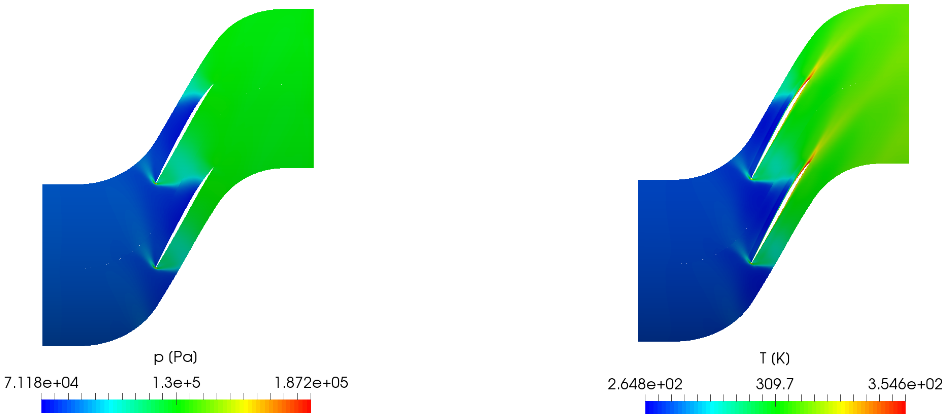

(a) Polje tlaka. **(b)** Polje temperature.

Slika 9: Polje tlaka i temperature na presjeku visine raspona od 10% za nominalnu radnu točku.

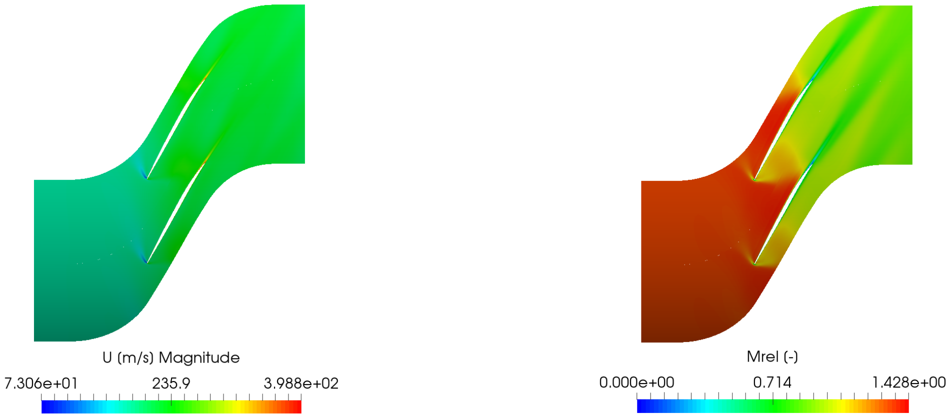

(a) Polje brzine. **(b)** Polje relativnog Machovog broja.

Slika 10: Polje brzine i relativnog Machovog broja na presjeku visine raspona od 10% za nominalnu radnu točku.

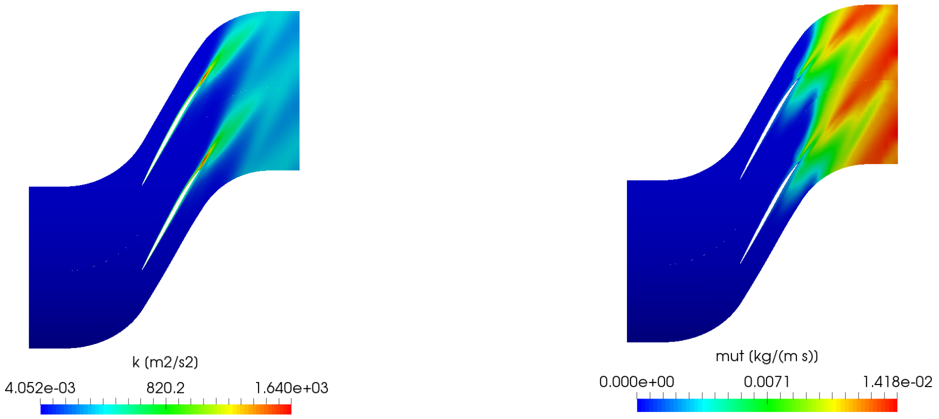

(a) Polje kinetičke energije turbulencije. **(b)** Polje turbulentne viskoznosti.

Slika 11: Polje kinetičke energije turbulencije i turbulentne viskoznosti na presjeku visine raspona od 10% za nominalnu radnu točku.

Prestrujavanje fluida s pretlačne na potlačnu stranu te vrtlog na vrhu lopatice prikazan je na Slici (12) pomoću strujnica.

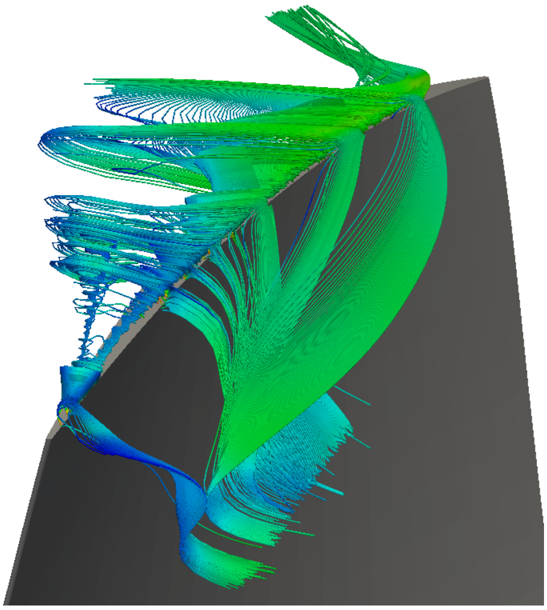

Slika 12: Prikaz prestrujavanja i vrtloga na vrhu lopatice pomoću pomoću strujnica za radnu točku s najvećom iskoristivošću.

Vrtlog na izlaznom bridu rotorske lopatice prikazan pomoću Q-kontura je dan na Slici (13).

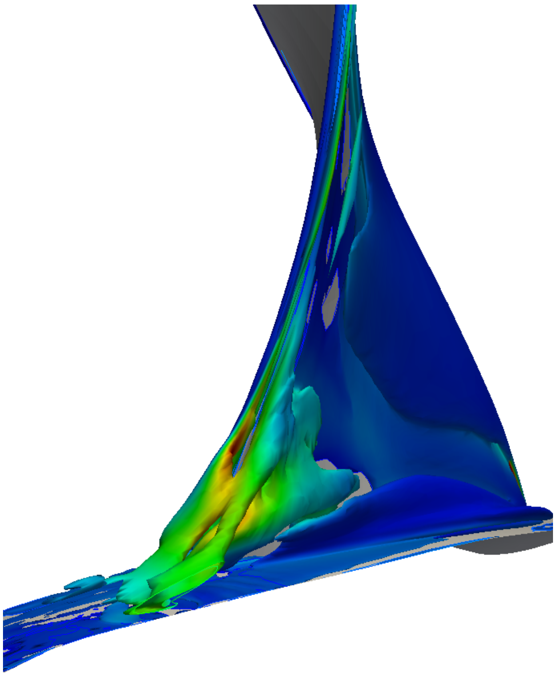

Slika 13: Vizualizacija vrtloga na izlaznom bridu rotorske lopatice pomoću Q-konture za nominalnu radnu točku.

Vrtlog na izlaznom bridu rotorske lopatice prikazan pomoću strujnica je dan na Slici (14).

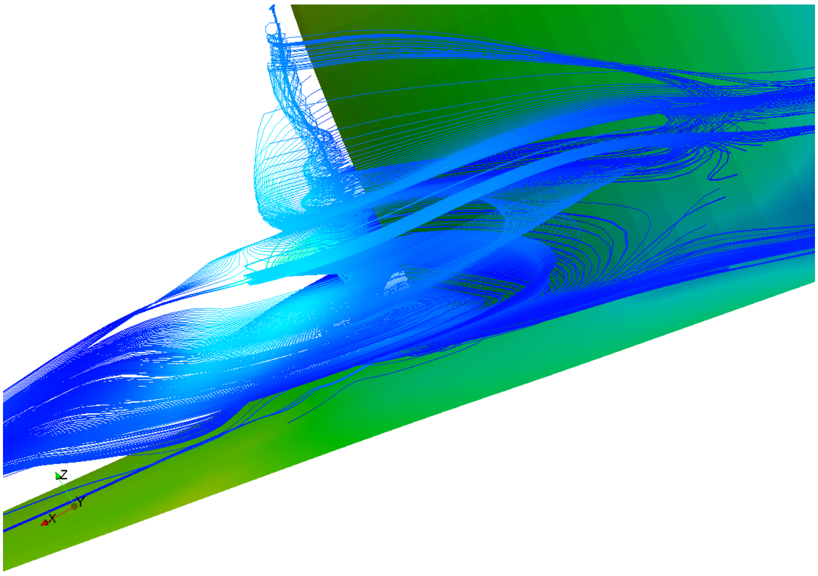

Slika 14: Vizualizacija vrtloga na izlaznom bridu rotorske lopatice pomoću strujnica za nominalnu radnu točku.

Provedbom numeričke simulacije strujanja u NASA Rotor 67 turboventilatoru za nominalnu radnu točku dobivene su radne performanse NASA Rotora te su prikazane u Tablici (3). Usporedbom numeričkih rezultata i eksperimenta zaključuje se da su numerički rezultati u dobrom slaganju s eksperimentom.

Tablica 3: Performanse NASA Rotora 67 u nominalnoj radnoj točki.

Parametar	**Vrijednost**	**Eksperiment**	**Greška**	**Relativna pogreška, [%]**
Maseni protok, $\dot{m}$	33,65 kg/s	34,573 kg/s	0,923 kg/s	2,67
Omjer totalnih tlakova, Π	1,6148	1,642	0,0272	1,66
Zakretni moment, T_F	42,9 N m	/	/	/
Aksijalna sila, F	-172,4 N	/	/	/
Snaga, P	72 020 W	/	/	/
Adijabatska iskoristivost, η_ad	90,03%	93%	2,97%	3,19

Radna točka u blizini zastoja strujanja

Rezultati numeričke simulacije NASA Rotora 67 u radnoj točki u neposrednoj blizini zastoja strujanja prezentirani su analogno rezultatima kod nominalne radne točke. Usporedbe kontura relativnog Machovog broja za nominalnu radnu točku mogu se vidjeti na Slikama (15), (16) i (17). Kao i u slučaju nominalne radne točke, primjetno je kako se radi o dobrom poklapanju vrijednosti relativnog Machovog broja. Prikazane su slike polja tlaka i temperature - Slika (9), brzine i relativnog Machovog broja - Slika (10) te kinetičke energije turbulencije i turbulentne viskoznosti - Slika (11). Polje temperature prati konture tlaka što je u skladu s jednadžbom stanja idealnog plina.

(a) Eksperiment [1]. **(b)** Numerička simulacija.

Slika 15: Usporedba kontura relativnog Machovog broja između eksperimenta i numeričke simulacije na presjeku visine raspona od 10% za radnu točku u blizini zastoja strujanja.

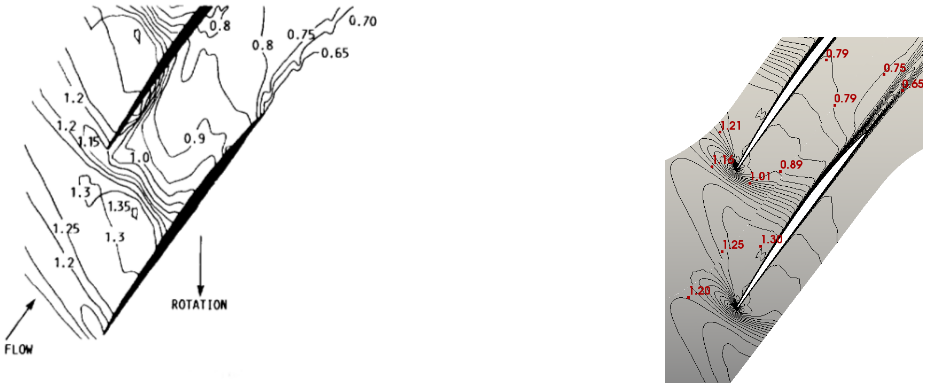

(a) Eksperiment [1]. **(b)** Numerička simulacija.

Slika 16: Usporedba kontura relativnog Machovog broja između eksperimenta i numeričke simulacije na presjeku visine raspona od 30% za radnu točku u blizini zastoja strujanja.

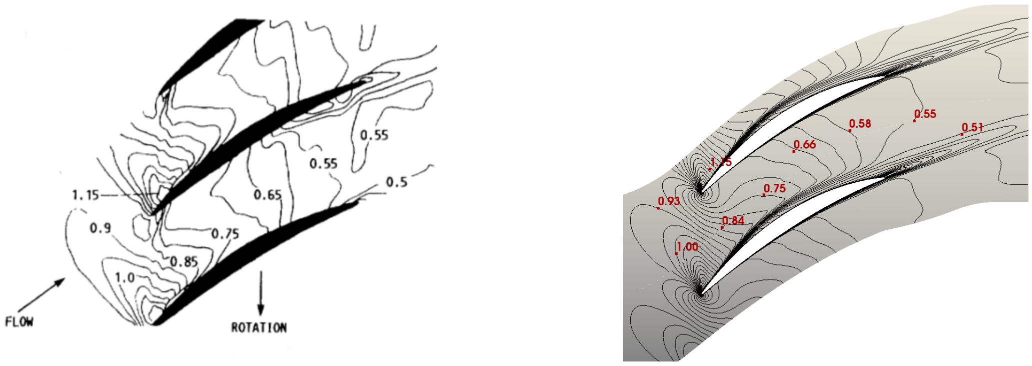

(a) Eksperiment [1]. **(b)** Numerička simulacija.

Slika 17: Usporedba kontura relativnog Machovog broja između eksperimenta i numeričke simulacije na presjeku visine raspona od 70% za radnu točku u blizini zastoja strujanja.

Ponovno je strujanje na ulazu nadzvučno, kroz međulopatični kanal je transoničnog karaktera, dok je na izlazu podzvučno (s obzirom na vrijednosti relativnog Machovog broja). U slučaju opisa strujanja shodno vrijednosti Machovog broja, strujanje je na ulazu podzvučno, kroz međulopatični kanal transonično te na izlazu podzvučno. Temeljem prikaza polja kinetičke energije turbulencije i turbulentne viskoznosti vrtložni trag je jasno vidljiv.

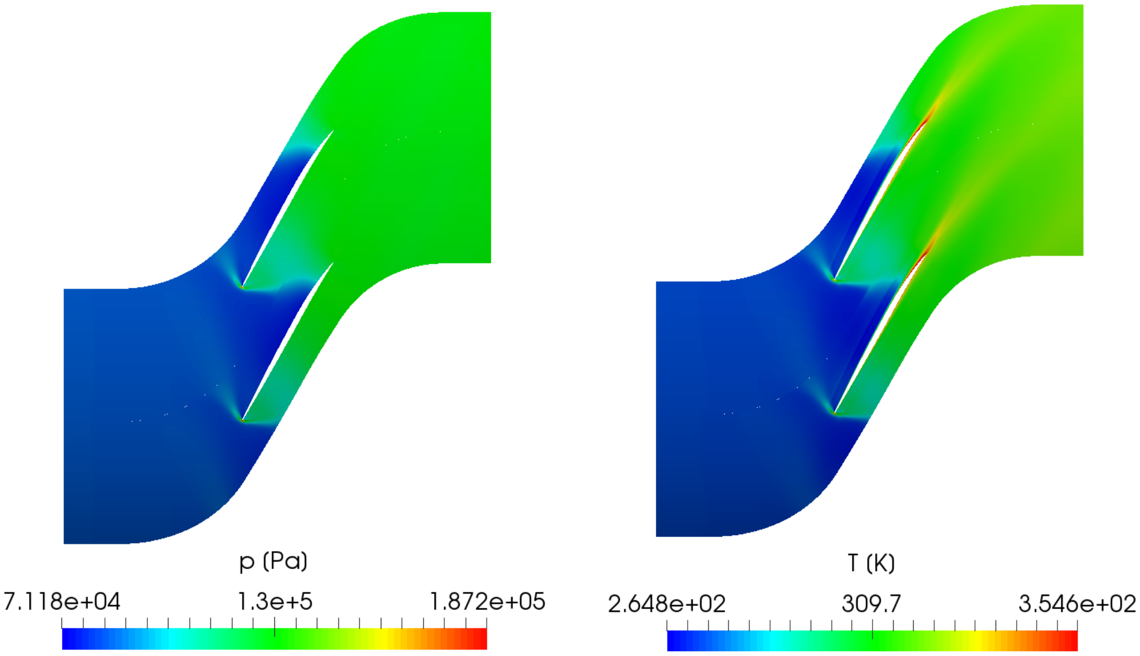

(a) Polje tlaka. **(b)** Polje temperature.

Slika 18: Polje tlaka i temperature na presjeku visine raspona od 10% za radnu točku u blizini zastoja strujanja.

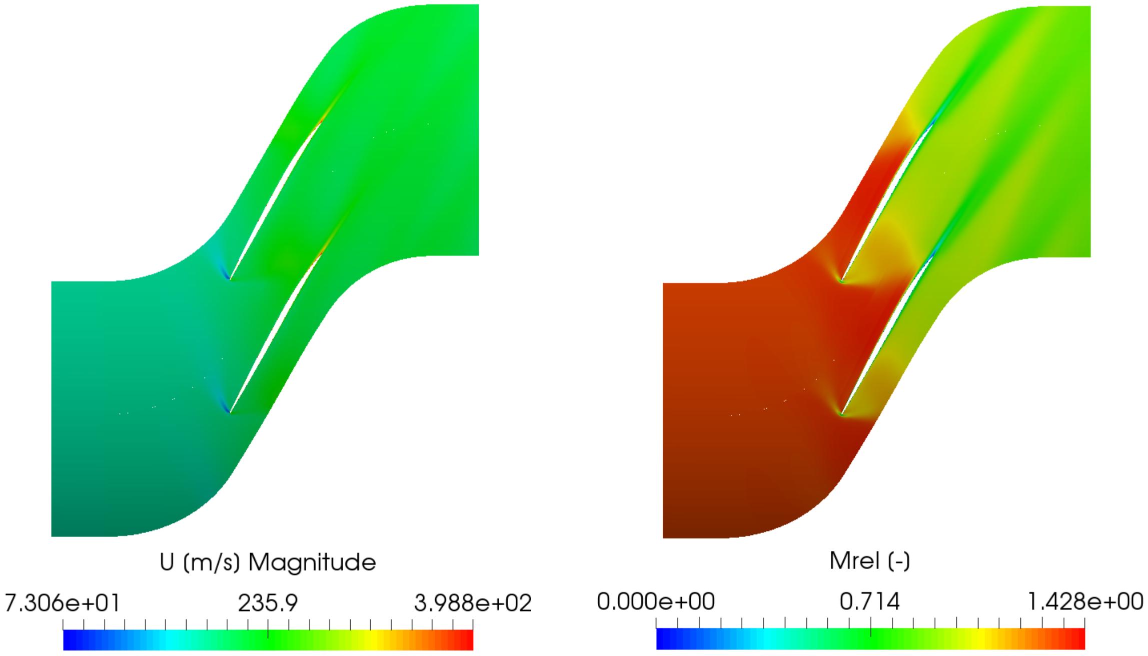

(a) Polje brzine. **(b)** Polje relativnog Machovog broja.

Slika 19: Polje brzine i relativnog Machovog broja na presjeku visine raspona od 10% za radnu točku u blizini zastoja strujanja.

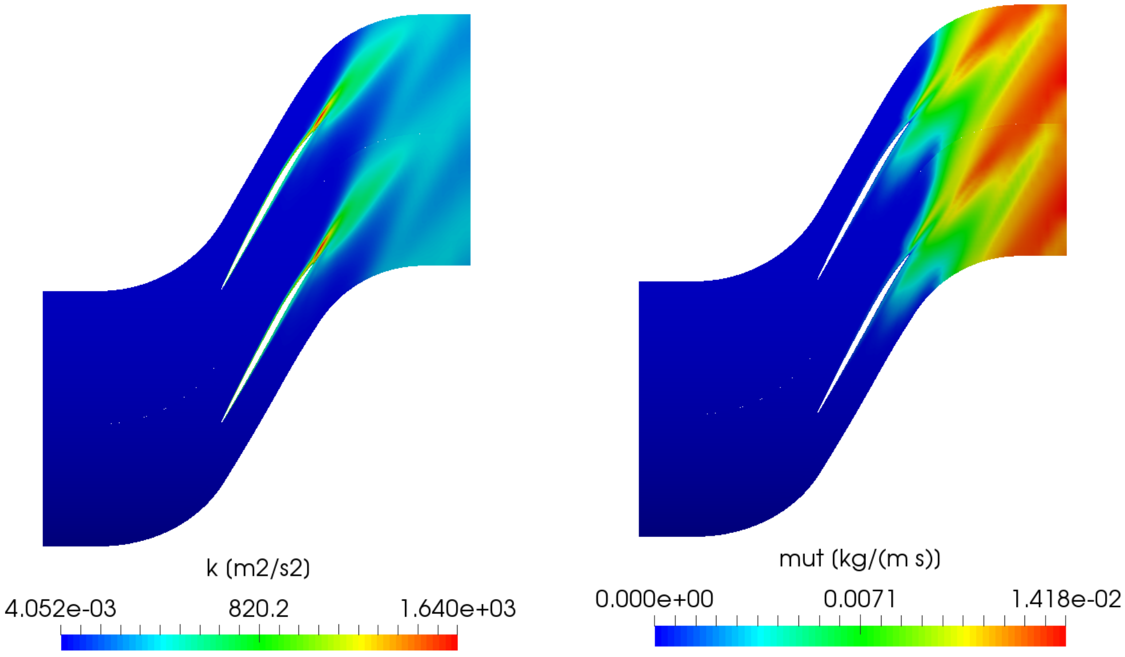

(a) Polje kinetičke energije turbulencije. **(b)** Polje turbulentne viskoznosti.

Slika 20: Polje kinetičke energije turbulencije i turbulentne viskoznosti na presjeku visine raspona od 10% za radnu točku u blizini zastoja strujanja.

Prestrujavanje fluida s pretlačne na potlačnu stranu te vrtlog na vrhu lopatice prikazan je na Slici (21) pomoću strujnica. Geometrija NASA Rotora 67 generira i vrtlog na izlaznom bridu rotorske lopatice koji je prikazan pomoću Q-kontura, te je dan na Slici (22).

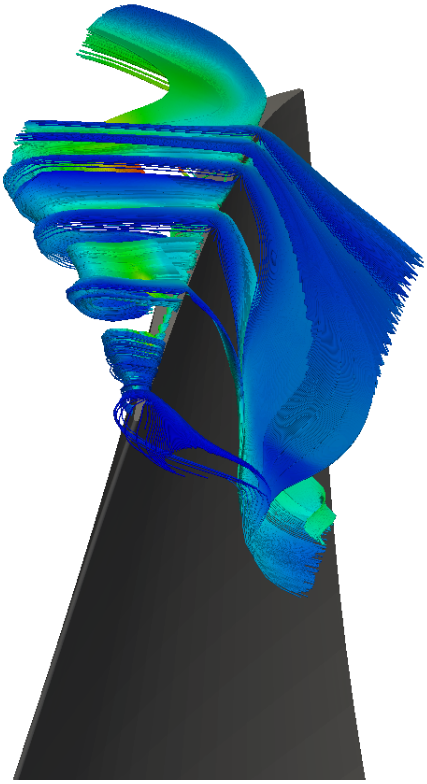

Slika 21: Prikaz prestrujavanja i vrtloga na vrhu lopatice pomoću pomoću strujnica za radnu točku u blizini zastoja strujanja.

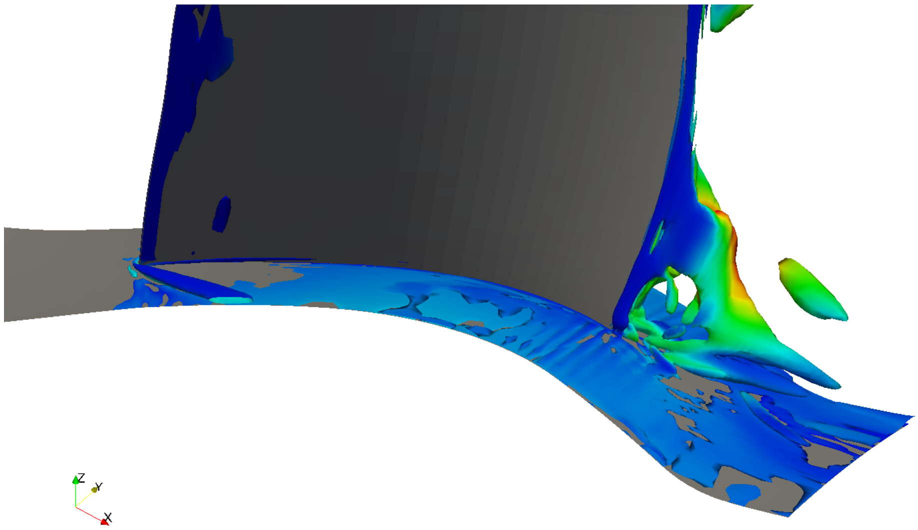

Slika 22: Vizualizacija vrtloga na izlaznom bridu rotorske lopatice pomoću Q-konture za radnu točku u blizini zastoja strujanja.

Vrtlog na izlaznom bridu rotorske lopatice prikazan pomoću strujnica je dan na Slici (14).

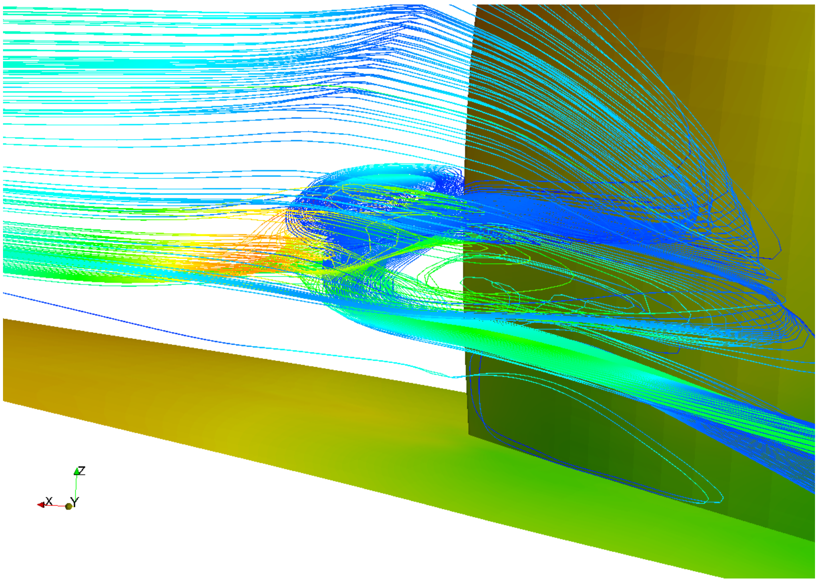

Slika 23: Vizualizacija vrtloga na izlaznom bridu rotorske lopatice pomoću strujnica za radnu točku u blizini zastoja strujanja.

Provedbom numeričke simulacije strujanja u NASA Rotor 67 turboventilatoru za radnu točku u blizini zastoja strujanja su dobivene radne performanse NASA Rotora koje su prikazane u Tablici (4). Usporedbom numeričkih rezultata i eksperimenta zaključuje se da su numerički rezultati u dobrom slaganju s eksperimentom.

Tablica 4: Performanse NASA Rotora 67 u radnoj točki u blizini zastoja strujanja.

Parametar	**Vrijednost**	**Eksperiment**	**Greška**	**Relativna greška, [%]**
Maseni protok, $\dot{m}$	32,23 kg/s	32,305 kg/s	0,075 kg/s	-0,23
Omjer totalnih tlakova, Π	1,6675	1,728	0,0605	3,5
Zakretni moment, T_F	44,7 N m	/	/	/
Aksijalna sila, F	-193,3 N	/	/	/
Snaga, P	75 100 W	/	/	/
Adijabatska iskoristivost, η_ad	88,49%	90,1%	1,61%	1,79

Radna karakteristika

Osim numeričkih simulacija strujanja u nominalnoj radnoj točki i radnoj točki u blizini zastoja strujanja, provedeno je više dodatnih numeričkih simulacija s ciljem generiranja radne karakteristike NASA Rotor 67 turboventilatora za nominalnu brzinu vrtnje. Generirana radna karakteristika prikazana je na Slici (24). Pritom je uz radnu karakteristiku prikazana i krivulja iskoristivosti.

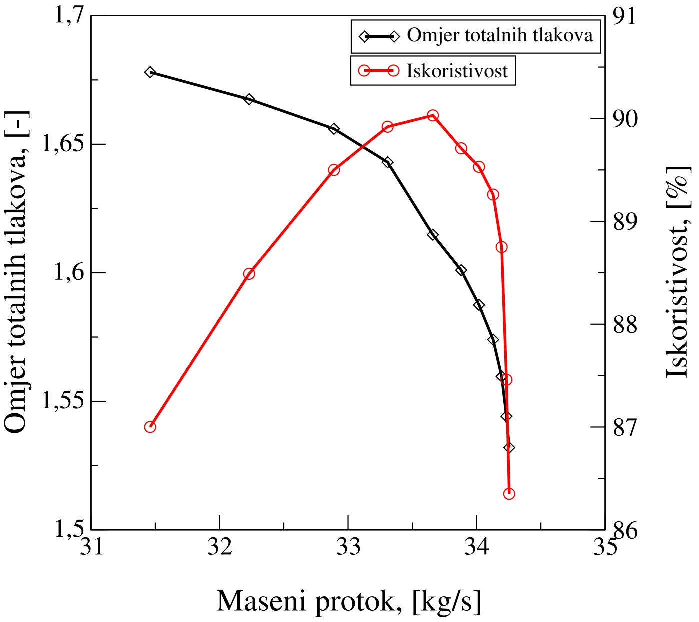

Slika 24: Radna karakteristika NASA Rotora 67.

Kako bi se radna karakteristika generirana numeričkim putem usporedila s radnom karakteristikom dobivenom eksperimentalnim pristupom, radna karakteristika prikazana na Slici (24) je normalizirana s obzirom na maseni protok zagušenja dobiven eksperimentom koji iznosi 34,96 kg/s. Usporedba normaliziranih radnih karakteristika je prikazana na Slici (25).

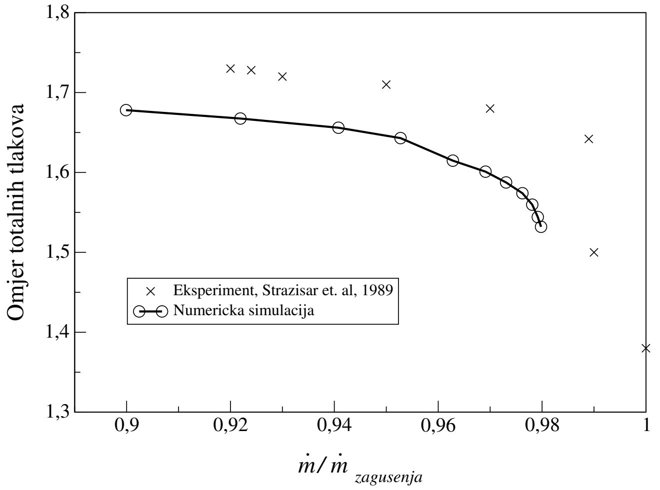

Slika 25: Usporedba generirane radne karakteristike s eksperimentom.

Prema prikazu na Slici (25), dvije normalizirane radne karakteristike se ne poklapaju, no relativno su bliske. Stoga se može zaključiti kako rezultati prezentirani unutar ovog rada daju razumne rezultate zadovoljavajuće točnosti za numeričku simulaciju kompleksnog strujanja kao što je kompresibilno, turbulentno i transonično strujanje u turbostrojevima.

1 Introduction

The complex nature of realistic fluid flow has fascinated mankind since the dawn of civilization. In order to completely describe the behaviour of the fluid flow, an adequate formulation of governing equations was necessary. The appropriate formulation came in the 19th century in terms of a set of partial differential equations that represent the governing equations for fluid particle, the Navier-Stokes equations. Solving the Navier-Stokes equations analytically is possible only for a limited number of very simple cases (Couette and Poisseuille flow), while for more complex cases the assistance of developed numerical methods by means of computer calculations is necessary.

In other words, Navier-Stokes equations represent the heart of the computer-based simulations of the fluid flow.

Computational Fluid Dynamics, as stated in [2], "is the analysis of systems involving fluid flow, heat transfer and associated phenomena such as chemical reactions by means of computer-based simulation". According to the previous statement, various types of simulations which include wide spectra of physical phenomena can be performed. Therefore it is not a big surprise that CFD is used on a daily basis in a wide range of modern high-tech industries such as aerospace, automotive and power generation industry in the design processes for their future components or for the evaluation of characteristics for the existing ones.

Within this thesis, advantages of the CFD are used to deal with another complex engineering topic - compressible flow inside turbomachinery. Currently, research and development of turbomachinery has reached its critical point due to the relatively high level of overall operating performances of current machines. In order to make further performance improvements, specific fluid flow phenomena or sources of "3-dimensional turbomachinery losses" have to be examined. Some of the 3D turbomachinery losses are tip-leakage flow, secondary flow or endwall losses which can not be examined sufficiently accurate by using a traditional experimental approach or elementary 2D analytical flow analysis. Carrying out an experimental research of a certain problem requires a huge amount of money, it is time-consuming and in many cases only a limited amount of information can be obtained. Additionally, in case of some optimisation process, the method of trial and error is very common, which drastically increases total costs.

Thus, to take a closer look into the extremely complex fluid flow patterns inside of turbomachinery passages, the assistance of numerical methods proved to be very useful. Although numerical simulations only represent the approximation of realistic fluid flow, with a certain level of accuracy according to its mathematical model and used numerical methods, their rapid increase in use is recorded and those trends are going to be continued in the future.

1.1 Turbocompressors and Turbofans

Compressors are machines that are used to increase the pressure of the flowing fluid. By doing so, compressors ensure the flow of the fluid by withstanding the friction losses. Thus, they are used in many applications such as compressor stations for gas supply in pipelines, gas turbine power plants, jet engines and so on.
There are two fundamentally different compressor types and their classification is presented below.

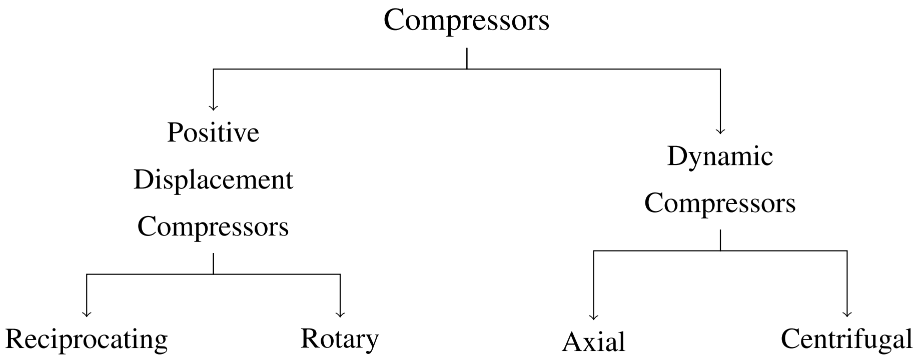

Positive displacement compressors increase the pressure of the flowing fluid by reducing its volume. They can be divided into reciprocating and rotary compressors. Reciprocating compressors compress the fluid in a cylinder via the crankshaft driven piston. On the other hand, rotary compressors, whose representative is a screw compressor, are used instead of reciprocating compressors in application where higher flow rate is necessary.

Dynamic compressors operate in a much different way, and their behaviour is described according to the basic laws of fluid dynamics and thermodynamics. Due to the fact that they are powered by a rotating shaft, they are commonly called turbocompressors.
Turbocompressors are turbomachines that by means of shaft and consequently rotor (and rotor blades) rotation transfer energy (angular momentum) to the compressible flowing fluid. Energy transferred from rotor blades to the flowing fluid as a consequence takes a form of the pressure rise of the fluid.

According to the above classification, turbocompressors can be divided into axial and centrifugal compressors. Operating principle of centrifugal compressors is the same as previously described with addition that flow at the inlet is axial, and in the impeller (rotor) is deflected in a radial direction. As a result of rotor rotation, increase of static pressure and kinetic energy of the fluid is achieved. Static pressure rise of the fluid is achieved on the way through the impeller of the compressor due to the centrifugal force effect. At the outlet of the compressor, fluid is entering a diffuser in which fluid velocity is decreased and therefore kinetic energy is additionally converted into static pressure.

Unlike centrifugal compressor, fluid flow inside of an axial compressor is strictly axial and pressure rise is achieved in a similar way. Due to the shaft rotation, rotor blades attached to the hub also rotate and transfer energy to the flowing fluid. Thus, fluid velocity is increased. Rotor blade passages are designed in a way that they form a diffuser, so that fluid velocity relative to the rotor blades decreases, which consequently causes pressure rise. Unlike centrifugal compressors, axial compressors also have stator blades. They are located behind the rotor blade row and their passages, such as rotor blade passages, also form a diffuser in order to decrease fluid velocity in favour of pressure rise. Likewise, they also serve as guide vanes for the next rotor row. Commonly, axial compressors have many stages, and in many cases there is a row of inlet guide vanes in front of the first rotor row for the flow adjustment.
Axial compressors can be subdivided according to the achieved pressure rise as:

- high-pressure compressors,
- intermediate-pressure compressors ,
- low-pressure compressors or turbofans.

In order to run compressors in optimal and safest way as possible, caution is necessary to avoid serious problems which can occur, so there is a need to understand stability restrictions in their operating range. The stability of an axial-flow compressor can be analysed in two fundamentally different perspectives. The first one is related to matching of compressor and pipeline (downstream flow) characteristics. On the other hand, the second perspective of compressor stability is related to the aerodynamic stability of flow patterns.

Axial-flow compressor operating range is described by its performance map. In Figure (1), a performance map of a transonic compressor for a civil aircraft jet engine is shown. Generally, it is a normalised mass flow rate versus total pressure rise graph, plotted for various constant rotational speeds of the compressor, with defined contours of constant efficiency. With multiple constant speed characteristics defined, a so-called instability line (or surge line) is also defined. According to the performance map, as seen in the Figure (1), stable operating range is limited by both low and high mass flow rates. If a compressor operates at the higher flow rate, flow can be choked and compressor can not be able to ensure the flow any further. On the other hand, if a compressor operates at lower flow rates, aerodynamic instabilities can occur in terms of a rotating stall or surge.

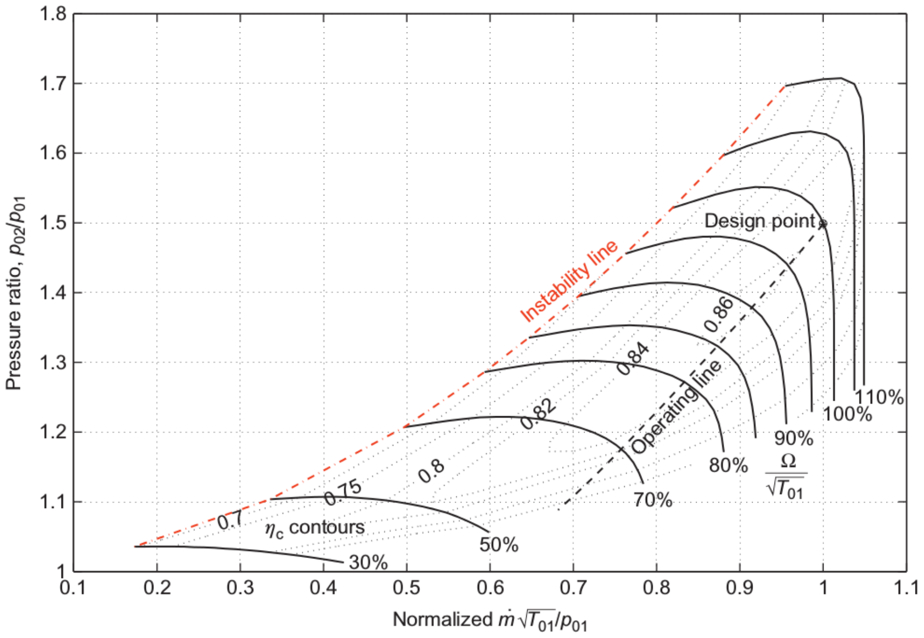

Figure 1: Example of transonic compressor performance map [3].

Rotating stall is a phenomenon of local instability inside of a compressor which can occur at low flow rates. It is characterised by marching flow separation at the suction side of a rotor blade, which "travels" around the annulus as the blade moves away from the disturbance. When a blade row is stalled, the blades stall in separate stall sections instead of all blades stalling together as might be expected. Those stalled sections of an annulus are called stall-cells. One of the features of a rotating stall is a steady average mass flow rate in the annulus, which is circumferentially non-uniform. A rotating stall can damage the rotor blades which suffer from additional fatigue and pressure oscillations during stall cycle [3, 4].
There are two types of rotating stall:

- **part-span stall**: only a certain part of blade passage is stalled, usually a blade tip,
- **full-span stall**: entire height of an annulus is stalled with multiple stall cells.

Likewise, surge is a serious global instability phenomenon followed by vibrations. While a flow rate during a rotating stall in a compressor appears to be steady, a flow rate during surge will pulse, characterised by axial oscillation of the flow which can even result in the reversed flow. As both instability phenomena appear very close on the performance map for low mass flow rates, it is still not certain which instability will appear in a specific compressor at the surge line. Commonly, the size of the whole compressor system determines which one will occur. In a compressor with a short exit pipeline and small volume inside of a system, rotating stall is dominant. On the other hand, a compressor attached to some storage tank will surge [3, 4]. As stated in [3], the point at which a compressor enters stall or surge still cannot be predicted reliably, even with the most advanced computational methods.

In other words, it is critical for the high speed turbocompressor to operate in stable operating range in order to avoid instabilities, vibrations and damage on the compressor system.

1.2 Scope of the Thesis

Compressible flow in turbomachinery is often examined with the assistance of CFD instead of performing expensive experiments. In order to increase the CFD capabilities by developing codes capable of solving specific phenomena, newly implemented code formulations also have to be tested and validated on characteristic test cases.

Within this thesis, the aim is to perform a numerical simulation of a steady, compressible, turbulent and transonic flow inside of an axial-flow NASA Rotor 67 turbofan, by using a newly implemented CFD code. Generally speaking, flows between the supersonic and subsonic regime (transonic flows) are the most difficult to solve due to the mix of elliptic and hyperbolic nature of the partial differential equations [5]. New formulation of a compressible flow solver has a modified energy equation and it is based on a conservation of rothalpy, instead of total enthalpy. Rothalpy, or relative total enthalpy, is a thermodynamic quantity of the compressible fluid that is conserved over a blade row but not over a stage [3, 6].

In order to perform numerical simulations, first a 3D CAD model needs to be generated in appropriate CAD software package according to the corresponding literature. Adequate mesh of finite volumes needs to be afterwards generated in Pointwise meshing software package.

Recently, a new pressure-based `steadyCompressibleMRFFoamRothalpy` solver was implemented in `foam-extend`, a community driven fork of the open-source CFD package OpenFOAM [7]. `Foam-extend` is equipped with tools specially developed for handling turbomachinery flow analyses. These tools are Multiple Reference Frame (MRF) [8] and General Grid Interface (GGI) [9].

MRF represents a steady-state technique for simulating turbomachinery. Rotating flow is achieved by adding additional terms in the mathematical model to the rotating zone cells: centrifugal and Coriolis force terms. In this way, a steady-state simulation is carried out on a stationary rotor without moving the mesh. This modelling technique is commonly called the "frozen rotor" approach.

General Grid Interface is a feature for handling communication and interpolation between non-conformal meshes. Non-conformal meshes imply the mismatch of grid nodes on the connection of the two sides of a domain. Since only one portion of the annulus is simulated in order to reduce computational cost, a `cyclicGGI` interface is used. This is a variant of a GGI interface that involves a coordinate transformation on a periodic boundary.

Numerical simulations are carried out for a near peak efficiency and near stall operating point. With the obtained data, a performance curve for the NASA Rotor 67 at the nominal angular velocity is evaluated. Results are presented in terms of mass flow, total pressure ratio, power and efficiency, and are followed by a graphical representation of a flow field quantities at various sections of the domain. Finally, obtained results are compared to the reference experimental data [1].

1.3 Thesis Outline

The aim of the thesis is to perform multiple numerical simulations for the NASA Rotor 67 Turbofan in order to assemble a single fan performance curve for a nominal angular velocity and to compare the obtained results with reference experimental data. For that purpose, NASA Rotor 67 Turbofan's performance is evaluated in the near peak efficiency and near stall operating point.

The work covered within this thesis is divided into the following chapters: Section (2) describes the used mathematical model for solving compressible, turbulent and transonic fluid flow in a turbofan. In Section (3) general information related to the NASA Rotor 67 Turbofan is presented along with the proposed numerical methods. Section (4) covers preprocessing steps, including a 3D CAD model generation, which is a basis for the numerical domain generation afterwards. Generation of the numerical domain represents the spatial discretization and is the first step for performing CFD simulations. Section (5) covers obtained results with adequate graphical representation of the flow field quantities on various cross sections of the numerical domain. Section (6) is reserved for the author's conclusion related to the thesis, with further recommendations for the future work on the treated topic.

2 Mathematical Model

In this section, mathematical model for solving steady, compressible, turbulent and transonic flow in rotating turbomachinery is presented. Mathematical model presented in this section is implemented in `foam-extend` [7] and is used within this thesis for transonic turbofan calculation.

2.1 Introduction

This section deals with the mathematical model and governing equations that are used for steady-state simulation of a transonic turbofan. In order to completely describe the mathematical model, a generic scalar transport equation is firstly presented and its terms are properly explained. In subsequent subsections, governing equations for fluid flow are presented in terms of conservation of mass, linear momentum and energy, along with the additional form of energy equation for rotating turbomachinery - energy conservation equation in terms of rothalpy. Turbulence is modelled using a compressible formulation of the $k-\omega$ SST turbulence model, therefore the corresponding transport equations are also presented. Within this thesis, Multiple Reference Frame (MRF) mathematical model is used. MRF is also known as a "frozen rotor" approach due to the fact that the "rotating zone" is steady, there is no moving mesh and the effect of rotation is achieved by adding convective transport terms in the governing equations: centrifugal and Coriolis force for the cells in a rotating cell zone. Since the MRF model is used, adjusted formulations of conservation equations are also presented due to the calculation in the relative frame of reference. Finally, the last subsection covers the use of General Grid Interface to couple the non-conformal mesh boundaries.

2.2 Governing Equations of the Fluid Flow

Generic scalar transport equation models a combination of convection and diffusion transport of an arbitrary scalar property ϕ. Generic scalar transport equation in its standard and generalised form can be expressed as follows [5]:

$$\frac{\partial \phi}{\partial t} + \nabla \bullet (\phi \mathbf{u}) - \nabla \bullet (\gamma \nabla \phi) = q_v, \tag{1}$$

where ϕ is a transported arbitrary scalar property, $\mathbf{u}$ is a convective velocity, γ is a diffusion coefficient and q_v is an arbitrary local volume source or sink of scalar ϕ.

In the Equation (1), terms from left to right represent as follows:

- temporal term, describing the inertia of the isolated system,
- convection term, which represents the convective transport of the scalar field ϕ by the velocity $\mathbf{u}$,
- diffusion term, which represents the transport due to the existence of a spatial gradient of the transported scalar property ϕ and the diffusion coefficient γ,
- source and sink term, describing the local volume production or destruction of an arbitrary scalar property ϕ and accounts for a non-transport phenomenon.

Diffusion term has an elliptic nature of the Partial Differential Equation (PDE), which means that every cell in the domain feels the influence of every other cell instantaneously. On the other hand, convection term has a hyperbolic nature of the PDE meaning that cell information is defined by the direction of the convective velocity [5].

Generic scalar transport equation represents the general transport equation for the fluid flow, from which all other governing equations can be derived by simple substitution of the transported property ϕ with a new transported property.

2.2.1 Conservation of Mass

Governing equation for the conservation of mass, or the continuity equation can be derived from the Equation (1) and its form for the compressible fluid flow is represented as follows:

$$\frac{\partial \rho}{\partial t} + \nabla \bullet (\rho \mathbf{u}) = 0. \tag{2}$$

Continuity equation is derived directly from the generic transport equation, Equation (1), by simple substitution of the transported scalar property ϕ with the fluid density ρ which is a transported property. As mass is not transported by diffusion, there is no diffusion term present in the above equation. Furthermore, if it is assumed that mass is not transferred into energy or vice-versa, the source and sink terms are absent likewise.

2.2.2 Conservation of Linear Momentum

If a generic transported scalar property ϕ in Equation (1) is substituted with the momentum property $\rho\mathbf{u}$, after slight modifications it can be written:

$$\frac{\partial(\rho\mathbf{u})}{\partial t} + \nabla\bullet(\rho\mathbf{u}\otimes\mathbf{u}) = \rho\mathbf{g} + \nabla\bullet\boldsymbol{\sigma}, \tag{3}$$

where $\rho\mathbf{u}$ is the momentum per unit volume, $\rho\mathbf{g}$ is a body force and $\boldsymbol{\sigma}$ is the Cauchy stress tensor. Cauchy stress tensor $\boldsymbol{\sigma}$ represents all stresses that act on a fluid particle including the shear-rate stress tensor and pressure forces.

Since the momentum equation is a vector equation, it is possible to decompose it into three scalar differential equations, each for the respective spatial component of the momentum quantity, which are commonly called Navier-Stokes equations. In the above equation, according to Newton's second law of motion, source and sink terms on the right-hand side are equal to the sum of mass forces ($\rho\mathbf{g}$) and ($\nabla\bullet\boldsymbol{\sigma}$).

The stress tensor $\boldsymbol{\sigma}$ consists of a thermodynamic pressure p and a viscous stress tensor $\boldsymbol{\tau}$ as follows,

$$\boldsymbol{\sigma} = -p\mathbf{I} + \boldsymbol{\tau}, \tag{4}$$

where $\mathbf{I}$ is the identity or unit tensor.
Viscous stress tensor $\boldsymbol{\tau}$ for a Newtonian fluid can be written in a general way:

$$\boldsymbol{\tau} = 2\mu\mathbf{D} - \frac{2}{3}\mu\,(\nabla\bullet\mathbf{u})\,\mathbf{I}, \tag{5}$$

where μ is the dynamic viscosity, and $\mathbf{D}$ is a symmetric part of a velocity gradient tensor (shear-rate tensor), which represents the deformation rate. Shear-rate tensor $\mathbf{D}$ is formulated as follows,

$$\mathbf{D} = \frac{1}{2}\left[\nabla\mathbf{u} + (\nabla\mathbf{u})^T\right]. \tag{6}$$

Substituting the Equation (6) into the Equation (5), a complete formulation of a viscous stress tensor $\boldsymbol{\tau}$ can be written as follows,

$$\boldsymbol{\tau} = \mu\left[\nabla\mathbf{u} + (\nabla\mathbf{u})^T\right] - \frac{2}{3}\mu\,(\nabla\bullet\mathbf{u})\,\mathbf{I}. \tag{7}$$

Constitutive relation for a Cauchy stress tensor $\boldsymbol{\sigma}$ is now completely defined:

$$\boldsymbol{\sigma} = -\left(p + \frac{2}{3}\mu \nabla \bullet \mathbf{u}\right)\mathbf{I} + \mu\left[\nabla \mathbf{u} + (\nabla \mathbf{u})^T\right]. \tag{8}$$

The Equation (3) can now be rewritten in its full form as follows [10]:

$$\frac{\partial(\rho \mathbf{u})}{\partial t} + \nabla \bullet (\rho \mathbf{u} \otimes \mathbf{u}) = \rho \mathbf{g} - \nabla\left(p + \frac{2}{3}\mu \nabla \bullet \mathbf{u}\right) + \nabla \bullet \left[\mu\left(\nabla \mathbf{u} + (\nabla \mathbf{u})^T\right)\right]. \tag{9}$$

Since the velocity $\mathbf{u}$ in the convective term is both the convective and convected property, it is the source of the non-linearity due to the fact that the solution for the velocity field depends on itself.

2.2.3 Conservation of Energy

If a generic transported scalar property ϕ in the Equation (1) is substituted with the product of density and specific total energy ρe, after slight modifications a form of the total energy conservation equation can be written as:

$$\frac{\partial(\rho e)}{\partial t} + \nabla \bullet (\rho e \mathbf{u}) = \rho \mathbf{g} \cdot \mathbf{u} + \nabla \bullet (\boldsymbol{\sigma} \cdot \mathbf{u}) - \nabla \bullet \mathbf{q} + \rho Q, \tag{10}$$

where e is a specific total energy, $\mathbf{q}$ is a heat flux vector and Q is a volume energy source.

In order to close the system of differential equations, a number of additional, constitutive relations is needed as well as the stress tensor $\boldsymbol{\sigma}$ defined in the Equation (8). The heat flux vector $\mathbf{q}$ can be expressed using the constitutive relation of the Fourier's law of heat conduction as follows,

$$\mathbf{q} = -\lambda \nabla T, \tag{11}$$

where λ is a thermal conductivity, which is a fluid property dependent on the thermodynamic state of the fluid particle. In general, it can be written,

$$\lambda = \lambda(p, T). \tag{12}$$

Molecular viscosity μ can be generally expressed in a similar way,

$$\mu = \mu(p, T). \tag{13}$$

Finally, there is a need to couple density ρ with the rest of the system. Generally, density is dependent on the thermodynamic state of the fluid particle as stated in the Equation (14).

$$\rho = \rho(p, T). \tag{14}$$

For that purpose, constitutive relation of the equation of state of the perfect gas is typically used to establish a relationship between density and pressure field:

$$\rho = \frac{p}{RT} = \psi p, \tag{15}$$

where R is an individual gas constant and ψ is compressibility:

$$\psi = \frac{1}{RT}. \tag{16}$$

If the above-mentioned constitutive relations for the heat flux density vector $\mathbf{q}$ and the stress tensor $\boldsymbol{\sigma}$ are applied, with slight modifications the Equation (10) can be rewritten in its full form:

$$\begin{aligned} \frac{\partial(\rho e)}{\partial t} + \nabla \bullet (\rho e \mathbf{u}) = \rho \mathbf{g} \cdot \mathbf{u} - \nabla \bullet (p\mathbf{u}) - \nabla \bullet \left(\frac{2}{3}\mu\left(\nabla \bullet \mathbf{u}\right)\mathbf{u}\right) \\ + \nabla \bullet \left[\mu\left(\nabla \mathbf{u} + (\nabla \mathbf{u})^T\right) \cdot \mathbf{u}\right] + \nabla \bullet (\lambda \nabla T) + \rho Q. \end{aligned} \tag{17}$$

Energy conservation in the Equation (17) is presented in terms of specific total energy and it consists of the internal (thermal) energy u and the mechanical (kinetic) energy e_{M}.

$$e = u + e_{\mathrm{M}}, \tag{18}$$

where internal energy u is a function of pressure and temperature,

$$u = u(p, T), \tag{19}$$

and the kinetic energy is described as follows:

$$e_{\mathrm{M}} = \frac{1}{2}(\mathbf{u} \cdot \mathbf{u}). \tag{20}$$

In the compressible flow calculations, it is more common to use an alternative form of energy conservation equation in terms of specific enthalpy equation or specific total enthalpy. Specific enthalpy h is the sum of internal energy and the kinematic pressure as follows,

$$h = u + \frac{p}{\rho}. \tag{21}$$

On the other hand, the specific total enthalpy h_0 is calculated by summing the specific enthalpy and the mechanical (kinetic) energy of the fluid particle in the following way,

$$h_0 = h + \frac{1}{2}(\mathbf{u} \cdot \mathbf{u}) = u + \frac{p}{\rho} + \frac{1}{2}(\mathbf{u} \cdot \mathbf{u}) = e + \frac{p}{\rho}. \tag{22}$$

If the specific total energy e in the Equation (10) is substituted with the expression for e from the Equation (22), the energy conservation equation in terms of the specific total enthalpy can be written in the following form,

$$\frac{\partial(\rho h_0)}{\partial t} - \frac{\partial p}{\partial t} + \nabla \bullet (\rho \mathbf{u} h_0) = \rho \mathbf{g} \cdot \mathbf{u} + \nabla \bullet (\sigma \cdot \mathbf{u}) - \nabla \bullet \mathbf{q} + \rho Q. \tag{23}$$

For most compressible flow analyses, the energy conservation equation in terms of specific total enthalpy, Equation (23), is regularly used and is sufficient for accurate flow calculations. Although the energy conservation equation presented in Equation (23) is valid, within this thesis another approach is preferred. Since the new `foam-extend` code uses a different formulation, energy conservation equation in terms of relative total enthalpy or commonly called rothalpy is to be presented.

2.2.4 Conservation of Rothalpy

The alternative formulation of energy conservation equation, implemented in the new `foam-extend` code specially for flows in turbomachinery, is presented in terms of rothalpy. Rothalpy is a thermodynamic quantity of a compressible fluid that is constant over a streamline. It is conserved over a rotor blade row or stator blade row, but not over a stage [3, 6]. Due to the turbomachinery analysis in moving frames of reference, the energy equation uses rothalpy as a conservative quantity, where rothalpy i is defined as [11],

$$i = h - \omega r u_\Theta, \tag{24}$$

where h is static enthalpy, r is radius, ω is the angular velocity and u_Θ is the tangential component of the absolute velocity. Formulation of rothalpy conservation equation strictly depends on the used MRF method formulation. Since the MRF can be formulated via either relative or absolute velocity, therefore two rothalpy conservation formulations exist. For the MRF method described in terms of the absolute velocity, rothalpy conservation equation is presented as follows [11]:

$$\nabla \bullet (\rho i \mathbf{u}_{\mathrm{rel}}) = -\nabla \bullet (\rho \omega r u_\Theta \mathbf{u}_{\mathrm{rel}}) - \nabla \bullet (p\mathbf{u}) + \nabla \bullet (\boldsymbol{\tau} \cdot \mathbf{u}) + \nabla \bullet (\lambda \nabla T) + S_{\mathrm{H}}, \tag{25}$$

where $\mathbf{u}_{\mathrm{rel}}$ is a relative velocity vector and S_{H} is a source term of enthalpy. On the other hand, if the relative velocity formulation of the MRF method is used, rothalpy conservation equation yields another formulation accordingly [11]:

$$\nabla \bullet (\rho i \mathbf{u}_{\mathrm{rel}}) = \nabla \bullet (\boldsymbol{\tau} \cdot \mathbf{u}) + \nabla \bullet (\lambda \nabla T) + S_{\mathrm{H}}. \tag{26}$$

Since rothalpy is conserved over a certain blade row (but not over a stage), a special care needs to be taken in cases of rotor-stator interaction in order to accurately resolve a fluid flow. Therefore, if the rothalpy equation is solved, rothalpy is continuous over the domain, but the quantities that are calculated from rothalpy (enthalpy h and temperature T) have a jump over the rotor-stator interface due to the change in angular velocity ω. Thus, a rothalpy jump Δi on the interface is used in order to manipulate rothalpy in a way that ensures continuous evaluation of enthalpy h and temperature T field. Rothalpy jump is defined with the following expression:

$$\Delta i \; = \; -\omega r \mathbf{u}_{\mathrm{rel}}. \tag{27}$$

2.3 Turbulence Modelling

Turbulence is irregular, disordered, non-stationary, three-dimensional, highly non-linear and irreversible stochastic phenomenon [5] which commonly occurs in most realistic fluid flows. A turbulent flow regime is characterised by a chaotic behaviour, increased diffusivity and energy dissipation, which is present in a wide span of spatial and temporal scales. The nature of turbulent vortices is commonly presented in terms of vortex stretching energy cascade, as shown in Figure (2).

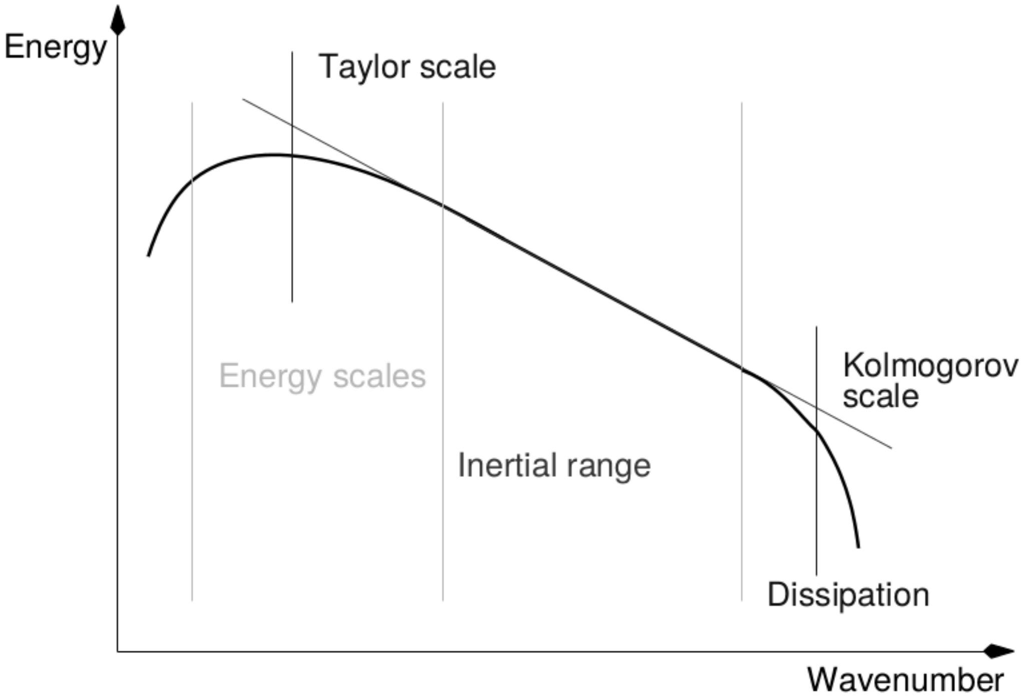

Figure 2: Energy cascade [5].

In the Figure (2), the concept of turbulent flow is shown in terms of energy vs. wavenumber relations for turbulent eddies, where wavenumber represents how many vortices fit into the space. The largest vortices (Taylor length-scale) contain the highest amount of turbulent kinetic energy, while the smallest turbulent eddies contain a small amount of energy. The largest vortices are created within a flow influenced by a domain shape, and as a result of vortex stretching they decay into smaller ones, which further fall apart into smaller ones, up to the smallest-scale vortices. The length-scale of smallest vortices is called a Kolmogorov scale. In the process of vortex decomposition, a turbulent kinetic energy is transferred from large-scale to small-scale vortices. Final vortices contain the smallest amount of turbulent kinetic energy which finally dissipates into heat due to viscous effects.

According to the introduced turbulent length-scales, there are three different CFD simulation approaches for solving turbulent flow, based on the needed level of resolved details:

- Direct Numerical Simulation (DNS),
- Large Eddy Simulation (LES),
- Reynolds Averaged Navier-Stokes Equations (RANS).

DNS is used to resolve the complete fluid flow on all scales and hence a turbulence is not modelled at all. The unsteady Navier-Stokes equations are solved on high resolution grids to capture both mean flow and turbulent velocity fluctuations. Due to the high computational cost, it is rarely used for industrial flow computations [2, 5].

LES is focused on simulating the coherent structures and large-scale turbulence of energy spectrum. LES involves space filtered unsteady Navier-Stokes equations prior the computations, which passes the larger eddies and rejects the smaller ones. Due to unsteady flow calculations, demands on computing resources are large [2]. However, smaller energy-dissipating vortex scales are modelled, thus reducing the need for spatial resolution. Based on the idea that smallest scales of turbulent flows are approaching homogeneous and isotropic turbulence, which is easier to model, LES today is a practical engineering tool for complex turbulent flows.

RANS solves the averaged Navier-Stokes equations in order to obtain results of the mean flow field quantities which are commonly sufficient for most engineering analyses. Due to that, a grid resolution is not governed by a Kolmogorov length-scale and hence computational requirements are drastically decreased. The idea behind the RANS approach is to decompose flow field quantities into their *mean* and *fluctuating* components, and ignore the influence of instantaneous terms which are not of interest. In such way, one additional term appears in the Reynolds-Averaged momentum equation. It is the Reynolds stress tensor $\mathbf{R}$, the only term that takes into account instantaneous velocity fluctuations within the presented approach [2, 5]. Since RANS approach is used within this thesis, it will be described in further detail.

Within the RANS approach, a commonly used averaging method is a Reynolds-Averaging. But for flows with significant compressibility effects, a more complicated Favre-Averaging procedure is used due to density fluctuations. In such way, a density-weighting averaging is used [12]. If Φ is taken as a general instantaneous variable, a Favre-Averaging procedure is expressed as follows:

$$\Phi = \widetilde{\Phi} + \Phi'', \tag{28}$$

where Φ is general instantaneous variable, which is decomposed into a mean (Favre-Averaged) $\widetilde{\Phi}$ and fluctuating component Φ''.
Favre-Averaged density-weighted variable $\widetilde{\Phi}$ is defined as follows,

$$\widetilde{\Phi} = \frac{\overline{\rho \Phi}}{\overline{\rho}}, \tag{29}$$

where overbars denote standard Reynolds-Averaging.
Having defined the expressions for Favre-Averaging, Reynolds-Averaged Navier-Stokes equations and the continuity equation can be defined as follows,

- **continuity equation**

  $$\frac{\partial \overline{\rho}}{\partial t} + \nabla \bullet (\overline{\rho} \widetilde{\mathbf{u}}) = 0, \tag{30}$$

  where $\overline{\rho}$ represents Reynolds-Averaged density and $\widetilde{\mathbf{u}}$ is the Favre-Averaged (density-weighted averaged) velocity.

- **Reynolds-Averaged momentum equation**

  $$\frac{\partial \overline{\rho} \widetilde{\mathbf{u}}}{\partial t} + \nabla \bullet (\overline{\rho} \widetilde{\mathbf{u}} \otimes \widetilde{\mathbf{u}}) = \nabla \bullet \overline{\sigma} + \overline{\rho} \mathbf{g} + \nabla \bullet \mathbf{R}, \tag{31}$$

  where $\overline{\sigma}$ is the Reynolds-Averaged Cauchy stress tensor and $\mathbf{R}$ is the Reynolds stress tensor. Reynolds stress tensor $\mathbf{R}$ is a symmetric second order tensor that is represented with the following expression,

  $$\mathbf{R} = -\overline{\rho \mathbf{u}'' \otimes \mathbf{u}''}. \tag{32}$$

By using the Reynolds-Averaging procedure six additional unknowns were introduced due to interactions between various turbulent fluctuations, and no further equations were introduced. Thus, this is the source of the known *closure problem* for turbulent flows. In order to close the system and to model the Reynolds-stress tensor, a turbulence model has to be introduced. There are few theories available, but the most famous and widely used is the Boussinesq's eddy viscosity hypothesis.

Boussinesq proposed proportionality between Reynolds stresses and a mean deformation rate [2], so the Reynolds stress tensor can be modelled in the following way:

$$\mathbf{R} = \mu_\mathrm{t}\left[\nabla\widetilde{\mathbf{u}} + (\nabla\widetilde{\mathbf{u}})^T\right] - \frac{2}{3}\mu_\mathrm{t}\nabla\bullet(\widetilde{\mathbf{u}})\,\mathbf{I} - \frac{2}{3}\overline{\rho}\mathbf{I}k, \tag{33}$$

where μ_t is a turbulent (eddy) viscosity and k is the turbulent kinetic energy. Turbulent kinetic energy k is defined as follows,

$$k = \frac{1}{2}\overline{\mathbf{u}'' \cdot \mathbf{u}''}. \tag{34}$$

If one looks at the Equation (33), it is very similar to the Equation (7), with the existence of one additional term (the last term on the right-hand side). This term is necessary to ensure the proper trace of the Reynolds-stress tensor **R** [13].

There are many turbulence models present today, and they can be divided into the following main categories [13]:

- Algebraic (zero-equation) turbulence models,
- One-equation turbulence models,
- Two-equation turbulence models.

Within this thesis, a two-equation turbulence model based on the Boussinesq's hypothesis of eddy viscosity is used, which is to be presented in the following subsection. The turbulence model used in this study is $k-\omega$ SST turbulence model.

2.3.1 Compressible $k-\omega$ SST Turbulence Model

Within this thesis a two-equation eddy viscosity $k-\omega$ Shear Stress Transport (SST) turbulence model is used [14]. Since the turbulent model is implemented in `foam-extend`, a community driven fork of the CFD package OpenFOAM, its full implementation is presented by Keser [15].

$k-\omega$ SST turbulence model is taking advantage of the two most commonly used turbulence models: $k-\varepsilon$ and $k-\omega$ turbulence model. The general idea behind the whole "equation mix" is to use the $k-\omega$ turbulence model near the wall and to switch to the $k-\varepsilon$ in the free-stream. In order to properly resolve turbulent behaviour of the flow within the RANS approach, the $k-\omega$ SST turbulence model uses two general transport equations, the one for the turbulent kinetic energy k and the other one for the eddy turn-over time ω.
A transport equation for the turbulence kinetic energy k is stated in the following way:

$$\frac{\partial \overline{\rho} k}{\partial t} + \nabla \bullet \left(\overline{\rho} \widetilde{\mathbf{u}} k \right) - k \nabla \bullet \left(\overline{\rho} \widetilde{\mathbf{u}} \right) = \min \left(G,\ c_1 \beta^* k \omega \right) - \beta^* \rho \omega k, \tag{35}$$

while the transport equation for the eddy turn-over time ω reads,

$$\begin{split} \frac{\partial \overline{\rho} \omega}{\partial t} + \nabla \bullet \left(\overline{\rho} \widetilde{\mathbf{u}} \omega \right) - \omega \nabla \bullet \left(\overline{\rho} \widetilde{\mathbf{u}} \right) - \nabla \bullet \left(\Gamma_{\mathrm{k,eff}} \nabla \omega \right) = \\ \gamma \min \left[S_2, \frac{c_1}{a_1} \beta^* \omega \max \left(a_1 \omega,\ b_1 F_{23} \sqrt{S_2} \right) \right] - \beta \overline{\rho} \omega^2 + (1 - F_1) CD_{\mathrm{k},\omega}. \end{split} \tag{36}$$

First, effective diffusion coefficients for turbulence kinetic energy $\Gamma_{\mathrm{k,eff}}$ and eddy turn-over time $\Gamma_{\omega,\mathrm{eff}}$ equation are defined in the following way,

$$\Gamma_{\mathrm{k,eff}} = \alpha_{\mathrm{k}} \mu_{\mathrm{t}} + \mu, \tag{37}$$

$$\Gamma_{\omega,\mathrm{eff}} = \alpha_{\omega} \mu_{\mathrm{t}} + \mu, \tag{38}$$

where μ is a molecular dynamic viscosity. Eddy viscosity μ_{t} is evaluated using:

$$\mu_{\mathrm{t}} = \frac{\overline{\rho} a_1 k}{\max \left[a_1 \omega,\ b_1 F_{23} \sqrt{2} \left| \frac{1}{2} \left(\nabla \widetilde{\mathbf{u}} + \left(\nabla \widetilde{\mathbf{u}} \right)^T \right) \right| \right]}. \tag{39}$$

Production of the turbulence kinetic energy G is calculated in the following way,

$$G = \mu_\mathrm{t} S_2, \tag{40}$$

where S_2 represents

$$S_2 = 2\left|\frac{1}{2}\left(\nabla\widetilde{\mathbf{u}} + (\nabla\widetilde{\mathbf{u}})^T\right)\right|^2. \tag{41}$$

Blending functions are used in order to achieve smooth switch from $k-\omega$ turbulence model in the inner parts of a boundary layer near the wall, to the $k-\varepsilon$ turbulence model.

F_1 is a blending function that is equal to one in the viscous sublayer and in the logarithmic region of the boundary layer, and gradually switches to zero in the wake region [14].

$$F_1 = \tanh\left[(arg_1)^4\right], \tag{42}$$

where arg_1 is defined as follows,

$$arg_1 = \min\left\{\min\left[\max\left(\frac{\sqrt{k}}{\beta^*\omega y}, \frac{500\nu}{y^2\omega}\right), \frac{4\alpha_{\omega,2}k}{CD_{\mathrm{k},\omega+y^2}}\right], 10\right\}. \tag{43}$$

Blending function F_2 is equal to one for boundary-layer flows, and is equal to zero for free shear layers [14] and can be expressed the following way,

$$F_2 = \tanh\left[(arg_2)^2\right], \tag{44}$$

where arg_2 is defined as follows,

$$arg_2 = \min\left[\max\left(\frac{2\sqrt{k}}{\beta^*\omega y}, \frac{500\nu}{y^2\omega}\right), 100\right]. \tag{45}$$

Blending functions F_{23} is expressed in the following way,

$$F_{23} = \begin{cases} F_{23} = F_2, & \text{default setting} \\ F_{23} = F_2F_3, & \text{optional term for rough-wall flows} \end{cases} \tag{46}$$

where F_3 is used to prevent the SST limitation from being activated in the roughness layer in rough-wall flows [15], and is defined as follows,

$$F_3 = 1 - \tanh\left[(arg_3)^4\right], \tag{47}$$

and arg_3 is defined as,

$$arg_3 = \min\left(\frac{150\nu}{y^2\omega},\ 10\right), \tag{48}$$

where ν is a molecular kinematic viscosity and y is a distance to wall.

In order to properly define blending functions there are a number of constants which are necessary for a $k-\omega$ SST turbulence model to work properly. Those constants are evaluated in the following way,

$$\alpha_\mathrm{k} = F_1\left(\alpha_{\mathrm{k},1} - \alpha_{\mathrm{k},2}\right) + \alpha_{\mathrm{k},2}, \tag{49}$$

$$\alpha_\omega = F_1\left(\alpha_{\omega,1} - \alpha_{\omega,2}\right) + \alpha_{\omega,2}, \tag{50}$$

$$\beta = F_1\left(\beta_1 - \beta_2\right) + \beta_2, \tag{51}$$

$$\gamma = F_1\left(\gamma_1 - \gamma_2\right) + \gamma_2. \tag{52}$$

Furthermore, last terms are defined in the following way:

$$CD_{\mathrm{k},\omega+} = \max\left(CD_{\mathrm{k},\omega}, 10^{-10}\right), \tag{53}$$

$$CD_{\mathrm{k},\omega} = 2\overline{\rho}\alpha_{\omega,2}\frac{\nabla k \bullet \nabla\omega}{\omega}. \tag{54}$$

Coefficients necessary to close the system of equations are presented in the Table (1).

Table 1: $k-\omega$ SST turbulence model coefficients.

$\alpha_{\mathrm{k},1}$	$\alpha_{\mathrm{k},2}$	$\alpha_{\omega,1}$	$\alpha_{\omega,2}$	β_1	β_2	β^*	γ_1	γ_2	a_1	b_1	c_1
0.85	1.0	0.5	0.856	0.075	0.0828	0.09	5/9	0.44	0.31	1.0	10.0

2.4 Multiple Frames of Reference

If an unsteady fluid flow in an inertial frame of reference is observed from a moving frame, it appears to be steady with respect to the moving frame, hence a fluid flow inside of a turbomachinery is commonly rendered in a moving reference frame. If a flow is observed in a moving frame of reference, formulations for momentum conservation equation can be expressed by using either absolute or relative velocities as a dependent variables. Within the MRF approach inside of a `foam-extend` package, an absolute velocity formulation is used, since it does not require a transformation of the velocity vector at the interface between rotating zones, making the code easier to handle [16].

Relations between an arbitrary position vector $\mathbf{r}$ in stationary and moving frame can be summarised in the following way [8, 17] :

$$\left[\frac{\mathrm{d}\mathbf{r}}{\mathrm{d}t}\right]_{\mathrm{I}} = \left[\frac{\mathrm{d}\mathbf{r}}{\mathrm{d}t}\right]_{\mathrm{R}} + \boldsymbol{\omega} \times \mathbf{r}, \tag{55}$$

where $\boldsymbol{\omega}$ is an angular velocity vector, while subscripts I and R represent inertial and rotating frame, respectively.

According to the Equation (55), a well know relation between absolute velocity in an inertial (stationary) frame and its corresponding relative velocity in a moving reference frame is obtained,

$$\mathbf{u} = \mathbf{u}_{\mathrm{rel}} + \boldsymbol{\omega} \times \mathbf{r}. \tag{56}$$

In the absolute velocity formulation of the MRF approach, a centrifugal force term vanishes compared to the relative velocity formulation. Thus, only a Coriolis force terms appears as an additional source term. The flux in the convection term uses relative velocity which is calculated from mesh motion. Therefore, in the case of prescribed rotation, mesh flux is calculated directly from rotation and without mesh motion.

By using an MRF approach, there is no mesh motion and the computational domain remains fixed. Furthermore, accuracy of a fluid flow solution is acceptable for specific CFD purposes, while a calculation run time is drastically reduced compared to transient simulation.

2.4.1 Compressible Navier - Stokes Equations in the Rotating Frame

In general, turbomachinery problems involve both rotating and stationary parts. Thus, a computational domain needs to be split in separate cell zones, where each zone is assigned a corresponding angular velocity. If one defines a zero angular velocity for a stationary region, their corresponding governing equations in moving frame transform to stationary frame formulation. Thus, the Multiple Reference Frame (MRF) model approach is analogous to freezing the motion of the moving part in a specific position and observing the instantaneous flow field with rotor in that fixed position in space [17].

Governing equations for a compressible fluid flow in a rotating frame of reference used in the MRF model are defined in the [18] as:

- **conservation of mass**

$$\frac{\partial \rho}{\partial t} + \nabla \bullet (\rho \mathbf{u}) = 0, \tag{57}$$

- **conservation of linear momentum**

$$\frac{\partial (\rho \mathbf{u})}{\partial t} + \nabla \bullet (\rho \mathbf{u}_{\mathrm{rel}} \otimes \mathbf{u}) + \boldsymbol{\omega} \times (\rho \mathbf{u}) = -\nabla p + \nabla \bullet \boldsymbol{\tau} + \rho \mathbf{g}, \tag{58}$$

where a viscous stress tensor $\boldsymbol{\tau}$ is defined as follows:

$$\boldsymbol{\tau} = \mu \left[\nabla \mathbf{u} + (\nabla \mathbf{u})^T \right] - \frac{2}{3} \mu \nabla \bullet (\mathbf{u}) \mathbf{I}, \tag{59}$$

- **conservation of rothalpy** (absolute velocity formulation)

$$\nabla \bullet (\rho i \mathbf{u}_{\mathrm{rel}}) = -\nabla \bullet (\rho \omega r u_{\Theta} \mathbf{u}_{\mathrm{rel}}) - \nabla \bullet (p \mathbf{u}) + \nabla \bullet (\boldsymbol{\tau} \cdot \mathbf{u}) + \nabla \bullet (\lambda \nabla T) + S_{\mathrm{H}}. \tag{60}$$

2.5 Coupling of Non-Conformal Mesh Boundaries

In modern CFD, simulating a flow field around the complex geometry is a common case. Consequently, creating a high-quality mesh for a complex geometry is a very difficult task. In order to overcome these problems, one simple solution is to generate two separate mesh regions with mismatching patch nodes on both sides and connect them by means of a coupling interface. Therefore, mesh quality of both regions can be improved. Within the `foam-extend` CFD package, a General Grid Interface (GGI) [9] is used for coupling patches with mismatching topology.

2.5.1 General Grid Interface

Using the standard periodic boundaries where coupled patches share identical mesh topology is beneficial, but it is very often avoided in turbomachinery cases due to practical reasons. Since common turbomachinery cases involve highly twisted rotor blades, using the standard periodic boundaries would produce mesh of insufficient quality. In order to expand the possibilities of using periodic boundaries for turbomachinery purposes, a special feature for the non-conformal mesh boundaries coupling needs to be used. Within the `foam-extend` package, a General Grid Interface (GGI) [9] is used for treating the coupled patches with mismatching mesh topology in order to preserve a high-quality mesh for turbomachinery purposes.

GGI is a coupling interface used for joining two non-conformal regions where the patch nodes on each side of the interface do not match [9]. Due to common problems with preserving mesh quality in turbomachinery simulations, GGI is regularly used as a solution for that kind of cases.

Most turbomachinery cases involve periodic geometry patterns such as rotor blades. Thus it is possible to resolve the flow field by evaluating only one blade passage and taking the advantage of the periodic boundary conditions. By using the above-mentioned approach, the number of grid cells can be drastically reduced and consequently, results can be obtained in a shorter time period.

In cases where only one portion of an annulus is simulated, a practice is to generate mesh around the rotor blade with the halves of blade passages on both sides of a blade. Thus, one half of blade passage on a pressure side communicates with the other half of blade passage on a suction side of the blade via the GGI interface.

There are many derived forms of the GGI interface implemented in `foam-extend` that are based on the same algorithm, but for periodic geometry such as the NASA Rotor 67 turbofan case, a special derivative of GGI called `cyclicGGI` is used. The `cyclicGGI` is a variation of the basic GGI developed for handling periodic non-conformal mesh [9], which involves a coordinate transformation on a periodic boundary.

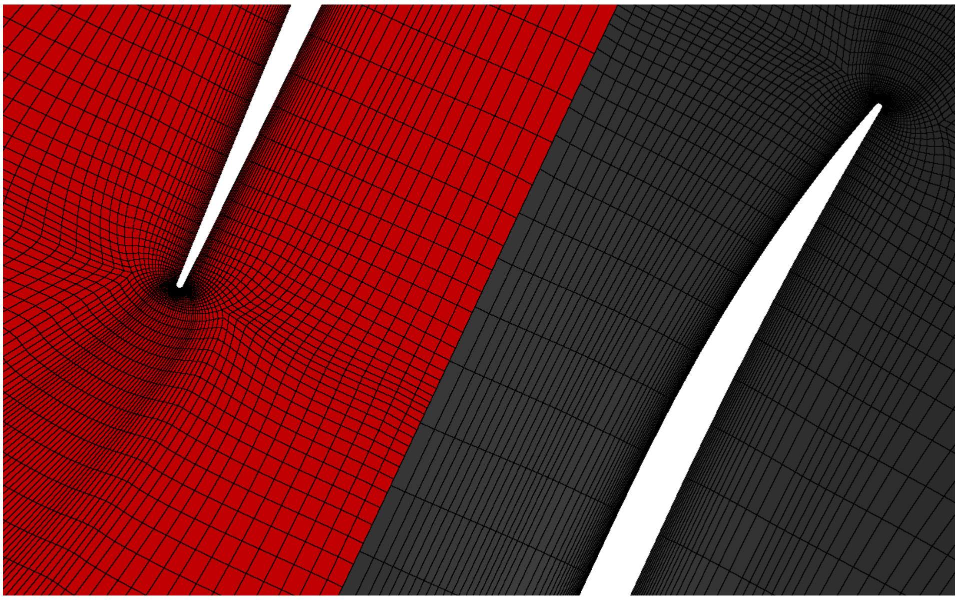

Figure 3: `cyclicGGI` interface.

Figure (3) represents the `cyclicGGI` interface used in this thesis. It is clear that the grid nodes on both sides of the interface do not match so the GGI interface is used for passing the information between the corresponding GGI pair.

2.6 Boundary Conditions

Boundary conditions are used to isolate the system from the external environment [5] and they are prescribed for each variable on each physical boundary of the analysed model. Generally, boundary conditions can be classified as either numerical or physical boundary conditions. Physical boundary conditions relate to the domain shape and are assigned to the characteristic parts of a domain boundary which is represented by a set of faces. Typical physical boundary conditions for CFD cases are inlet, outlet and wall. On the other hand, numerical boundary conditions are considered at the equation level [5]. Thus, due to imposed numerical boundary conditions on the boundaries of a numerical domain, the unique solution of the partial differential equation set can be obtained.
Numerical boundary conditions can be classified into:

- Dirichlet boundary condition
- von Neumann boundary condition

Dirichlet boundary condition specifies a fixed value of the variable at the certain boundary of numerical domain. Von Neumann boundary condition specifies the gradient of the variable normal to the boundary. It is a very common case that the zero gradient (no flux) of the variable is specified as the boundary condition. Additionally, there is also a number of mixed boundary conditions which represent a linear combination of the Dirichlet and von Neumann boundary condition.

Commonly, Dirichlet and von Neumann numerical boundary conditions are used in pair on the same boundary in order to solve Navier-Stokes equations. For example, if velocity is prescribed a Dirichlet (fixed value) boundary condition on the inlet boundary, a von Neumann boundary condition (zero gradient, no flux) is prescribed for the pressure on the same boundary. Additionally, velocity at the outlet boundary is assigned a von Neumann boundary condition, while the pressure at the same boundary is assigned a Dirichlet boundary condition. Thus, overall mass conservation is guaranteed by the pressure equation [10].

Furthermore, there are also some special boundary conditions that are related to the simplification and reduction of the computational domain and hence, required computational resources. Those boundary conditions are:

- Symmetry plane boundary conditions,
- Cyclic and periodic boundary conditions.

Symmetry plane boundary conditions can be used in cases where the geometry of interest and boundary conditions are symmetrical and if fluid flow is steady and symmetrical [5]. In such cases only a portion of the "whole domain" can be analysed without any consequences to the quality of obtained results.

Cyclic and periodic boundary conditions, on the other hand, are commonly used in cases of repeating geometry, where only a representative portion of the geometry is modelled [5]. The application of cyclic and periodic boundaries is common in turbomachinery simulation, where the fluid flow around a single rotor blade is modelled. Because of that both cyclic and periodic boundary condition principle is used within this thesis.

2.7 Closure

In this section a CFD mathematical model for solving steady, compressible, turbulent and transonic flow in rotating turbomachinery was presented. The mathematical model takes a form of coupled system consisting of conservation equation for mass, linear momentum and rothalpy. Since the realistic fluid flow is turbulent, a chosen framework for dealing with turbulent flow is RANS. To model Reynolds stresses within the RANS approach, a Boussinesq hypothesis of eddy viscosity was introduced along with the used $k-\omega$ SST turbulence model. MRF model that is used for obtaining steady-state solution of inherently unsteady turbomachinery flow is explained, along with the GGI interface that is needed for preserving a high-quality mesh inside of a turbomachinery passage. Subsequent section deals with the NASA Rotor 67 Turbofan.

3 NASA Rotor 67

This section covers the overview of NASA Rotor 67 axial-flow turbofan design and measured operating characteristics at near peak efficiency and near-stall operating point. Additionally, experimental procedure is briefly explained. For more details related to the experimental measurement technique, the reader is reffered to the Strazisar et al. [1].

3.1 Introduction

To meet the need for turbomachinery data that can be used for validation test cases for computational methods, the NASA Lewis Research Center has undertaken a program aimed at obtaining detailed measurements within transonic turbomachinery blade rows using laser anemometry method according to Strazisar et al. [1]. Because of that, since the late 1980s, those detailed experimental data serve for the validation of various CFD numerical codes for transonic turbomachinery flows. Flow patterns inside of high-speed turbomachinery are extremely complex, but transonic nature additionally increases the complexity on the greater level. More specifically, the flow inside of a NASA Rotor 67 axial-flow fan is transonic with shock waves, tip-leakage flow is present along with various vortices at the tip-gap and rotor blade trailing edge. Thus, it is a perfect candidate for examining the robustness of a CFD numerical codes developed for handling complicated transonic flows.

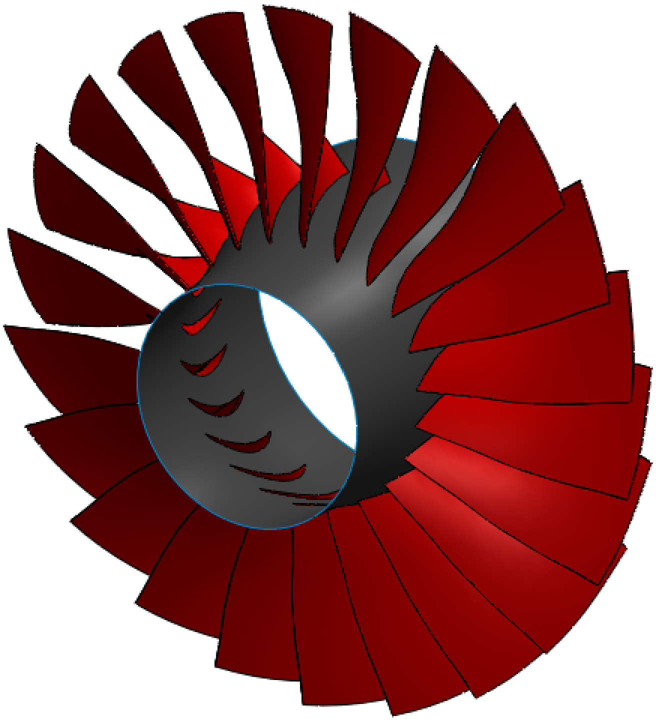

Figure 4: NASA Rotor 67 Transonic Turbofan.

3.2 NASA Rotor 67 Turbofan

NASA Rotor 67 is a high-speed, low aspect-ratio, transonic, axial-flow turbofan rotor developed to examine various three-dimensional phenomena inside of high-speed turbomachinery. Aspect-ratio refers to the ratio of blade height to blade chord. Turbofan is used as a first-stage rotor of a two-stage axial turbocompressor for a civil short-haul aircraft jet engine. Due to the availability of comprehensive experimental data from the NASA's study, it is widely used as a test case for the validation of the CFD codes for turbomachinery. NASA Rotor 67 turbofan is designed for an axial inflow and therefore it does not require inlet guide vanes. In accordance with NASA's survey, a steady compressible turbulent flow in NASA Rotor 67 turbofan without stator was analysed.

In Figure (4), NASA Rotor 67 turbofan is presented. It has 22 blades and its design mass flow rate at the nominal rotational speed of 16 043 revolutions per minute is 33,25 kg/s, while the achieved design total pressure ratio is 1,63. At the inlet, a reference total pressure and total temperature are 101 325 Pa and 288,15 K. Tangential velocity of the blade tip at the design operating point is 429 m/s and the resulting relative Mach number at the inlet tip is 1,38. There is a gap between a blade tip and a shroud of approximately 1 mm which is a source of tip loss due to tip leakage. Inlet diameter of a shroud is 0,514 m, while the outlet shroud diameter is 0,485 m. Inlet diameter of a hub is 0,193 m and the outlet diameter is 0,232 m. Design adiabatic efficiency is 93%. As stated by NASA, turbulence intensity at the fan inlet is 1,5%. Short summary of given data is presented in table 2.

Table 2: NASA Rotor 67 general operating data according to [1].

Parameter	**Value**
Number of blades, N	22
Rotational speed, n	16 043 rpm
Design mass flow rate, $\dot{m}$	$33,25$ kg/s
Design total pressure ratio, Π	$1,63$
Reference temperature, T_{ref}	$288,15$ K
Reference pressure, p_{ref}	101 325 Pa
Tangential velocity of the blade tip, u_{tip}	429 m/s
Turbulence intensity at the inlet, I	$1,5$ %
Tip relative Mach number, M_{rel}	$1,38$
Tip clearance	$1,016$ mm
Blade Aspect Ratio, AR	$1,56$
Adiabatic efficiency, η_{ad}	$0,93$

Experimental measurements were carried out by Strazisar et al. [1] for two design-speed operating conditions of rotor-only configuration. The first configuration is near-peak efficiency, while the second one is near-stall operating point. Within the experiment, a laser anemometer technique was used in order to obtain relevant tangential and axial velocities of the fluid flow through the turbofan, while the influence of radial velocity component was neglected according to their previous observations.

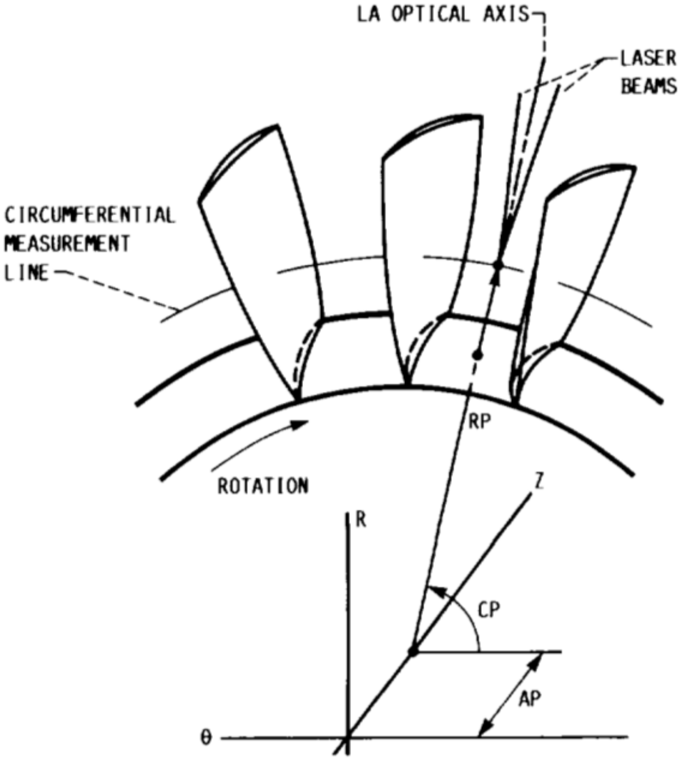

Figure 5: Definition of circumferential measurement line [1].

Measurements for each operating point were carried out at 50 points per single passage from blade-to-blade, along a fixed axial and radial location (on the circumferential measurement line). Figure (5) shows how measurement position points were defined. For each circumferential location, surveys were acquired at 30 axial locations on the 9 surfaces of revolution, which were spaced approximately every 10% of span from hub to tip.

As a result of the laser anemometer survey, obtained data was presented in the form of relative Mach number contour plots at 10%, 30% and 70% span (from shroud to hub) for both analysed operating conditions. Additionally, observed measured choke mass flow rate was 34,96 kg/s.

Aerodynamic survey probe stations, which relate to the other part of their measurement procedure, were positioned upstream and downstream of the rotor as shown in the Figure (6). The aerodynamic stations were used to gather radial distributions of total pressure and total temperature. According to the obtained radial distributions, the overall rotor row pressure ratio Π and adiabatic efficiency η_{ad} can be evaluated. Expression for adiabatic efficiency η_{ad} reads

$$\eta_{\mathrm{ad}} = \frac{\left(\dfrac{p_{02}}{p_{01}}\right)^{\frac{\kappa-1}{\kappa}} - 1}{\dfrac{T_{02}}{T_{01}} - 1}, \tag{61}$$

where κ is the specific heat ratio. Total pressure ratio Π is evaluated as,

$$\Pi = \frac{p_{02}}{p_{01}}. \tag{62}$$

In the above equations, subscript 1 denotes the inlet aerodynamic station conditions, while the subscript 2 denotes the outlet conditions, respectively. Overall aerodynamic performance of the turbofan is based on the appropriate averages of total pressure and total temperature radial distributions.

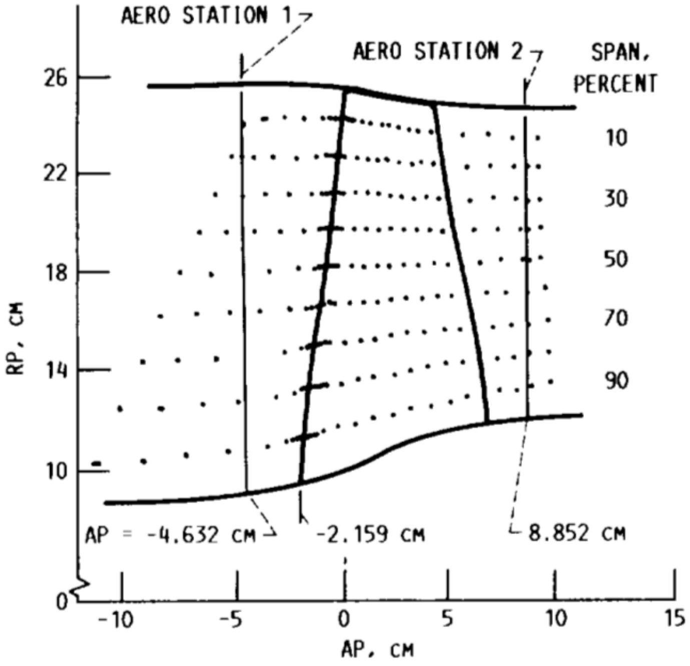

Figure 6: Laser anemometer and aerodynamic survey stations within the NASA Rotor 67 [1].

According to the experimental survey carried out by Strazisar et al., overall characteristics of the NASA Rotor 67 turbofan at the near-peak efficiency operating point are slightly different from the design parameters. Relevant data is summarised in the Table (3).

Table 3: Obtained performance data for near peak efficiency operating point [1].

Parameter	Value
Measured mass flow rate, $\dot{m}$	$34,573$ kg/s
Adiabatic efficiency, η	93%
Total pressure ratio, Π	$1,642$

Likewise, relevant data of measured characteristics for NASA Rotor 67 turbofan at the near-stall operating point is summarised in a Table (4).

Table 4: Obtained performance data for near stall operating point [1].

Parameter	Value
Measured mass flow rate, $\dot{m}$	$32,305$ kg/s
Adiabatic efficiency, η	$90,1\%$
Total pressure ratio, Π	$1,728$

According to the theory, operating point with lower mass flow rate achieves a greater total pressure ratio which was confirmed within the experiment. Thus, the mass flow rate in the near-stall operating point is lower, while the total-pressure ratio is greater. In addition, an adiabatic efficiency in the near-stall operating point is slightly lower. If one takes into account that the measured mass flow rate in the near-peak efficiency operating point is relatively close to choke, it is indicative that the analysed axial-flow NASA Rotor 67 has a narrow span of stable operating points.

3.3 Closure

In this section, a brief overview of NASA Rotor 67 axial-flow turbofan design characteristics was presented. Furthermore, basic informations related to the experimental procedure carried out by Strazisar et al. [1] were also presented. A summary of relevant performance data for both near-peak efficiency and near-stall operating point is presented in tabular form.

4 Geometry and Numerical Domain

This section covers the overview of preprocessing steps which are prerequisite in order to perform numerical simulations. Preprocessing steps consist of generation of the CAD model for NASA Rotor 67 turbofan along with the generation of spatially discretised grid of finite volumes based on the previously generated 3D CAD model.

4.1 Introduction

Performing a numerical simulation of a fluid flow inside of a complex geometry from scratch is time-consuming. In order to carry out a simulation, a few preprocessing steps have to be done. First, a corresponding CAD model has to be generated within a CAD package. In order to successfully accomplish the first step, one has to have in mind that the CAD generation for CFD purposes involves the introduction of certain CAD model simplifications, which do not effect the CFD solution, but largely simplify the subsequent mesh generation step. For that purpose, it is recommended to generate a clean, *watertight* geometry that consists of exclusively significant parts for the fluid flow. Based on the generated clean *watertight* CAD model, exported in one of the various neutral CAD formats, spatially discretised grid of finite volumes around the CAD model can be generated in the appropriate meshing software. Despite the growth of automatic meshing softwares and time-consuming process of manual meshing procedure, a manual meshing is still widely used due to drastically enlarged control over a complete grid.

This section is structured as follows: CAD model generation according to the literature [1] is explained and the output is presented within the Subsection (4.2), followed by the mesh generation process in Subsection (4.3). Generated mesh is presented in terms of various figures and finally, mesh quality is reported in the corresponding tabular form.

4.2 Geometry Generation

Comprehensive measured data obtained by the Strazisar et al. [1] were were presented so that the NASA Rotor 67 can be used as a validation test case for various turbomachinery CFD numerical codes. Thus, a detailed description of blade geometry and flowpath were provided in tabular form for the future analyses with CFD codes.

Hub and shroud represent the inner and outer surface that defines the turbofan's flow annulus. Since those surfaces are axisymmetric, they are defined by a simple distribution of points in the meridional *Z-R* plane, where *R* represents the radius of a point on the given surface, and *Z* represents its axial location. By revolving the created hub and shroud contour around the axis of rotation, hub and shroud surfaces are generated, and define the flow annulus. As their point distribution was quite dense, generated surfaces are very smooth.

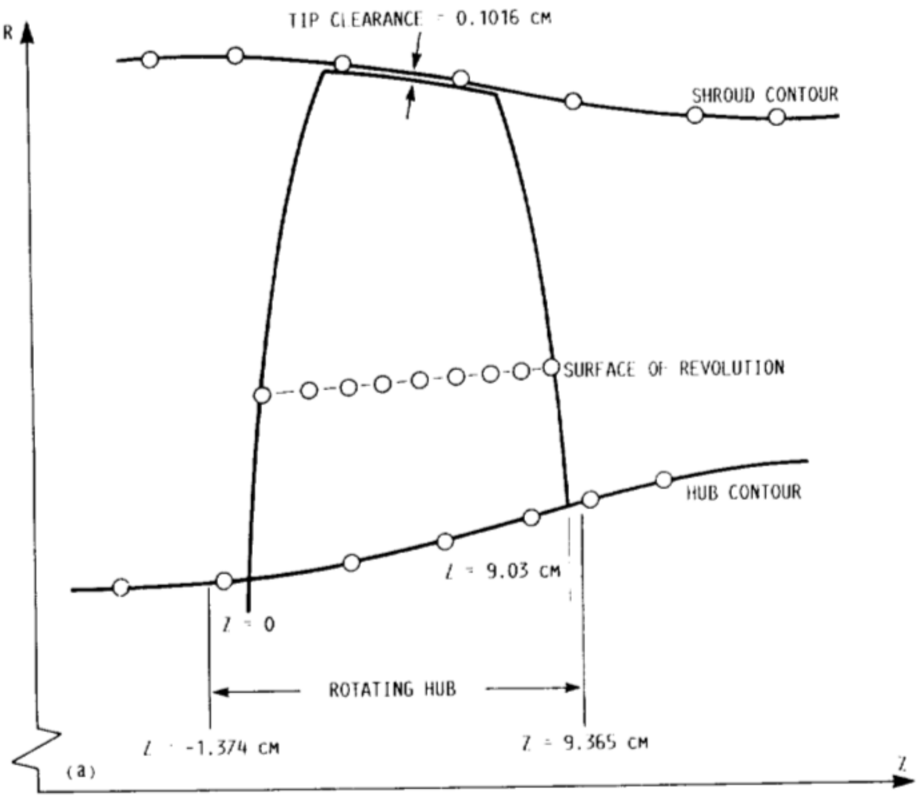

Figure 7: Definition of blade and flowpath geometry [1].

Rotor blade geometry is more complex than the hub and shroud contours. In the literature, a rotor blade is defined by a number of surfaces of revolution. Surface of revolution is defined with a number of points on the pressure and suction side with circles on a leading and trailing edge. Pressure and suction side points are defined in the cylindrical coordinate system in such way that two points (one on the suction and one on the pressure side) are described with the same axial and radial coordinate but different angular coordinate. There are 14 surfaces of revolution defined in the literature, hence a smooth CAD surface representation of a rotor blade can be generated. In the Figure (7) the meridional projection of geometry contours is presented.

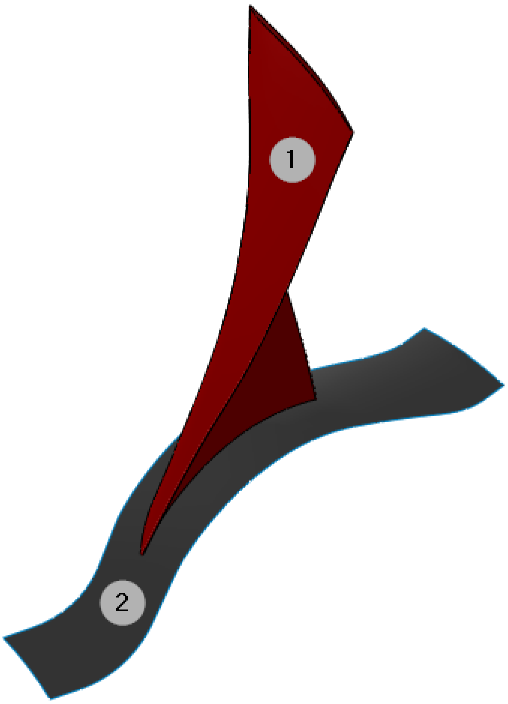

Figure 8: CAD model of a rotor blade and hub.

During the CAD generation process, one should have the idea of what the mesh would look like. Thus, a mesh generation process can be greatly eased. Figure (8) shows the CAD model representing the rotor blade and hub surfaces. If the concept of cyclic and periodic boundaries is used, there is no need to generate a CAD model of the full annulus with 22 blades. Instead, only one blade passage can be created. According to that, imaginary CAD surfaces that represent the periodic boundaries were created. Using this technique, the effort during the meshing process can be decreased.

Figure (9) shows the complete CAD surface model representation that consists of the inlet, outlet, shroud and periodic surfaces (hub and rotor blade are not visible), which define the outer boundaries for the grid of discretised finite volumes.

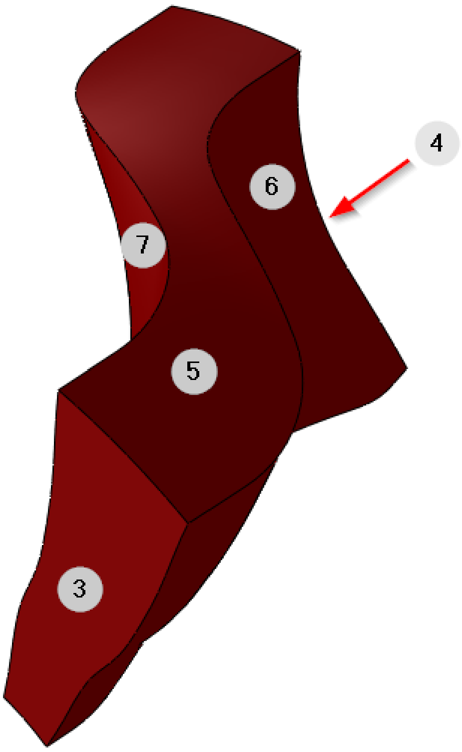

Figure 9: Complete NASA Rotor CAD model.

In Figures (8) and (9) a NASA Rotor 67 case topology is presented with the assigned patch ID numbers. Corresponding patch ID numbers which represent boundaries of the generated geometry and numerical domain accordingly, are presented in the table Tab. (5).

Table 5: Definition of patch topology for NASA Rotor 67 numerical simulation.

Patch ID	**Patch name**	**Patch type**
1	rotorBlade	`wall`
2	hub	`wall`
3	inlet	`patch`
4	outlet	`patch`
5	shroud	`wall`
6	rotorCyclic1	`cyclicGgi`
7	rotorCyclic2	`cyclicGgi`

For the purpose of NASA Rotor 67 turbofan CAD model generation, a commercial CAD package SolidWorks was used [19]. Generated CAD model was afterwards exported in the neutral .stl CAD format to be used with the meshing software.

4.3 Mesh Generation

Based on the generated CAD model, meshing was performed in the commercial meshing software Pointwise [20]. Pointwise is a meshing software for manual grid generation with various types of finite volume elements available (tetrahedra, hexahedra, prisms, pyramids). Generated mesh can be structured, unstructured or hybrid according to the used elements. Despite the fact that manual mesh generation users have a much greater control over each mesh segment during the mesh generation process, compared to automatic meshers. Mesh is generated on basis of the CAD model presented in previous subsection and simulations were carried out for a fixed rotor position by using the MRF approach. Additionally, special derivative of a GGI interface for coupling non-conformal periodic mesh boundaries called `cyclicGGI` was used which required special attention. Within this thesis, the generated mesh is a fully structured hexahedral mesh.

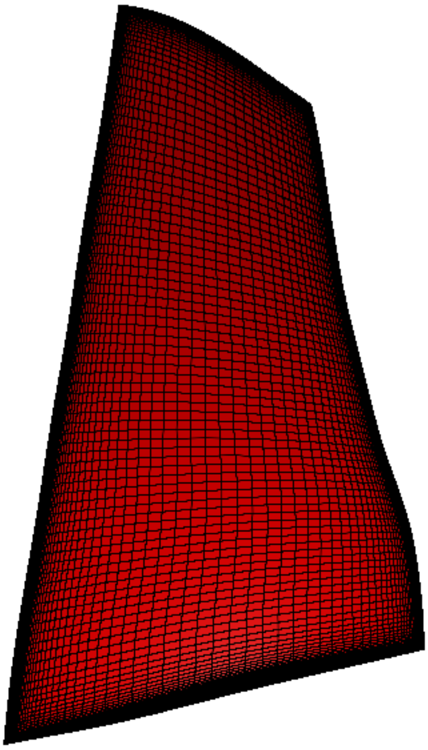

Figure 10: Surface mesh on the pressure side of a rotor blade.

Fully structured hexahedral meshes provide the best accuracy of numerical results and the numerical domain consists of decreased number of finite volume elements (cells), compared to its unstructured version. Computational demand is also decreased accordingly.

In the Figure (10), a surface mesh on the pressure side of a rotor blade is presented. As can be seen, the mesh resolution is quite dense, which is a prerequisite for accurate fluid flow solution. Rotor blade surface mesh consists of five segments: suction side, pressure side, leading edge, trailing edge and blade-tip mesh, and it is assigned a total of 21 500 structured quadrilateral surface elements.

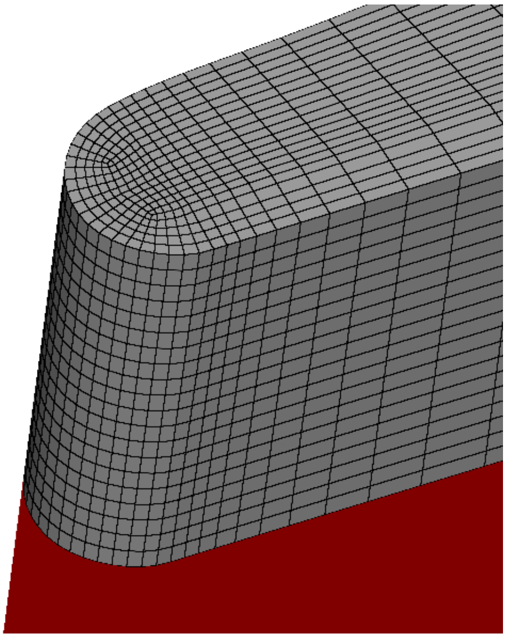

Figure 11: Detail of the tip-gap volume mesh near the leading edge.

Surface mesh on a blade-tip is smoothly generated and has a total of 3100 structured quadrilateral surface elements. On the leading and trailing edge, mesh is created using an O-H "butterfly" topology in order to preserve high-quality mesh. Blade-tip surface mesh is then used to fill a tip-gap with 20 cells in order to ensure high resolution of the tip-gap mesh and to capture details of tip-leakage flow and tip-gap vortices.

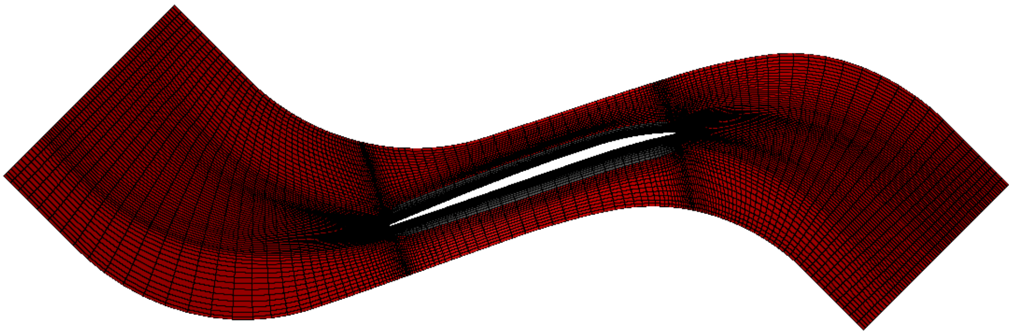

Figure 12: Surface mesh representation on the shroud of the NASA Rotor 67 turbofan passage.

In order to capture the flow field details, the first set of cells near the rotor blade is assigned a total of 20 smooth layers. First smooth volume grid block can be seen in Figures (12) and (13) and is coloured grey. The rest of the volume mesh was generated pretty straightforward.

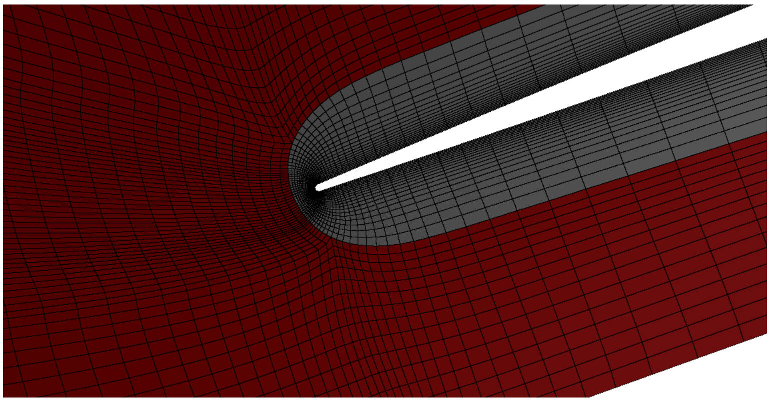

Figure 13: Detail of the surface mesh on the shroud near the leading edge.

Special attention was given to the `cyclicGGI` surface meshes. Since the NASA Rotor 67 has 22 rotor blades and only one blade passage was analysed, presented passage covers 1/22 portion of the complete flow annulus. Thus, the angle between the corresponding periodic patches rotorCyclic1 and rotorCyclic2 is 16,363636 degrees. As mentioned in the subsection 2.5.1, `cyclicGGI` interface is used in order to improve the mesh quality in the turbomachinery passages due to highly twisted rotor blades. This is achieved by allowing node mismatch on both sides of the coupling interface. Properly generated customized periodic surface meshes define the interior of the volume mesh in the acceptable way for turbomachinery flow analyses.

Surface mesh on the periodic boundary `rotorCyclic1` is shown in Figure (14). The other periodic boundary patch `rotorCyclic2` is generated in a similar way.

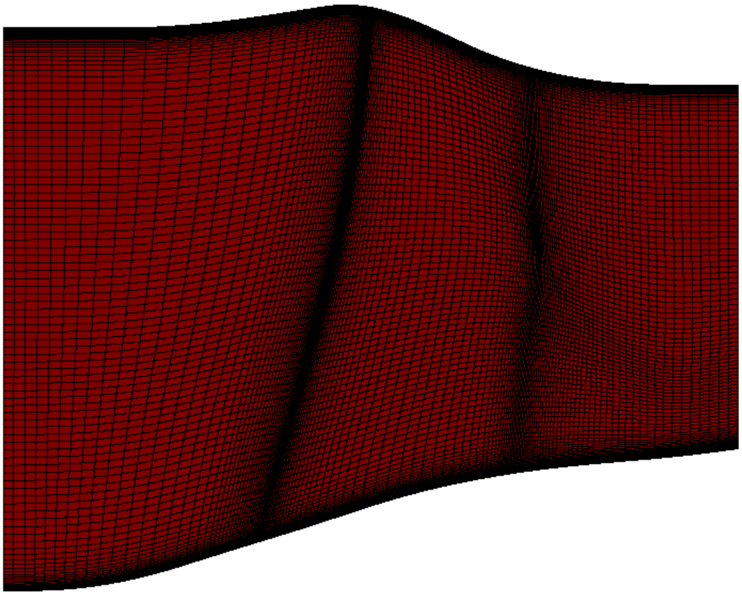

Figure 14: Surface mesh on the periodic boundary rotorCyclic1.

Generated volume mesh is a multi-block structured mesh which consists of several parts: tip-gap block, normally extruded smooth volume mesh around the rotor blade, pressure side block, suction side block, passage inlet block and passage outlet block. Quality assessment of the generated multi-block structured mesh was carried out by a `checkMesh` utility within the `foam-extend` CFD package, and based on the obtained report it satisfies all required criteria. Most important mesh quality assessment data is presented in the Table (6).

Table 6: Mesh quality assessment by `checkMesh` utility.

Parameter	**Value**
Number of cells	974 000
Max skewness	3,9
Max non-orthogonality	61,6
Max aspect ratio	149,6

4.4 Closure

Within this section, the overview of required preprocessing steps for numerical simulation is presented. First, the NASA Rotor 67 turbofan data extraction from the literature [1] and appropriate CAD model generation is explained. Appropriate figures of generated CAD are presented. On the basis of the previously generated 3D CAD model, a spatially discretised grid of finite volumes for numerical simulation is generated. Grid was generated within the commercial meshing software Pointwise and appropriate figures of characteristic mesh parts was presented accordingly. Basic information about the quality of the mesh was also presented in the corresponding tabular form. The subsequent section deals with the generated results for two analysed nominal speed operation points - for the near peak efficiency, and for the near stall opeating point.

5 Simulation Results

This section covers the presentation of obtained results for numerical simulations of flow inside the NASA Rotor 67 axial-flow turbofan. All numerical simulations were carried out on the mesh presented in Subsection (4.3).

5.1 Introduction

Numerical simulations of flow inside the NASA Rotor 67 turbofan were carried out for multiple operating points on the nominal angular velocity of 16 043 revolutions per minute. Detailed results in terms of graphical representation are presented at various axial and radial cross-sections for two operating points: for the nominal, near-peak efficiency and the near-stall operating point. The results of each numerical simulation were compared to the experimental data provided by Strazisar et al. [1] in terms of relative Mach number contour plots at 10%, 30% and 70% span measured from shroud. Other numerical simulation results were used in order to provide additional data to assemble a performance curve for the NASA Rotor 67 axial flow turbofan at nominal angular velocity in terms of $\Pi = \Pi\left(\dot{m}\right)$.

Subsection (5.2) covers the imposed boundary conditions for numerical simulations, while Subsections (5.3) and (5.4) cover the near-peak efficiency and the near-stall operating point results, respectively. Evaluated performance curve for the nominal angular velocity of the NASA Rotor 67 axial turbofan is presented in Subsection 5.5 and it is compared to the performance curve evaluated by measurements carried out by Strazisar et. al [1].

5.2 Boundary Conditions

In order to successfully and unambiguously solve the set of partial differential equations for fluid flow, there is a need to impose boundary conditions for each solved physical quantity on each boundary of the numerical domain, whereas boundaries are listed in the Table (5). Additionally, since the NASA Rotor 67 turbofan is rotating, the effect of rotation is taken into account by setting up an angular velocity for a `cellZone` consisting of a set of rotating cells. Within this thesis, the complete grid of finite volumes is assigned to the rotating `cellZone`.

Table (7) lists the imposed boundary conditions for pressure, velocity, rothalpy and temperature at the corresponding boundaries. Boundary conditions for each considered numerical simulation within this thesis were identical, except for the pressure boundary condition at the outlet boundary. By varying the outlet pressure, one can simply change the operating point of the axial-flow fan which yields different overall operating parameters such as total pressure ratio and mass flow rate. `timeVaryingMappedFixedValue` boundary condition is used as the outlet pressure boundary condition for all numerical simulations.

`timeVaryingMappedFixedValue` boundary condition allows mapping the pressure distribution along spanwise direction on the outlet boundary. Since the Strazisar et. al [1] provided the measured distribution of pressure along the spanwise direction on outlet boundaries for near-peak efficiency and near-stall operating point, those distributions were mapped on the outlet and used as pressure boundary conditions for corresponding numerical simulations. Pressure distribution for the near-peak efficiency operating point has a static pressure p of 101 558 Pa at the hub, while the shroud static pressure was set to 127 558 Pa. Area-averaged imposed static pressure was 120 000 Pa. On the other hand, near-stall operating point pressure distribution has a static pressure p of 104 730 Pa at the hub, while the shroud static pressure was set to 138 106 Pa. Area-averaged imposed static pressure was 127 160 Pa. Regarding the other numerical simulations, their outlet pressure distributions were set by scaling the near-peak efficiency pressure distribution.

Table 7: Imposed boundary conditions for pressure, velocity, rothalpy and temperature.

Patch	**Pressure BC**	**Velocity BC**	**Rothalpy BC**	**Temperature BC**
rotorBlade	`zeroGradient`	`fixedValue`	`zeroGradient`	`zeroGradient`
hub	`zeroGradient`	`fixedValue`	`zeroGradient`	`zeroGradient`
inlet	ITP	PDIOV	`fixedValue`	ITT
outlet	TVMFV	`inletOutlet`	`inletOutlet`	`inletOutlet`
shroud	`zeroGradient`	`fixedValue`	`zeroGradient`	`zeroGradient`
rotorCyclic1	`cyclicGgi`	`cyclicGgi`	`cyclicGgi`	`cyclicGgi`
rotorCyclic2	`cyclicGgi`	`cyclicGgi`	`cyclicGgi`	`cyclicGgi`

TVMFV – `timeVaryingMappedFixedValue`,
PDIOV – `pressureDirectedInletOutletVelocity`,
ITP – `isentropicTotalPressure`,
ITT – `isentropicTotalTemperature`.

`isentropicTotalPressure` boundary condition was imposed on the inlet boundary for all numerical simulations and the corresponding total pressure value was set to standard conditions of 101 325 Pa. Similar approach was used for the temperature at the inlet boundary. `isentropicTotalTemperature` boundary condition was used at the inlet with standard conditions of 288,15 K. Velocity boundary condition at the inlet boundary was set to `pressureDirectedInletOutletVelocity` which calculates the velocity vector from the flux according to the imposed inlet total pressure. Other boundary conditions are self-explanatory, where the `fixedValue` boundary conditions for velocity implies the no-slip boundary condition.

Boundary conditions for turbulent kinetic energy k on inlet and outlet patch boundaries were set to `turbulentIntensityKineticEnergyInlet`, where k is evaluated according to the corresponding magnitude of velocity vector. On the other hand, boundary condition for eddy turn-over time ω was set to `turbulentMixingLengthFrequencyInlet` on inlet and outlet patch boundaries. Wall functions were used on the `wall` type boundaries as boundary conditions for k and ω respectively, while the `cyclicGgi` was used on periodic boundaries.

5.3 Near Peak Efficiency Operating Point

This subsection presents the near peak efficiency operating point results obtained by the numerical simulation. Flow field representations are presented for physical quantities of interest at various radial and axial cross-sections of the numerical domain. Radial cross-sections were chosen according to the cross-sections with known relative Mach number contour plots presented in literature [1], and those are at 10%, 30% and 70% span measured from shroud. Chosen axial cross-sections for a detailed fluid flow analysis are presented in the Figure (15). If one introduce the axial length of a rotor blade, such as presented in the Figure (7), axial-cross sections 1 and 2 represent cross-sections 10% of the introduced axial length downstream and upstream of a rotor blade. Accordingly, axial cross-section 3, 4 and 5 represent cross-sections at the 30%, 50% and 70% of the rotor blade axial length measured from joint of rotor blade leading edge and hub.

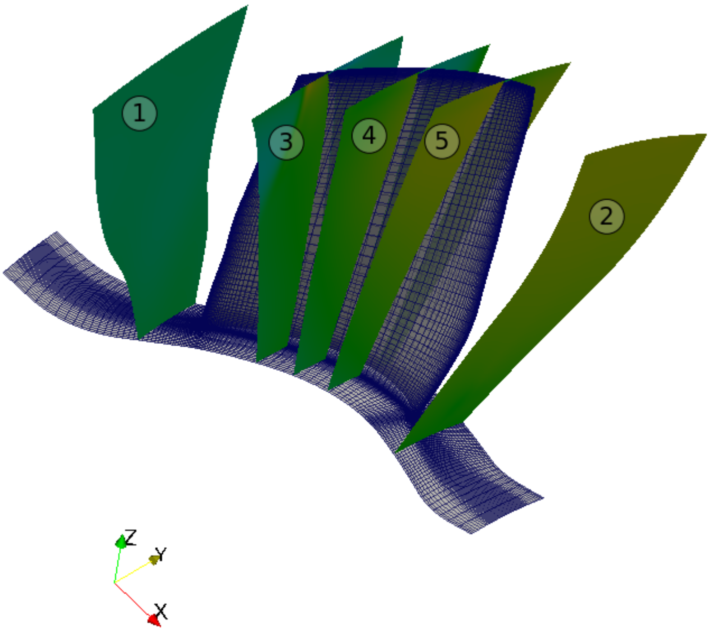

Figure 15: Position of analysed axial cross-section within the computational domain.

Relative Mach number is evaluated as a ratio of the local fluid relative velocity magnitude and the local speed of sound as follows:

$$M_{\mathrm{rel}} = \frac{|\mathbf{u}_{\mathrm{rel}}|}{a}, \tag{63}$$

where a is the local speed of sound which is evaluated in the following way,

$$a = \sqrt{\kappa R T}. \tag{64}$$

Despite the fact that only one passage was simulated, all presented figures show two passages. The reason for that is to indirectly observe the functionality of `cyclicGgi` interpolation interface for coupling of non-conformal mesh boundaries, and be able to compare it with experimental data.

- **Cross-section at 10% span from shroud**

Subsequent figures represent flow field quantities at the cross section located at 10% span from shroud. Figure (16) shows the comparison of relative Mach number contour plots from the experiment and from the numerical simulation. There is a good agreement between presented values in Figure (16a) and Figure (16b).

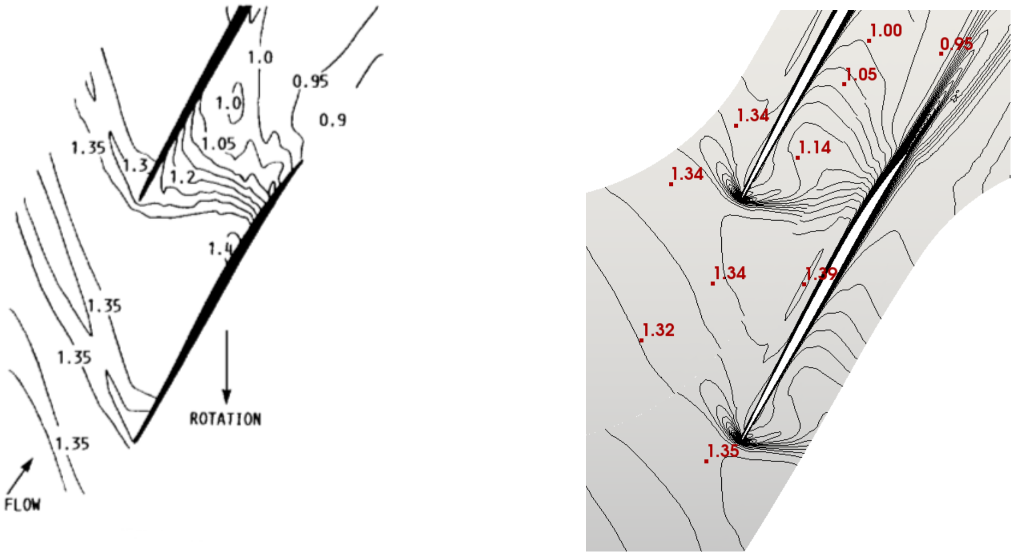

(a) Experiment [1]. **(b)** Numerical simulation.

Figure 16: Comparison of relative Mach number contour plots from experiment and numerical simulation at 10% span from shroud for the near peak efficiency operating point.

Figure (17) presents the pressure and temperature field representation at the 10% span from shroud obtained for the nominal, near peak efficiency operating point. Static pressure at the pressure side of the rotor blade gradually increases in the streamwise direction, which ensures proper working conditions for a turbofan. Figure (17b) shows the corresponding temperature field in the blade passage, which follows the pressure contours according to the equation of state for the ideal gas. Thus, lower temperature values occur on the suction side of the rotor blade where static pressure is lower. Higher temperature values occur on the pressure side of the rotor blade, where the static pressure values are higher respectively.

Figure (18) presents the magnitude of absolute velocity vector and relative Mach number field representation at the 10% span from shroud obtained for the near peak efficiency operating point. Since the velocity field in turbomachinery is often presented in terms of relative Mach number, the same principle is used within this thesis accordingly. Additionally, velocity field can be more clearly interpreted with respect to the relative velocity field. Relative Mach number field at the considered cross-section shows that the NASA Rotor 67 turbofan's inflow appears to have supersonic flow conditions in terms of relative velocity. Furthermore, the flow through blade passages is transonic, while the outflow is subsonic. Relative Mach number field, indirectly representing the relative velocity, is in accordance with the pressure field presented in Figure (17a). It can be observed that the relative Mach number is significantly lower in the turbulent wake downstream of the rotor blade row, compared to its surroundings.

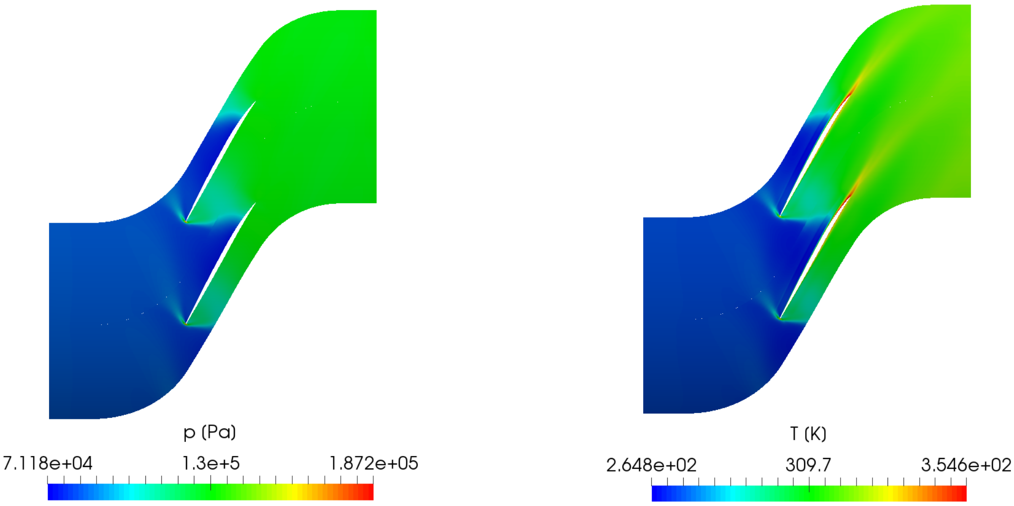

(a) Pressure field.

(b) Temperature field.

Figure 17: Pressure and temperature field representation at the 10% span from shroud for the near peak efficiency operating point.

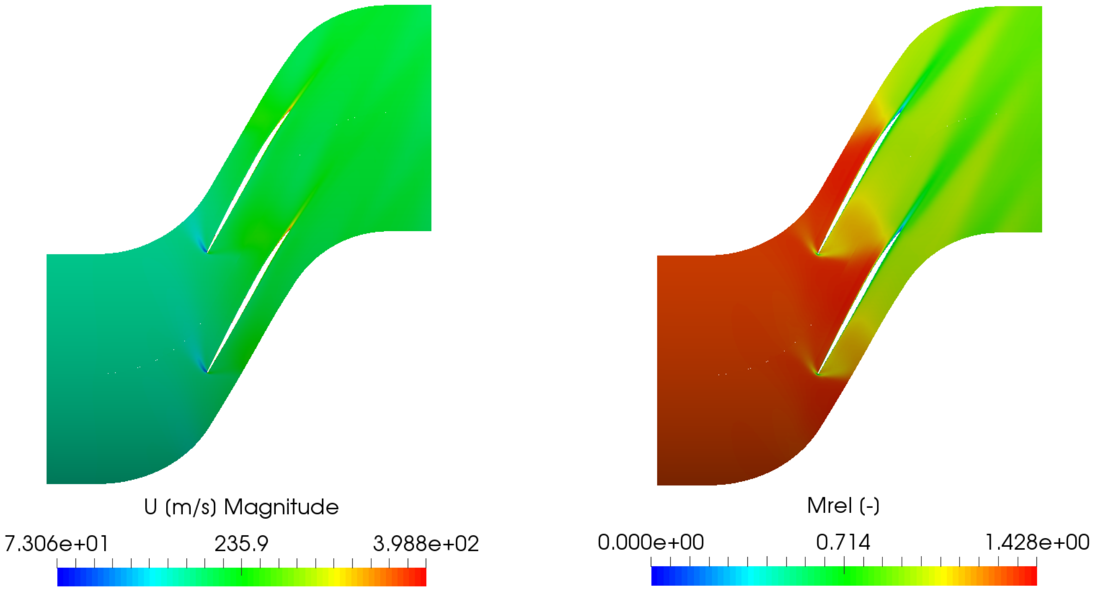

(a) Velocity field. **(b)** Relative Mach number field.

Figure 18: Velocity and relative Mach number field representation at the 10% span from shroud for the near peak efficiency operating point.

Figure (19) presents the turbulent kinetic energy and turbulent viscosity field representation at the 10% span from shroud obtained for the near peak efficiency operating point. It can be seen that the fluid flow is highly turbulent downstream of rotor blades. Turbulent wake spreading downstream of the rotor blade row can be clearly seen and correctly traverses the `cyclicGgi` interfaces.

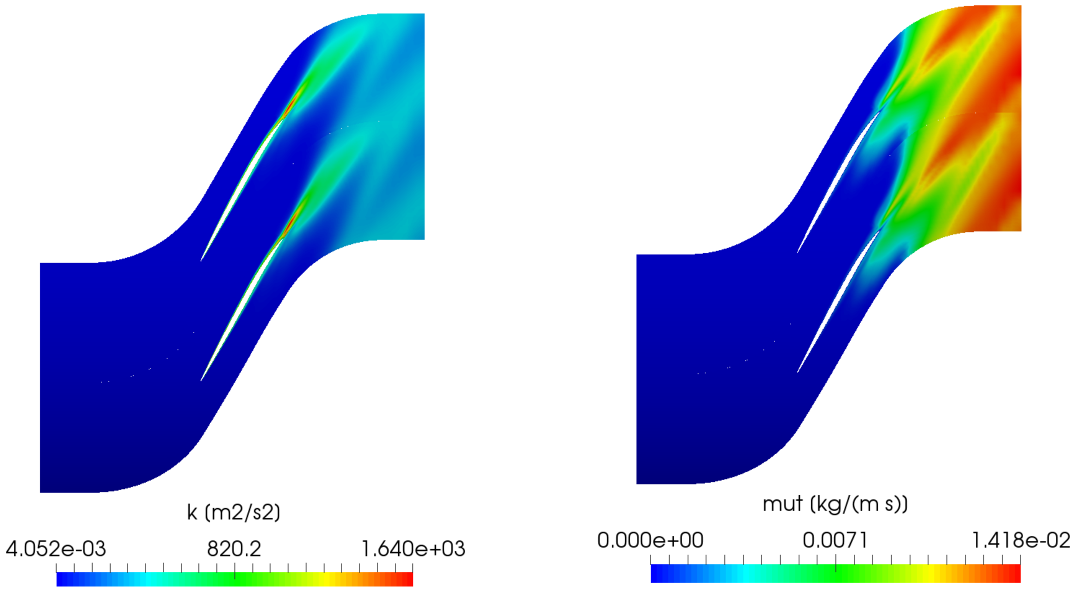

(a) Turbulent kinetic energy field. **(b)** Turbulent viscosity field.

Figure 19: Turbulent kinetic energy and turbulent viscosity field representation at the 10% span from shroud for the near peak efficiency operating point.

In order to additionally compare numerical simulation results with reference experimental data, the blade-to-blade plots of relative Mach number were presented. In Figure (20) a relative Mach number was presented as a function of pitch percentage (percentage of distance between two adjacent blades in the annulus), while the considered cross-section is the 50% of axial chord at the 10% span from shroud. As can be seen, there is a good agreement between numerical simulation and experiment for the lower values of pitch percentage (near the suction side of the rotor blade in the blade passage) in contrast to the higher pitch percentage values.

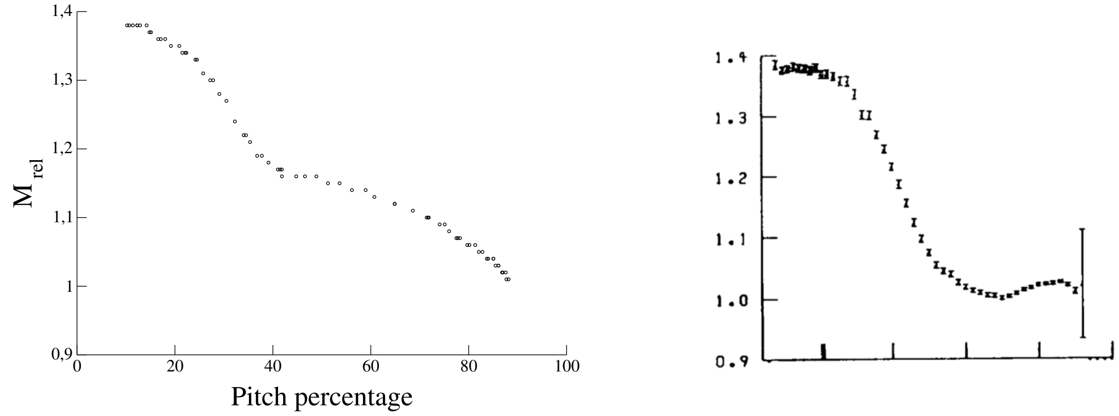

(a) Numerical simulation. **(b)** Experiment [1].

Figure 20: Blade-to-blade comparison of relative Mach number plots between numerical simulation and experiment for 50% axial chord at the 10% span cross-section for the near-peak efficiency operating point.

- **Cross-section at 30% span from shroud**

Subsequent figures represent flow field quantities at the cross-section located at 30% span from shroud, but flow field representations do not significantly differ compared to the preceding cross-section. Figure (21) shows the comparison between relative Mach number contours from the experiment and those obtained in the numerical simulation. As can be seen, there is again a good agreement between presented values on Figures (21a) and (21b) representing experiment and numerical simulation.

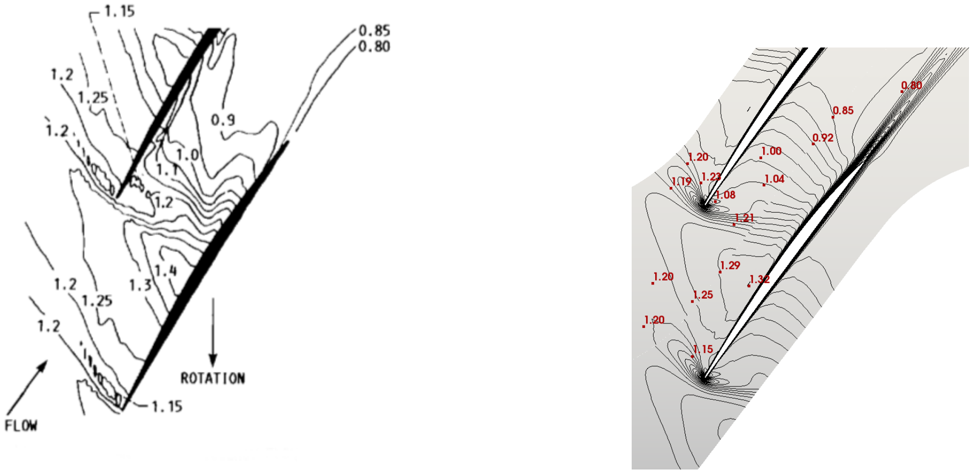

(a) Experiment [1]. **(b)** Numerical simulation.

Figure 21: Comparison of relative Mach number contour plots of experiment and numerical simulation at 30% span from shroud for the near peak efficiency operating point for the near peak efficiency operating point.

Figure (22) presents the pressure and temperature field. Again, a low pressure region smoothly spreads across the suction side of the rotor blade followed by a low temperature.

Figure (23) presents the magnitude of absolute velocity vector and relative Mach number field representation. Relative Mach number field at the considered cross-section shows that the NASA Rotor 67 turbofan's inflow appears to have supersonic flow conditions in terms of relative velocity. Additionally, the flow through blade passages is transonic, while the outflow is subsonic.

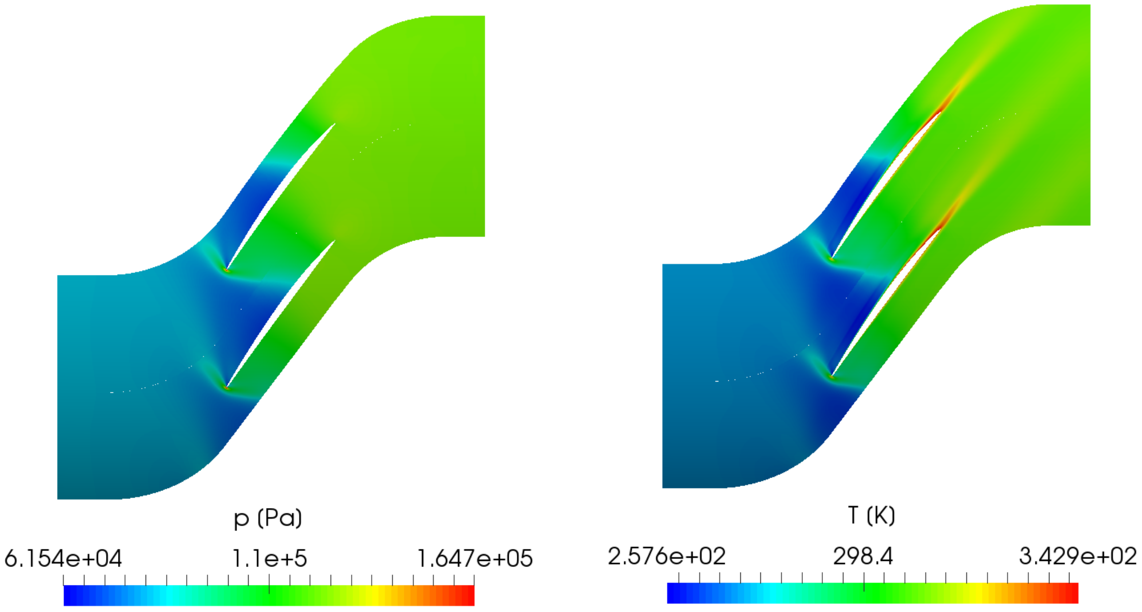

(a) Pressure field.

(b) Temperature field.

Figure 22: Pressure and temperature field representation at the 30% span from shroud for the near peak efficiency operating point.

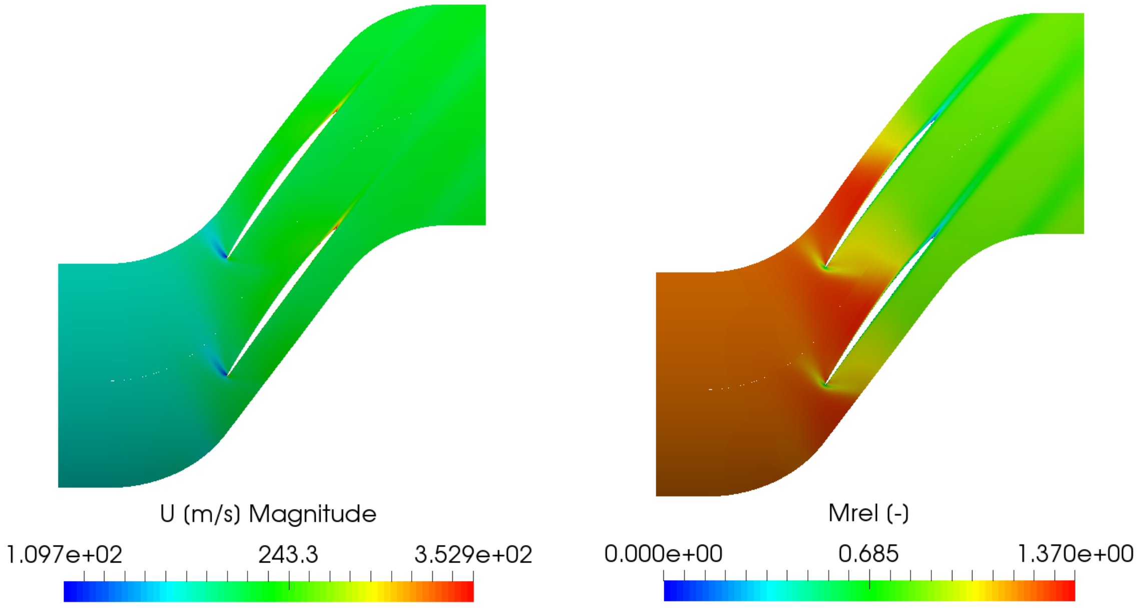

(a) Velocity field.

(b) Relative Mach number field.

Figure 23: Velocity and relative Mach number field representation at the 30% span from shroud for the near peak efficiency operating point.

Figure (24) presents turbulent kinetic energy and turbulent viscosity field representation at the 30% span from shroud obtained for the near peak efficiency operating point. It can be seen that the fluid flow is highly turbulent downstream of rotor blades. Turbulent wake spreading downstream of rotor blade row appears again.

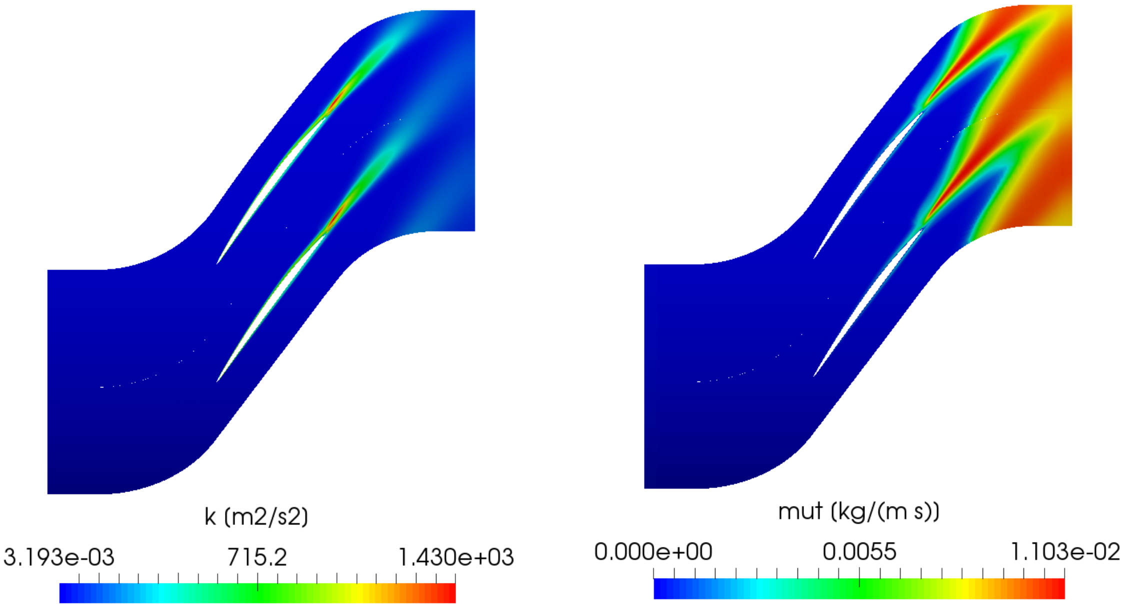

(a) Turbulent kinetic energy field.

(b) Turbulent viscosity field.

Figure 24: Turbulent kinetic energy and turbulent viscosity field representation at the 30% span from shroud for the near peak efficiency operating point.

Figure (25) shows a relative Mach number as a function of pitch percentage at the 50% of axial chord cross-section at the 30% span from shroud. As can be seen, agreement between numerical simulation results and experiment is very low.

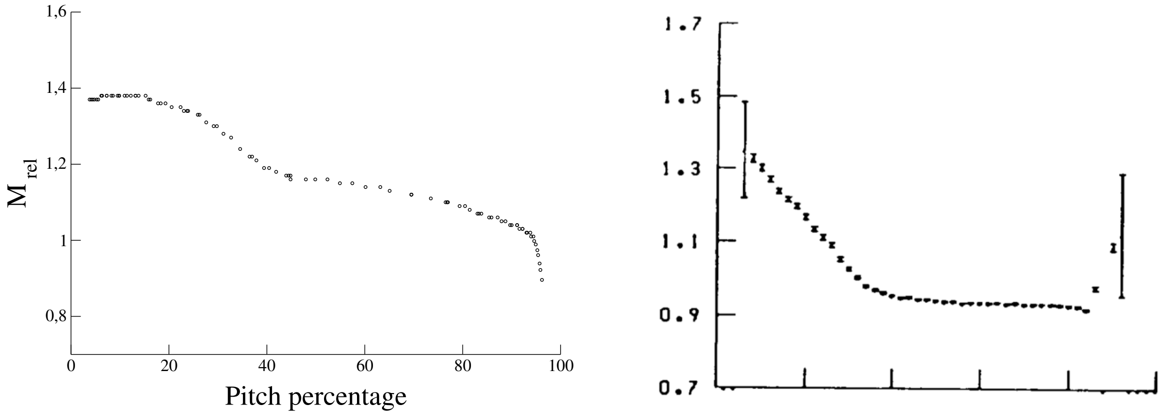

(a) Numerical simulation.

(b) Experiment [1].

Figure 25: Blade-to-blade comparison of relative Mach number plots between numerical simulation and experiment for 50% axial chord at the 30% span cross-section for the near-peak efficiency operating point.

- **Cross-section at 70% span from shroud**

Subsequent figures represent the flow field quantities at the cross-section located at 70% span from shroud for the near-peak efficiency operating point. The comparison between the relative Mach number contours in the experiment with those obtained in the numerical simulation is shown in Figure (26). Good agreement in relative Mach number values can be noticed on Figures (26a) and (26b) representing experiment and numerical simulation.

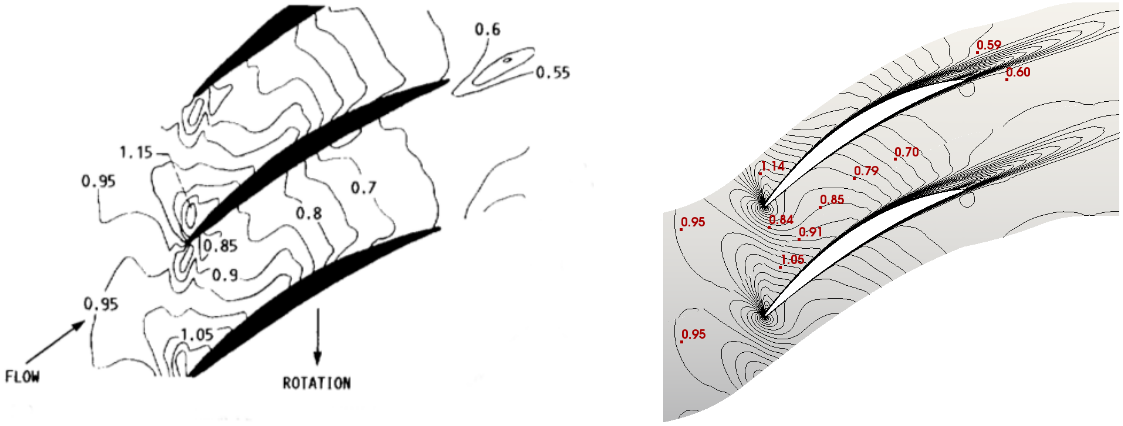

(a) Experiment [1]. **(b)** Numerical simulation.

Figure 26: Comparison of relative Mach number contour plots of experiment and numerical simulation at 70% span from shroud for the near peak efficiency operating point.

The pressure and temperature field is shown in Figure (27). Low pressure region is located only locally on a suction side in vicinity of the rotor blade leading edge, and is followed by a low temperature region. Emphasized high pressure region is located on the pressure side of the rotor blade. In contrast to the temperature fields at preceding cross-sections, a relatively high temperature of the fluid in the turbulent wake spreading downstream of the rotor blade can be observed. Figure (28) shows the absolute velocity and relative Mach number field. Relative Mach number field at the 70% span cross-section shows that the NASA Rotor 67 turbofan's inflow appears to have supersonic flow conditions. Furthermore, the flow through blade passages is transonic, while the outflow is subsonic.

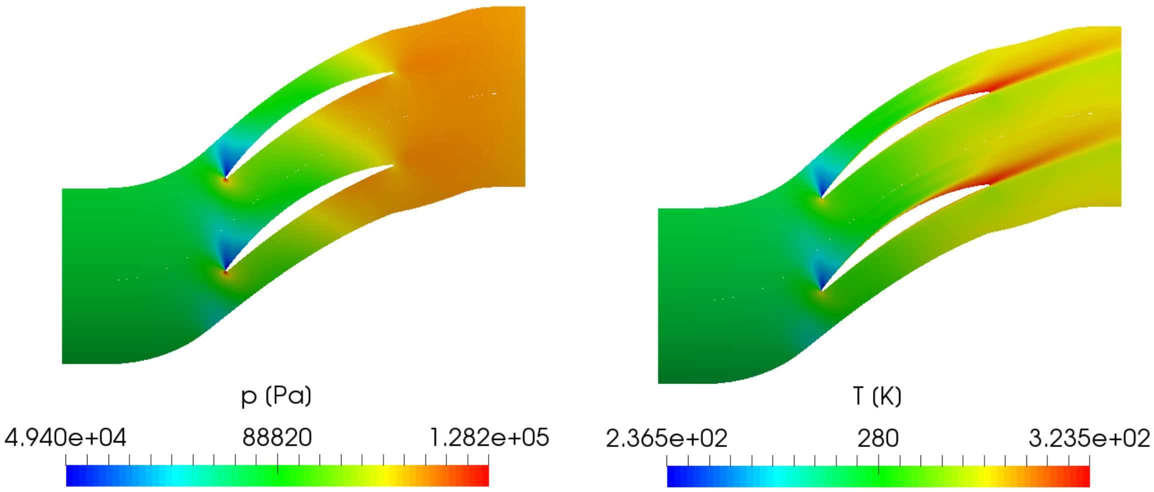

(a) Pressure field.

(b) Temperature field.

Figure 27: Pressure and temperature field representation at the 70% span from shroud for the near peak efficiency operating point.

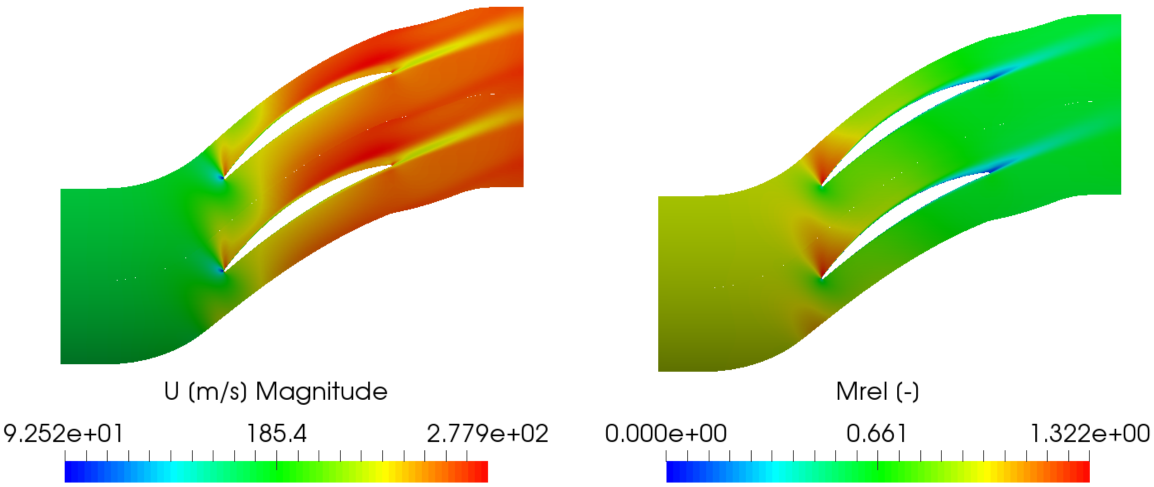

(a) Velocity field.

(b) Relative Mach number field.

Figure 28: Velocity and relative Mach number field representation at the 70% span from shroud for the near peak efficiency operating point.

Figure (29) shows the turbulent kinetic energy and turbulent viscosity field at the 70% span from shroud obtained for the near peak efficiency operating point. It can be seen that the fluid flow is highly turbulent downstream of rotor blades. Turbulent wake spreads downstream of the rotor blade row and the presence of fluid flow separation on the suction side can be observed.

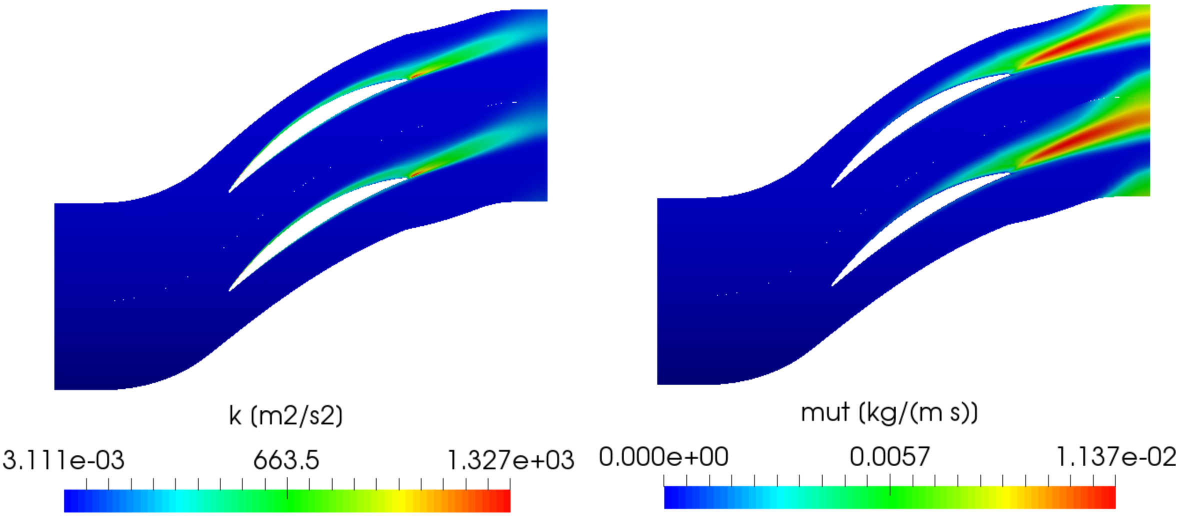

(a) Turbulent kinetic energy field.

(b) Turbulent viscosity field.

Figure 29: Turbulent kinetic energy and turbulent viscosity field representation at the 70% span from shroud for the near peak efficiency operating point.

Figure (30) shows a relative Mach number as a function of pitch percentage at the 50% of axial chord cross-section at the 30% span from shroud. As can be seen, agreement between numerical simulation results and experiment is very high.

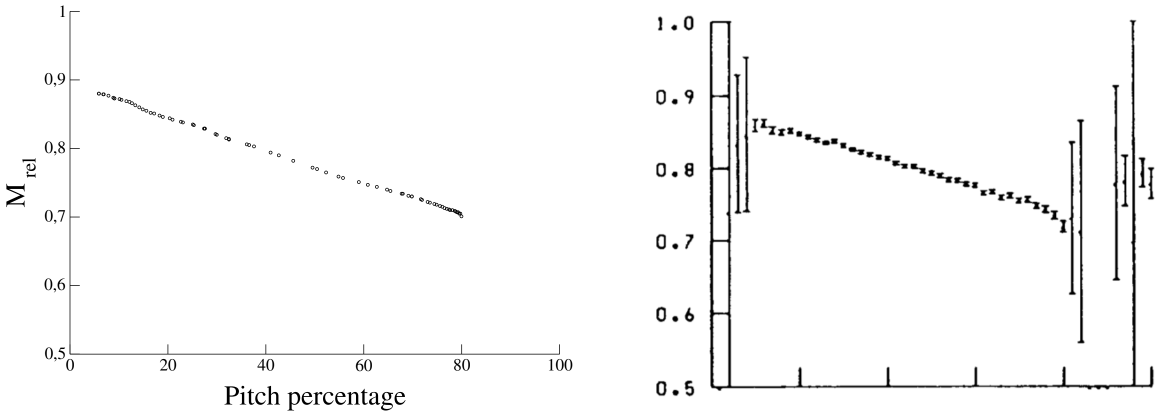

(a) Numerical simulation.

(b) Experiment [1].

Figure 30: Blade-to-blade comparison of relative Mach number plots between numerical simulation and experiment for 50% axial chord at the 70% span cross-section for the near-peak efficiency operating point.

- **Axial cross-section upstream of the rotor blade** (cross-section 1 on Figure (15))

Subsequent Figures (31) and (32) present profiles of pressure, temperature, velocity and relative Mach number at the cross-section upstream of the rotor blade. It can be observed that fluid flow quantities are almost undisturbed, except for the pressure field presented in Figure (31a) where the influence of low pressure region at the suction side of the rotor blade is visible.

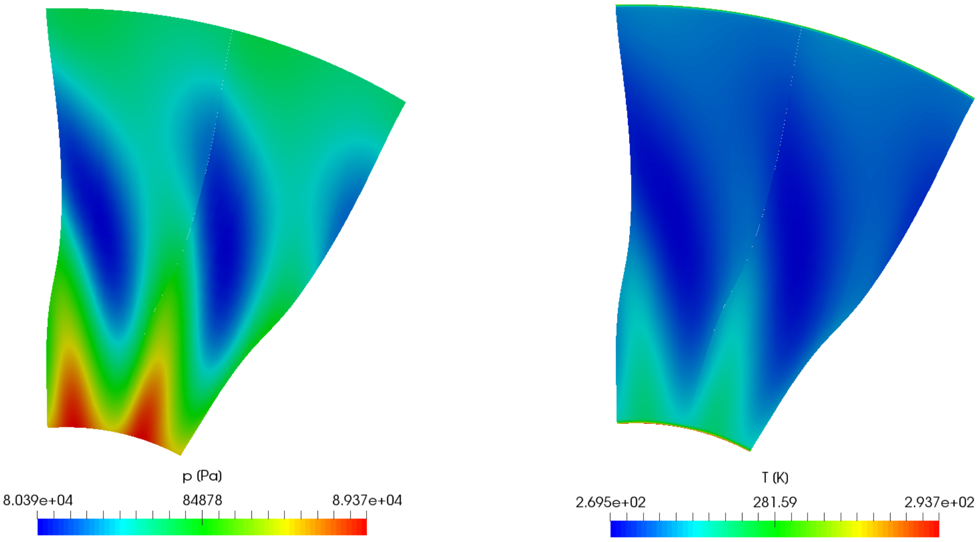

(a) Pressure field.

(b) Temperature field.

Figure 31: Pressure and temperature field representation at the axial cross-section upstream of the rotor blade leading edge for the near peak efficiency operating point.

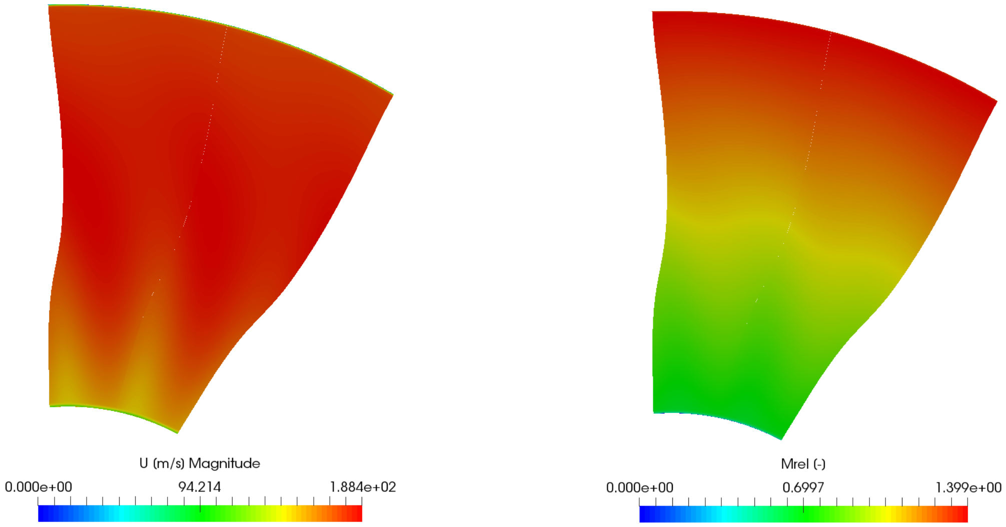

(a) Velocity field.

(b) Relative Mach number field.

Figure 32: Velocity and relative Mach number field representation at the axial cross-section upstream of the rotor blade for the near peak efficiency operating point.

- **Axial cross-section downstream of the rotor blade** (cross-section 2 on Figure (15))

Subsequent Figures (33) and (34) show profiles of pressure, temperature, velocity and turbulent kinetic energy at the cross-section downstream of the rotor blade. It can be observed that fluid flow quantities are completely influenced by turbulent wake spreading downstream of the rotor blade trailing edge. Furthermore, the existence of a trailing edge vortex is clearly demonstrated in the Figure (34b).

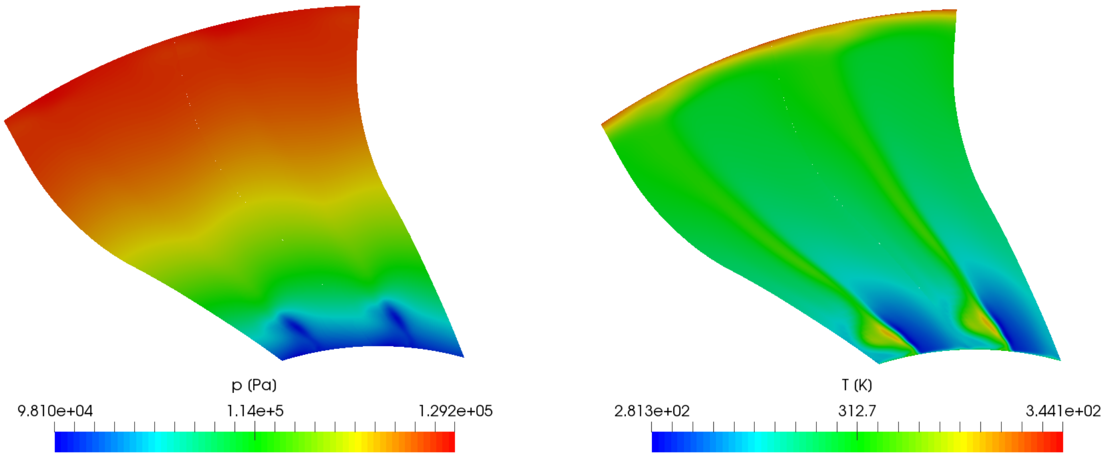

(a) Pressure field. **(b)** Temperature field.

Figure 33: Pressure and temperature field representation at the axial cross-section downstream of the rotor blade for the near peak efficiency operating point.

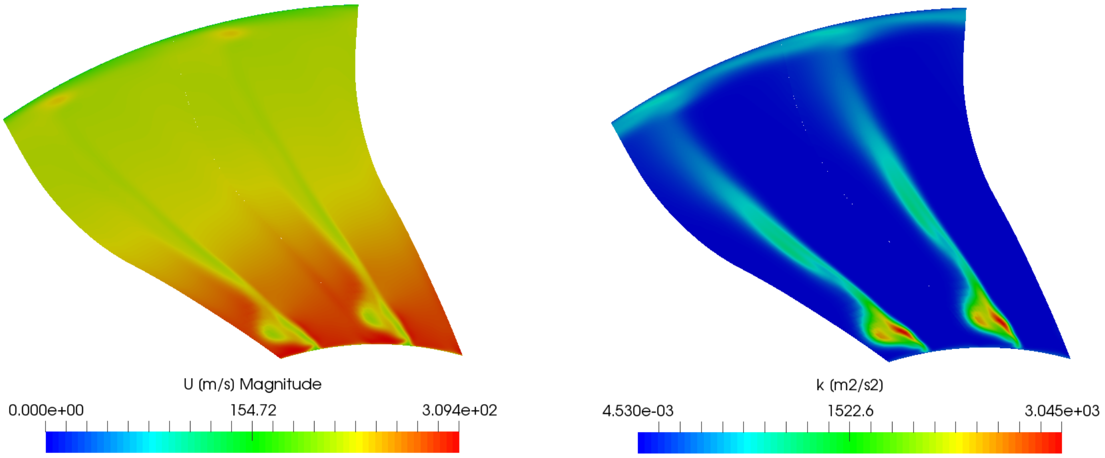

(a) Velocity field. **(b)** Turbulent kinetic energy field.

Figure 34: Velocity and turbulent kinetic energy field representation at the axial cross-section downstream of the rotor blade for the near peak efficiency operating point.

- **Axial cross-section 3** (presented on Figure (15))

The following Figures (35 - 38) present profiles of pressure, velocity, temperature, turbulent kinetic energy and turbulent viscosity field at the cross-section 3, respectively. Pressure, temperature and velocity field are presented alongside with the detail of fluid flow in the tip-gap. Figure (35a) shows the low-pressure region spreading through the blade passage from the suction side of one blade, to the vicinity of the subsequent rotor blade in the annulus. The reason for such pressure distribution is the location of the cross-section in the vicinity of the rotor blade leading edge, which is characterised by the emphasized low-pressure region at the suction side.

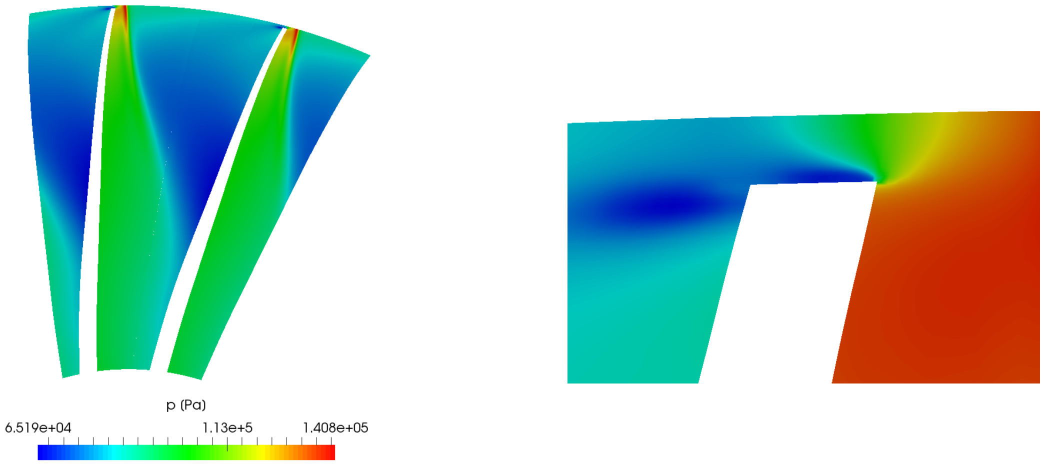

(a) Pressure field. **(b)** Detail of the pressure field in the tip-gap.

Figure 35: Pressure field representation at the axial cross-section 3 for the near peak efficiency operating point.

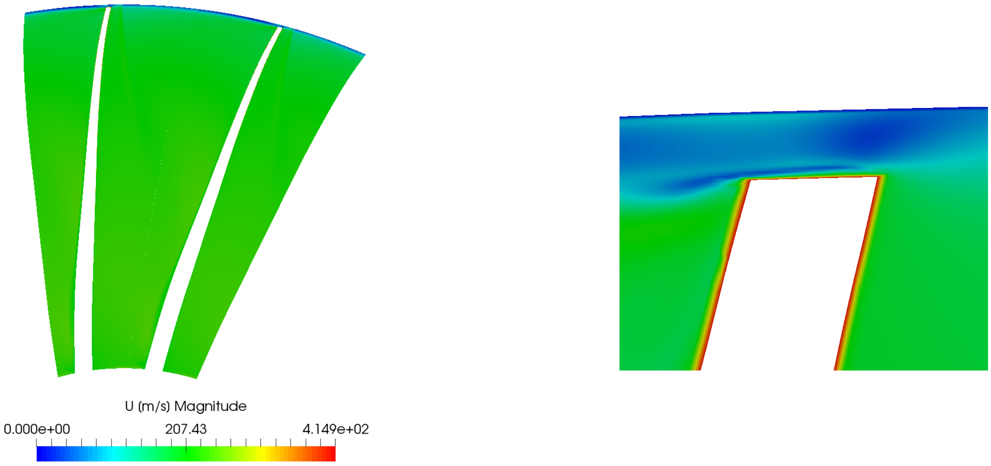

(a) Velocity field. **(b)** Detail of the velocity field in the tip-gap.

Figure 36: Velocity field representation at the axial cross-section 3 for the near peak efficiency operating point.

Detail of the pressure field in the tip-gap presented in Figure (35b) shows the exact location of the fluid flow separation point at the blade tip which causes the tip-leakage flow. Figure (37b) shows the temperature field at the axial cross-section 3 which follows the pressure field distribution. Turbulent kinetic energy and turbulent viscosity fields are presented in Figure (38a).

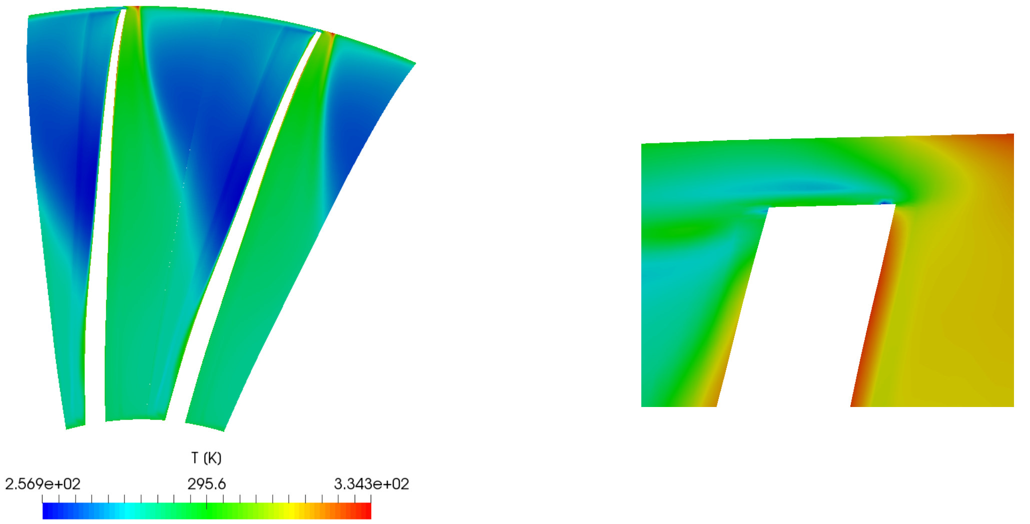

(a) Temperature field. **(b)** Detail of the temperature field in the tip-gap.

Figure 37: Temperature field representation at the axial cross-section 3 for the near peak efficiency operating point.

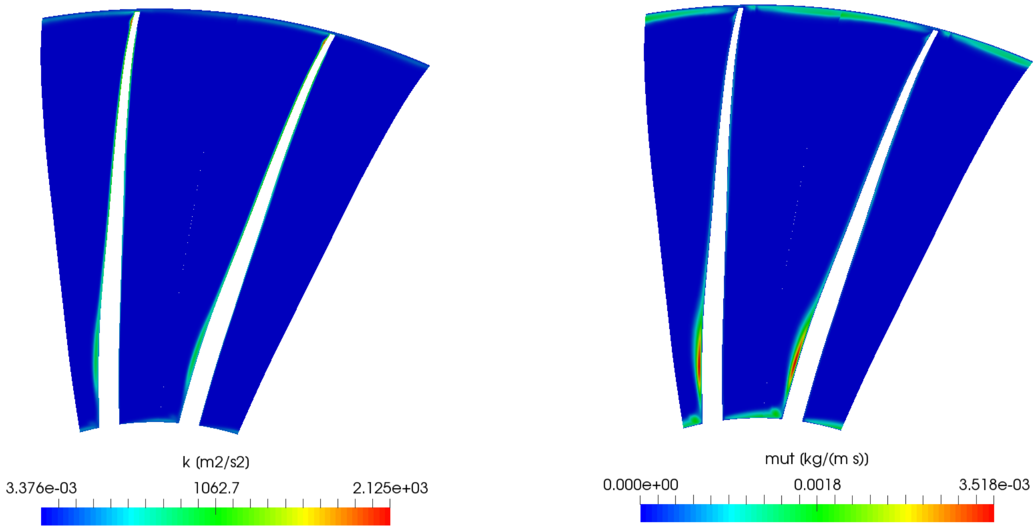

(a) Turbulent kinetic energy. **(b)** Turbulent viscosity.

Figure 38: Turbulent kinetic energy and turbulent viscosity field representation at the axial cross-section 3 for the near peak efficiency operating point.

Figures (39) and (40) show the details of Mach number and relative Mach number field in the tip-gap of the axial cross-section 3 for the near peak efficiency operating point. Figure (40) additionally presents the relative velocity vectors in the tip-gap in order to visualise a tip-leakage flow from pressure to the suction side of a rotor blade.

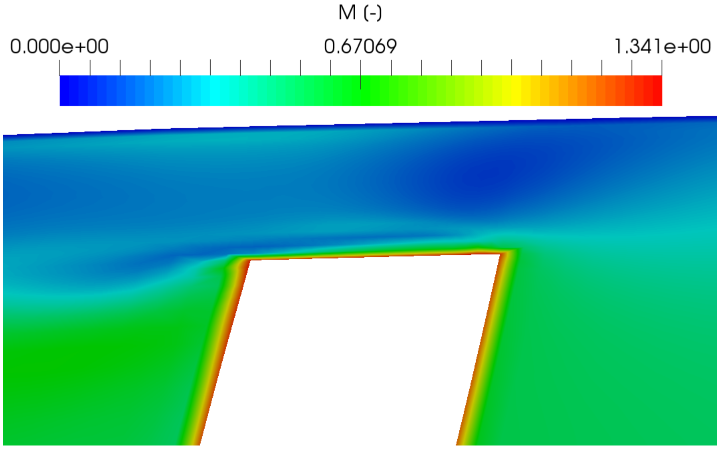

Figure 39: Details of Mach number field at the axial cross-section 3 for the near peak efficiency operating point.

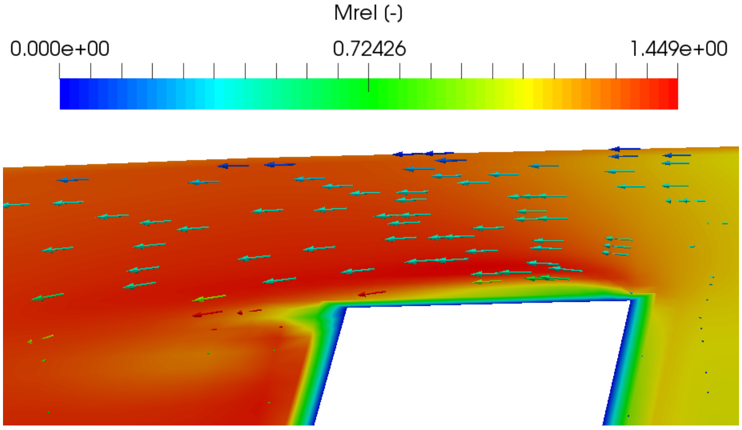

Figure 40: Details of relative Mach number field and relative velocity vectors at the axial cross-section 3 for the near peak efficiency operating point.

- **Axial cross-section 4** (presented on Figure (15))

The following Figures (41 - 44) present profiles of pressure, velocity, temperature, turbulent kinetic energy and turbulent viscosity field at the cross-section in the middle of the rotor blade passage, respectively. Pressure field presented at the Figure (41a) nicely captures the pressure distribution on both sides of the rotor blade, whereas the high pressure region is smoothly generated at the upper part of the pressure side of the rotor blade, while the low pressure region is located at the upper part of the rotor blade suction side.

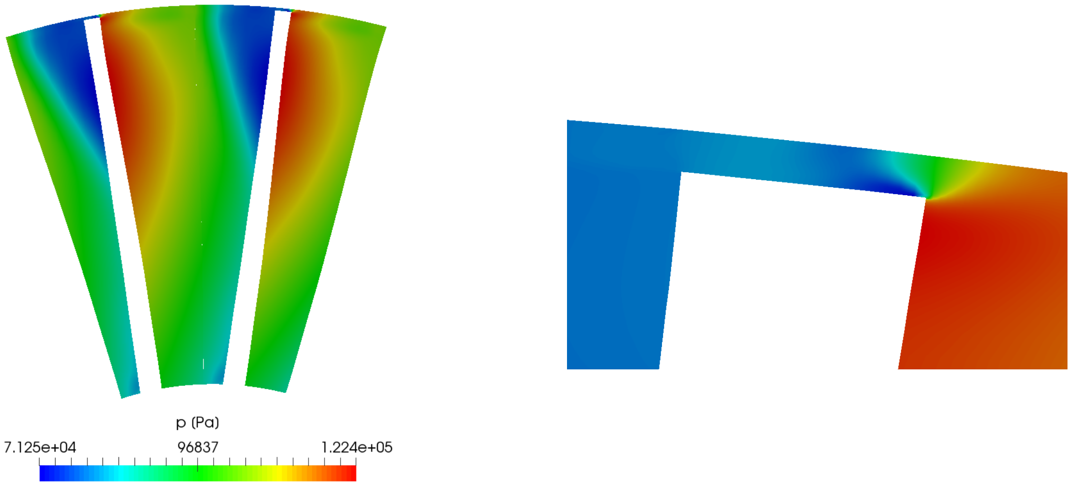

(a) Pressure field.

(b) Detail of the pressure field in the tip-gap.

Figure 41: Pressure field representation at the axial cross-section 4 for the near peak efficiency operating point.

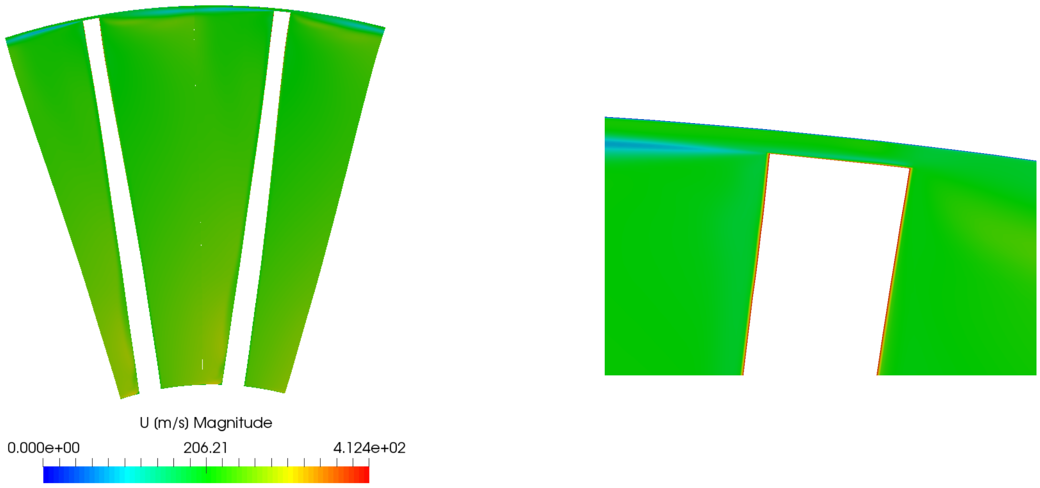

(a) Velocity field.

(b) Detail of the velocity field in the tip-gap.

Figure 42: Velocity field representation at the axial cross-section 4 for the near peak efficiency operating point.

Tip-gap pressure field detail is presented in the Figure (41b). It can be seen that high pressure gradients are located at the blade tip, which cause a tip-leakage flow. Within the blade passage, there is a smooth transition between a low pressure region at the suction side of a rotor blade and a high pressure region at the pressure side of the subsequent rotor blade in the annulus. Figure (43b) shows the temperature field at the axial cross-section at the middle of a blade passage. It can be observed that the high temperature region is located in the vicinity of a blade tip on the pressure side of a rotor blade. Figure (44a) shows the turbulent kinetic energy and turbulent viscosity field and they nicely highlight a tip-leakage flow. High values are present near the pressure side blade-tip, which are a source of localised high temperature field shown in Figure (43).

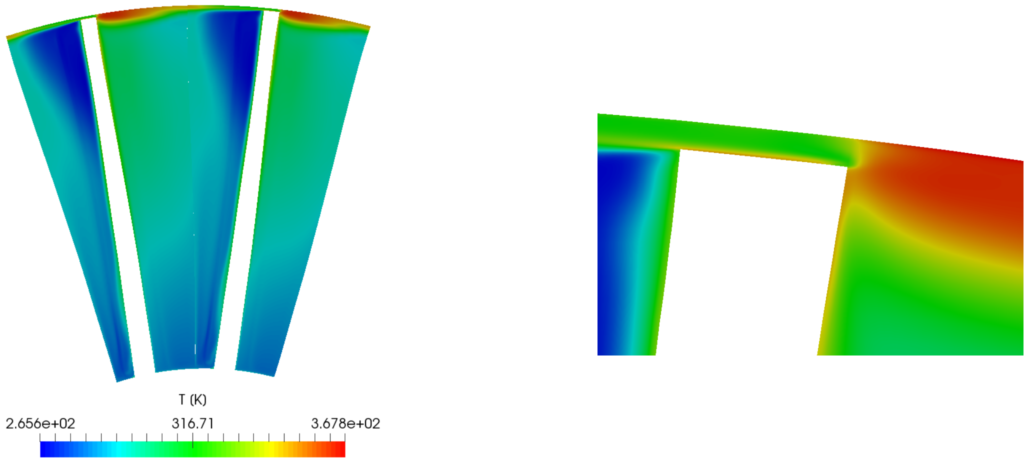

(a) Temperature field.

(b) Detail of the temperature field in the tip-gap.

Figure 43: Temperature field representation at the axial cross-section 4 for the near peak efficiency operating point.

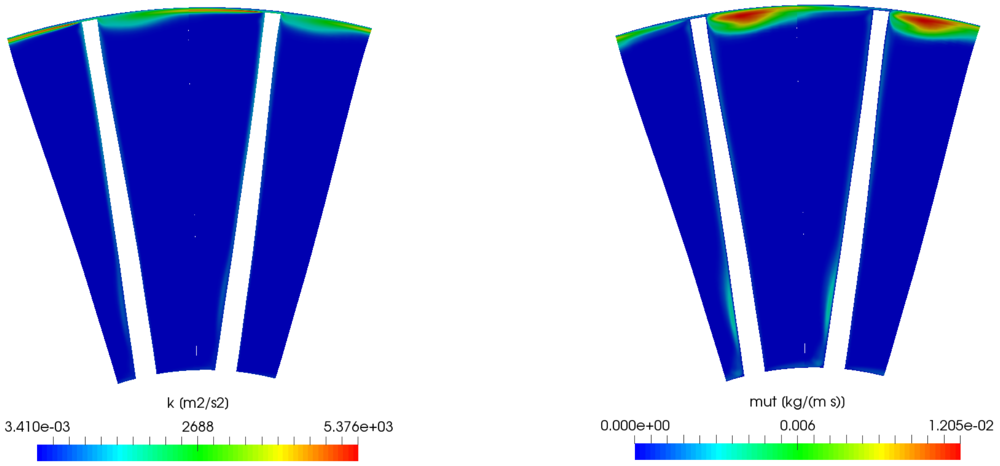

(a) Turbulent kinetic energy.

(b) Turbulent viscosity.

Figure 44: Turbulent kinetic energy and turbulent viscosity field representation at the axial cross-section 4 for the near peak efficiency operating point.

Figures (45) and (46) show the details of Mach number and relative Mach number field in the tip-gap of the axial cross-section 3 for the near peak efficiency operating point. Figure (46) additionally presents the relative velocity vectors in the tip-gap in order to visualise a tip-leakage flow from pressure to the suction side of a rotor blade.

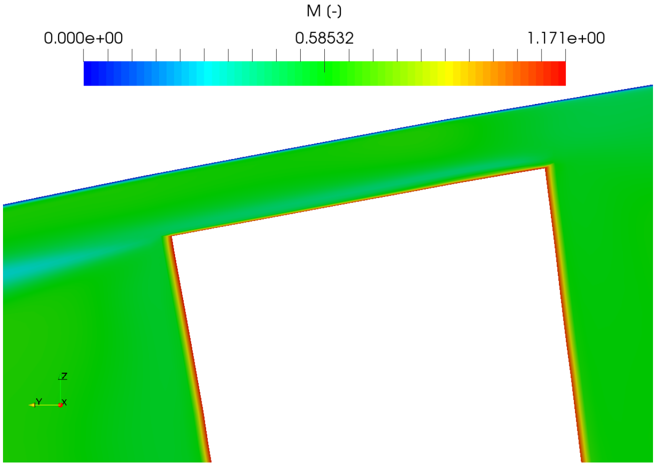

Figure 45: Details of Mach number field at the axial cross-section 4 for the near peak efficiency operating point.

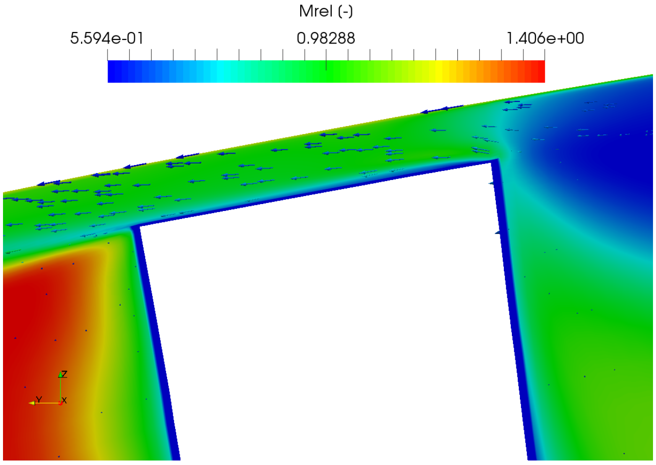

Figure 46: Details of relative Mach number field and relative velocity vectors at the axial cross-section 4 for the near peak efficiency operating point.

- **Axial cross-section 5** (presented on Figure (15))

The following Figures (47 - 50) present profiles of pressure, velocity, temperature, turbulent kinetic energy and turbulent viscosity field at the cross-section 5, respectively. Pressure field presented in Figure (47a) captures the pressure distribution on both sides of the rotor blade, whereas high pressure region is smoothly generated at the upper part of the rotor blade pressure side, while the low pressure region is located at the upper part of the rotor blade suction side.

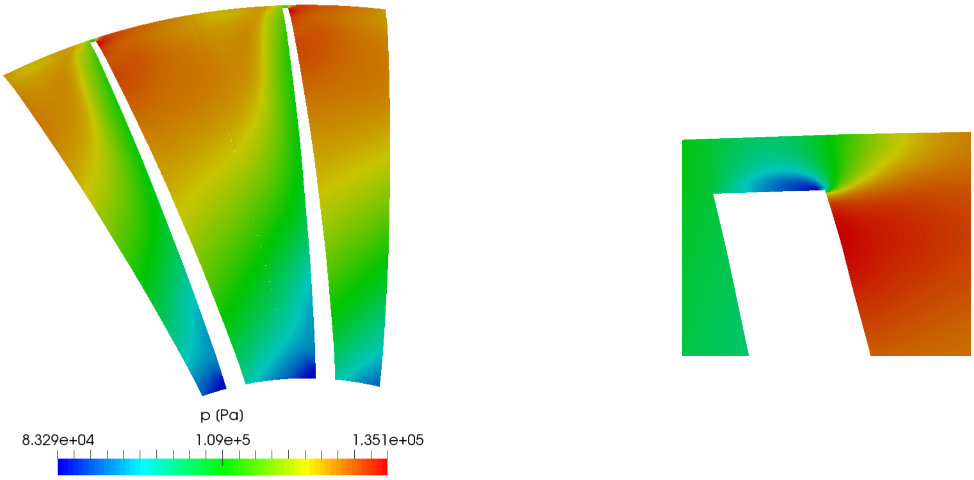

(a) Pressure field.

(b) Detail of the pressure field in the tip-gap.

Figure 47: Pressure field representation at the axial cross-section 5 for the near peak efficiency operating point.

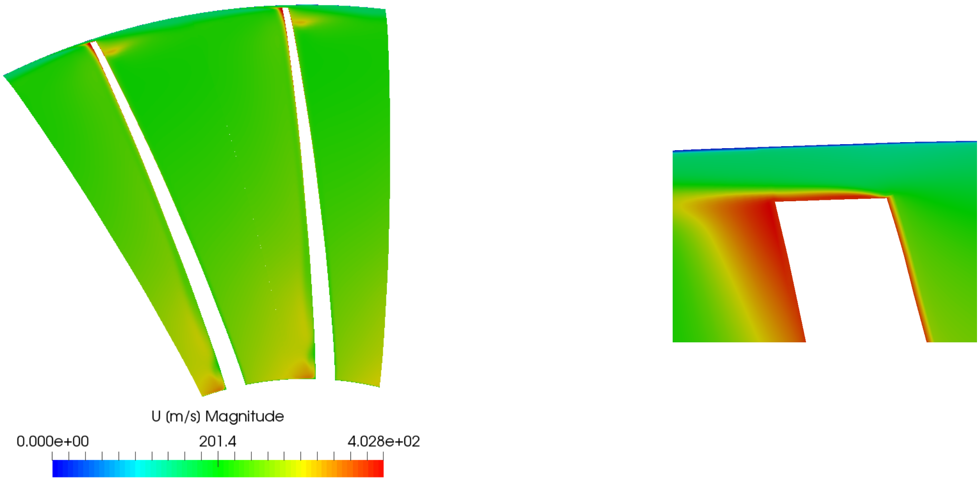

(a) Velocity field.

(b) Detail of the velocity field in the tip-gap.

Figure 48: Velocity field representation at the axial cross-section 5 for the near peak efficiency operating point.

Tip-gap pressure field detail is captured and presented in the Figure (47b). It can be seen that high pressure gradients are located at the blade tip, which cause a tip-leakage flow. Within the blade passage, there is a relatively smooth transition between a low pressure region at the suction side of a rotor blade and a high pressure region at the pressure side of the following rotor blade in the annulus. Figure (49b) shows the temperature field at the axial cross-section 5. It can be observed that the localised region of high temperature is located near the blade tip on the pressure side. Figure (50a) presents turbulent kinetic energy and turbulent viscosity field and they nicely show a tip-leakage flow. High values are present near the pressure side blade-tip, which are a source of localised high temperature field shown in Figure (49).

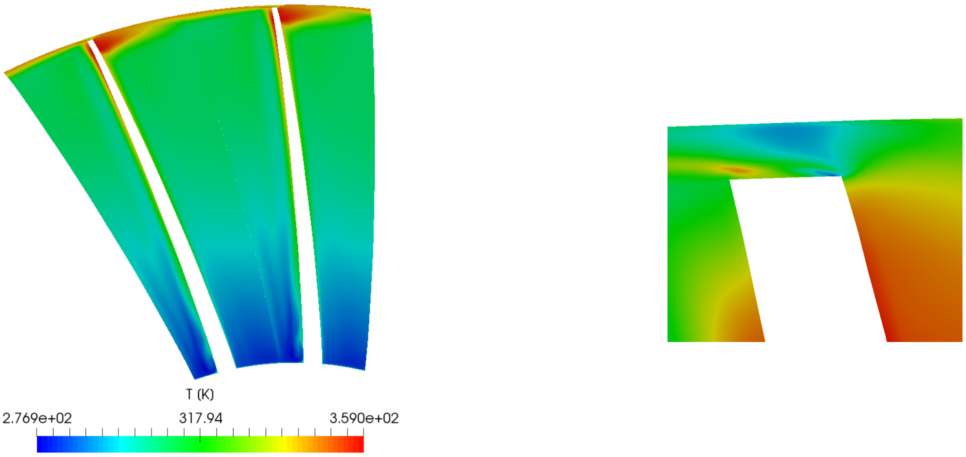

(a) Temperature field. **(b)** Detail of the temperature field in the tip-gap.

Figure 49: Temperature field representation at the axial cross-section 5 for the near peak efficiency operating point.

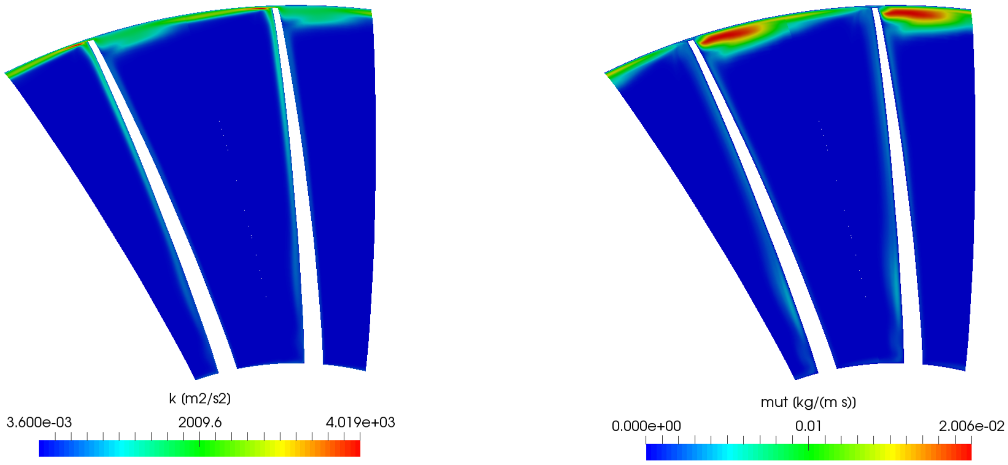

(a) Turbulent kinetic energy. **(b)** Turbulent viscosity.

Figure 50: Turbulent kinetic energy and turbulent viscosity field representation at the axial cross-section 5 for the near peak efficiency operating point.

Figures (51) and (40) show the details of Mach number and relative Mach number field in the tip-gap of the axial cross-section 3 for the near peak efficiency operating point. Figure (52) additionally presents the relative velocity vectors in the tip-gap in order to visualise a tip-leakage flow from pressure to the suction side of a rotor blade.

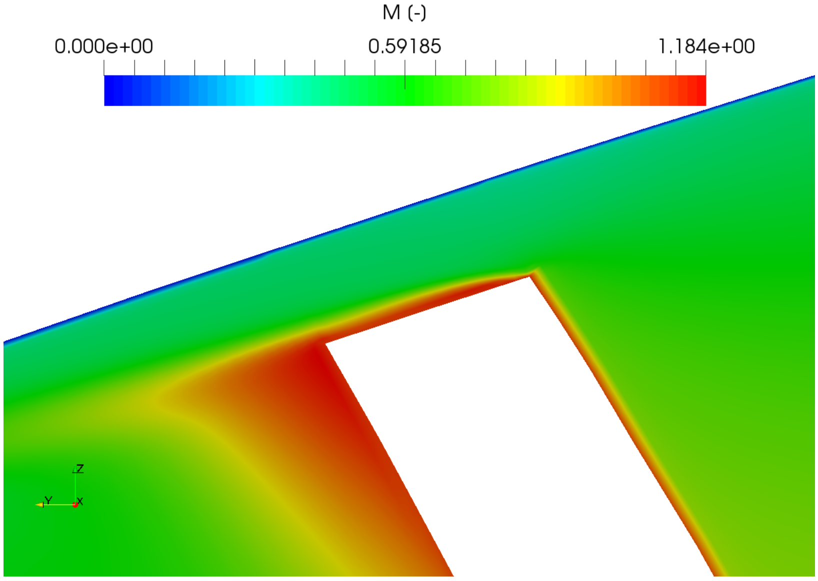

Figure 51: Details of Mach number field at the axial cross-section 5 for the near peak efficiency operating point.

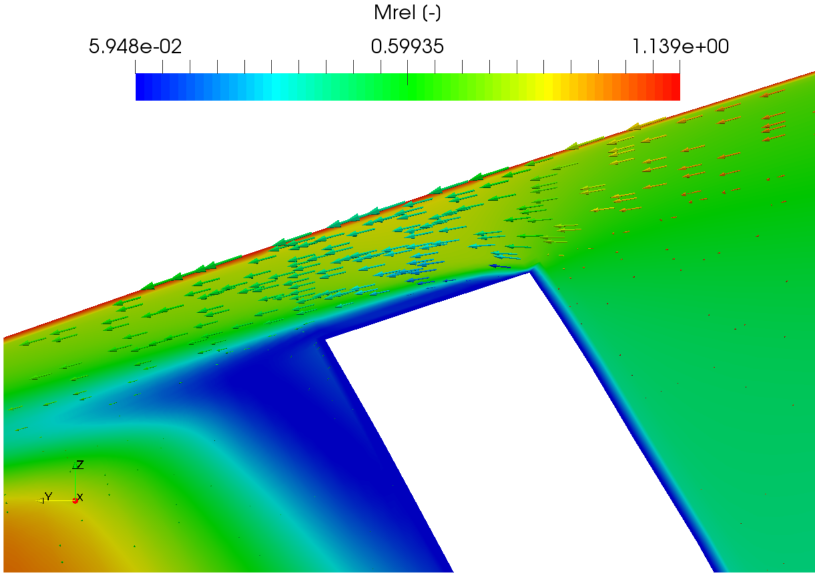

Figure 52: Details of relative Mach number field and relative velocity vectors at the axial cross-section 5 for the near peak efficiency operating point.

Pressure distribution at the each side of a rotor blade is presented in Figure (53), where a pressure side is presented in Figure (53a), while a suction side is shown in Figure (53b).

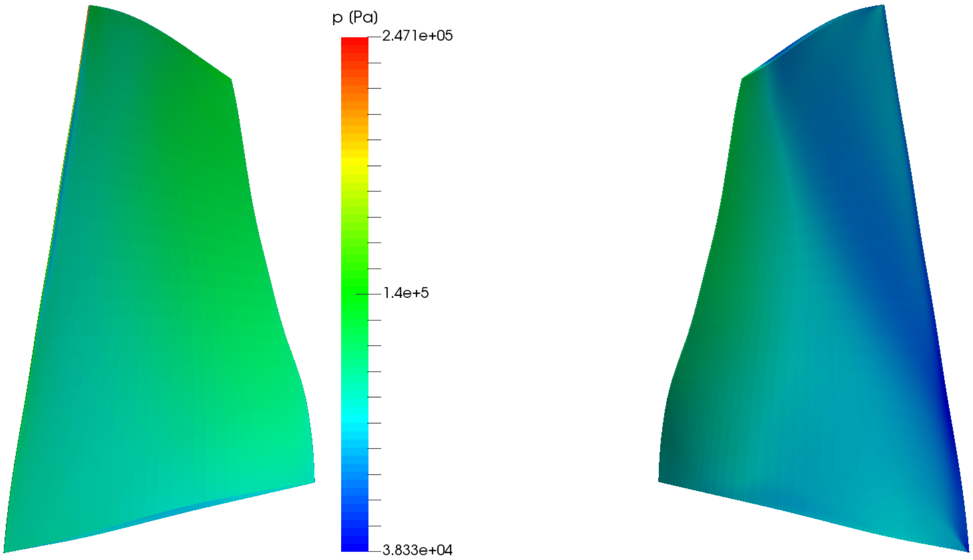

(a) Pressure side. **(b)** Suction side.

Figure 53: Pressure distribution at the rotor blade for the near peak efficiency operating point.

It is previously stated that the NASA Rotor 67 geometry produces vortices. The first type is a tip-gap vortex, while the other one appears at the trailing edge of a rotor blade. Since vortex shedding is a highly transient phenomenon and within this thesis a steady state approach is used, the subsequent vortex visualisations are only an approximation of a instantaneous flow pattern. Nevertheless, a tip-leakage flow along with the tip-gap vortex shedding and trailing edge vortex are captured and presented.

Within this thesis vortices are visualised using two methods: visualisation by streamlines and by Q-contours. Q-contour expression reads,

$$Q = \frac{1}{2}\left(|\mathbf{A}| - |\mathbf{S}|\right), \tag{65}$$

where $\mathbf{A}$ is the antisymmetric part of a velocity gradient tensor, which describes a rotation of a fluid particle. On the other hand, $\mathbf{S}$ is the symmetric part of a velocity gradient tensor, which describes a deformation of a fluid particle. Thus, Q is a scalar quantity that represents the difference between magnitudes of antisymmetric and symmetric part of a velocity gradient tensor. The criterion for vortex visualisation via Q-contour is that the antisymmetric part has to be greater than the symmetric part of a velocity gradient tensor.

Figure (54) shows a tip-leakage flow along with the tip-gap vortex shedding visualised by streamlines, while the Figure (57) presents a captured trailing edge vortex visualised via Q-contour method. A tip-gap vortex is also visualised via Q-contour, which is presented in the Figure (55).

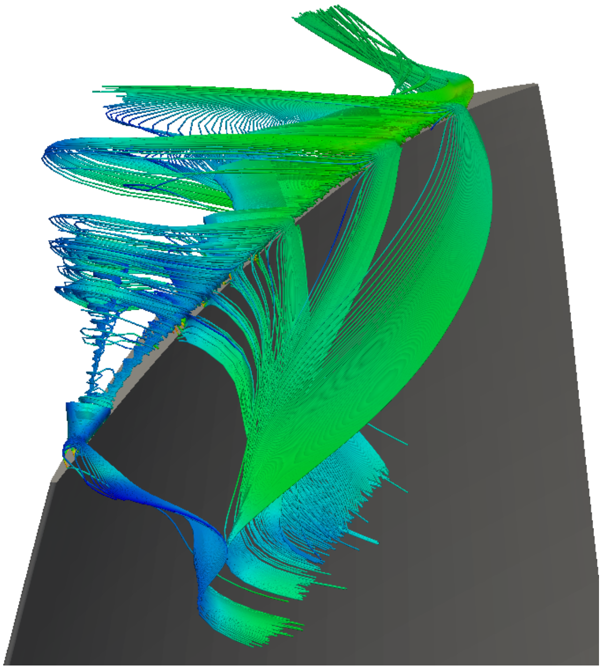

Figure 54: Tip-leakage flow and tip-gap vortex shedding visualised by streamlines at the near peak efficiency operating point.

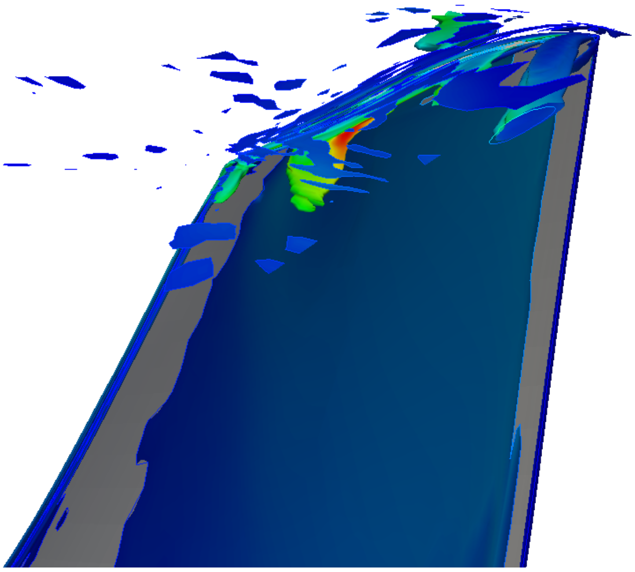

Figure 55: Tip-gap vortex visualisation via Q-contour for the near peak efficiency operating point.

Figure (56) shows the root vortex at the rotor blade trailing edge for the near peak efficiency operating point visualised by streamlines.

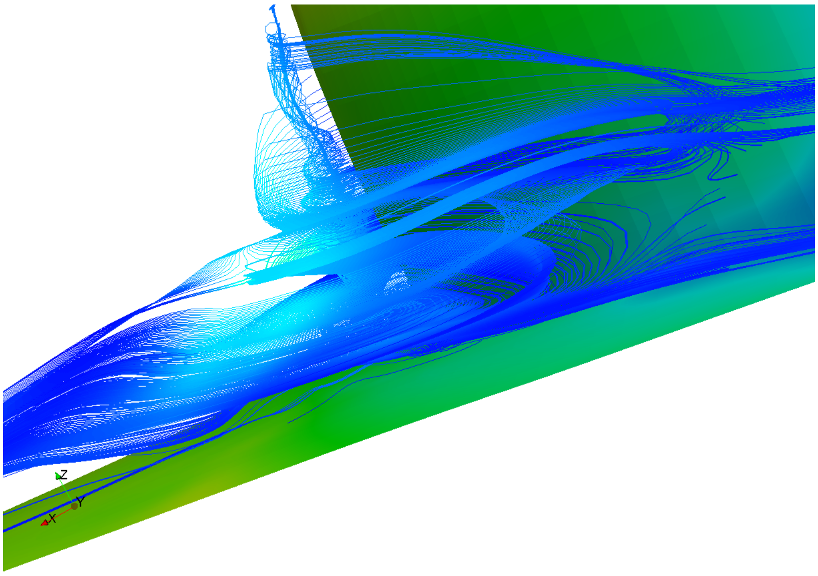

Figure 56: Vortex shedding at the trailing edge of a rotor blade visualised by streamlines for the near peak efficiency operating point.

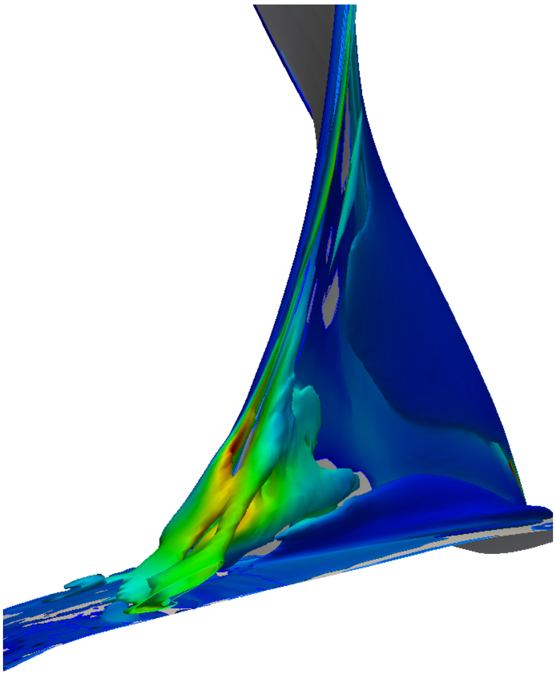

Figure 57: Vortex shedding at the trailing edge of a rotor blade visualised via Q-contour method at the near peak efficiency operating point.

Finally, after presenting all significant fluid flow distributions at various cross-sections of the numerical domain for the near-peak efficiency operating point, overall performance of the NASA Rotor 67 turbofan is to be presented. Achieved mass flow rate $\dot{m}$ equals 33,65 kg/s, while the obtained total pressure ratio Π is 1,6148. Obtained overall adiabatic efficiency η_{ad} of the NASA Rotor 67 turbofan is 90,03%. Detailed results are summarized in tabular form and presented in Table (8).

Table 8: Overall performance of the NASA Rotor 67 turbofan at the near peak efficiency operating point.

Parameter	**Value**	**Experiment**	**Error**	**Relative Error, [%]**
Mass flow rate, $\dot{m}$	33,65 kg/s	34,573 kg/s	0,923 kg/s	2,67
Total pressure ratio, Π	1,6148	1,642	0,0272	1,66
Fan torque, T_F	42,9 N m	/	/	/
Axial force, F	-172,4 N	/	/	/
Power, P	72 020 W	/	/	/
Adiabatic efficiency, η_ad	90,03%	93%	2,97%	3,19

In addition to the overall performance data obtained within the numerical simulation, the values obtained in the experiment were also presented in the Table (8). According to the the relative error between the numerical simulation and experiment, results slightly differ. The reason for that can also be due to measurement uncertainty. Nevertheless, obtained numerical results presented within this subsection highly agree with the provided experimental data according to the acceptable numerical error for CFD numerical simulations.

5.3.1 Closure

Numerical results for the fluid flow inside the NASA Rotor 67 axial flow turbofan at the near-peak efficiency operating point were presented within this subsection. Fluid flow quantities were presented at radial cross-sections at 10%, 30% and 70% span of the annulus. Results were presented in terms of pressure, temperature, velocity and turbulence properties while the relative Mach number contours were used for comparison with data provided in the experiment [1]. Detailed distribution of fluid flow quantities were presented at axial cross-sections upstream and downstream of the rotor blade where the influence of rotor blade can be observed. Additionally, axial cross-section in the middle of a blade passage was also considered and results were accordingly presented.

Since the NASA Rotor 67 turbofan geometry has introduced vortical structures at the tip-gap and at the rotor blade trailing edge, those vortices were visualised by streamlines and via Q-contour representation. Finally, the obtained overall aerodynamic performance of the NASA Rotor 67 axial-flow turbofan was presented in tabular form.

To sum up, relative Mach number contours obtained in the numerical simulation appear to be in agreement with experiment just like the overall aerodynamic performance of the considered turbofan. Thus, a new compressible flow solver within the `foam-extend` CFD package has generated satisfying results.

5.4 Near Stall Operating Point

This subsection presents the near-stall operating point results obtained by the numerical simulation. Flow field representations are given for physical quantities of interest at various radial and axial cross-sections of the numerical domain according to the cross-sections analysed within Subsection (5.3). Thus, the comparison of results between nominal, near-peak efficiency and near-stall operating point is facilitated. Since the NASA Rotor 67 turbofan is still in the stable operating range, presented results do not significantly differ from results for the near-peak efficiency operating point presented within the Subsection (5.3).

- **Cross-section at 10% span from shroud**

Subsequent figures represent flow field quantities at the cross section located at 10% span from shroud. Figure (58) shows the comparison of relative Mach number contour plots from the experiment and numerical simulation. There is a relatively good agreement between presented values on Figure (58a) and Figure (58b).

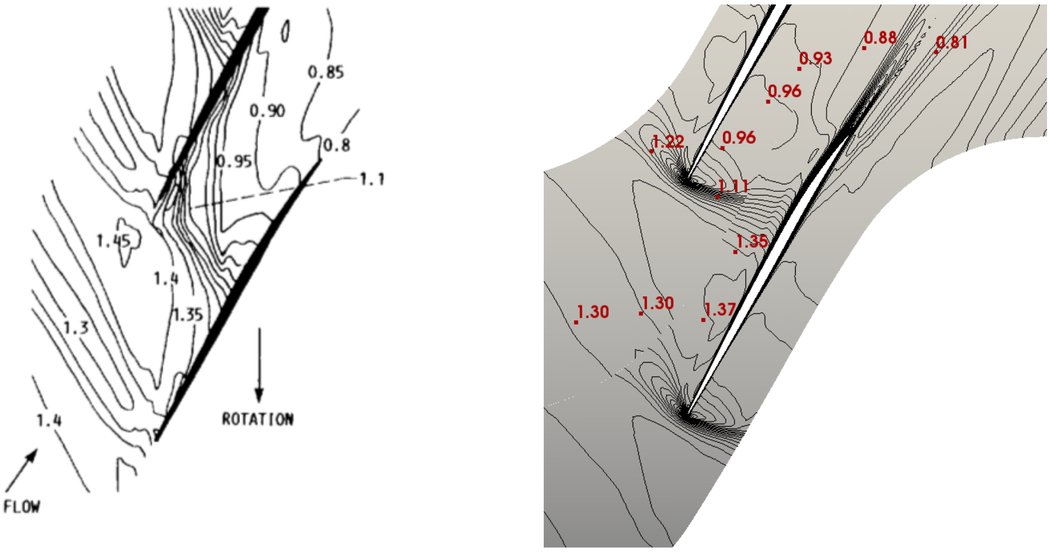

(a) Experiment [1]. **(b)** Numerical simulation.

Figure 58: Comparison of relative Mach number contour plots from experiment and numerical simulation at 10% span from shroud for the near-stall operating point.

Figure (59) presents the pressure and temperature field at the 10% span from shroud obtained for the near-stall operating point. Static pressure at the pressure side of the rotor blade gradually increases in the streamwise direction, which ensures proper working conditions for a turbofan. Figure (59b) shows the corresponding temperature field in the blade passage, which follows the pressure field contours according to the equation of state for the ideal gas. Thus, lower temperature values occur on the suction side of the rotor blade, while the higher temperature values occur on the pressure side of the rotor blade.

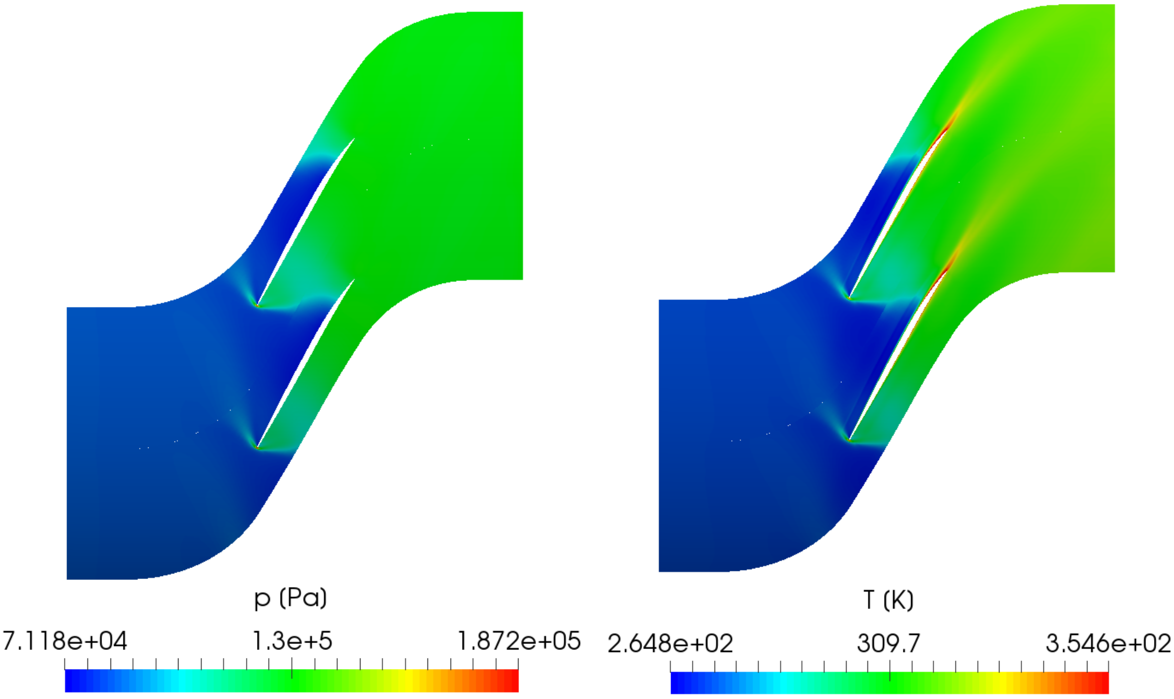

(a) Pressure field. **(b)** Temperature field.

Figure 59: Pressure and temperature field representation at the 10% span from shroud for the near-stall operating point.

Figure (60) presents the absolute velocity and relative Mach number field at the 10% span from shroud obtained for the near-stall operating point. Relative Mach number field at the considered cross-section implies that the NASA Rotor 67 turbofan's inflow appears to have supersonic flow conditions in terms of relative velocity. Flow through blade passages is transonic, while the outflow is subsonic. Relative Mach number field, indirectly representing the relative velocity, is in accordance with the pressure field presented in Figure (59a) due to Bernoulli principle. It can be observed that the relative Mach number is sensibly lower in the turbulent wake downstream of the rotor blade row, if it is compared to the relative Mach number in its surroundings.

Figure (61) presents turbulent kinetic energy and turbulent viscosity field representation at the 10% span from shroud obtained for the near-stall operating point. It can be seen that the fluid flow is highly turbulent downstream of rotor blades. Turbulent wake spreading downstream of the rotor blade row is clearly presented.

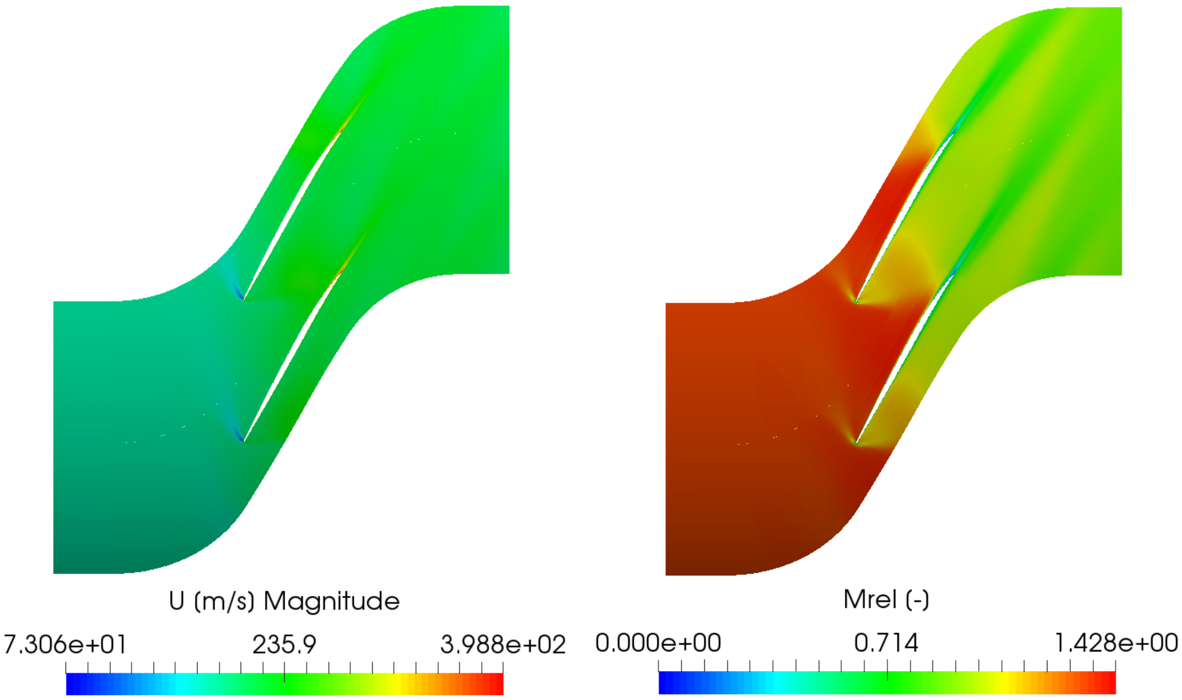

(a) Velocity field.

(b) Relative Mach number field.

Figure 60: Velocity and relative Mach number field representation at the 10% span from shroud for the near-stall operating point.

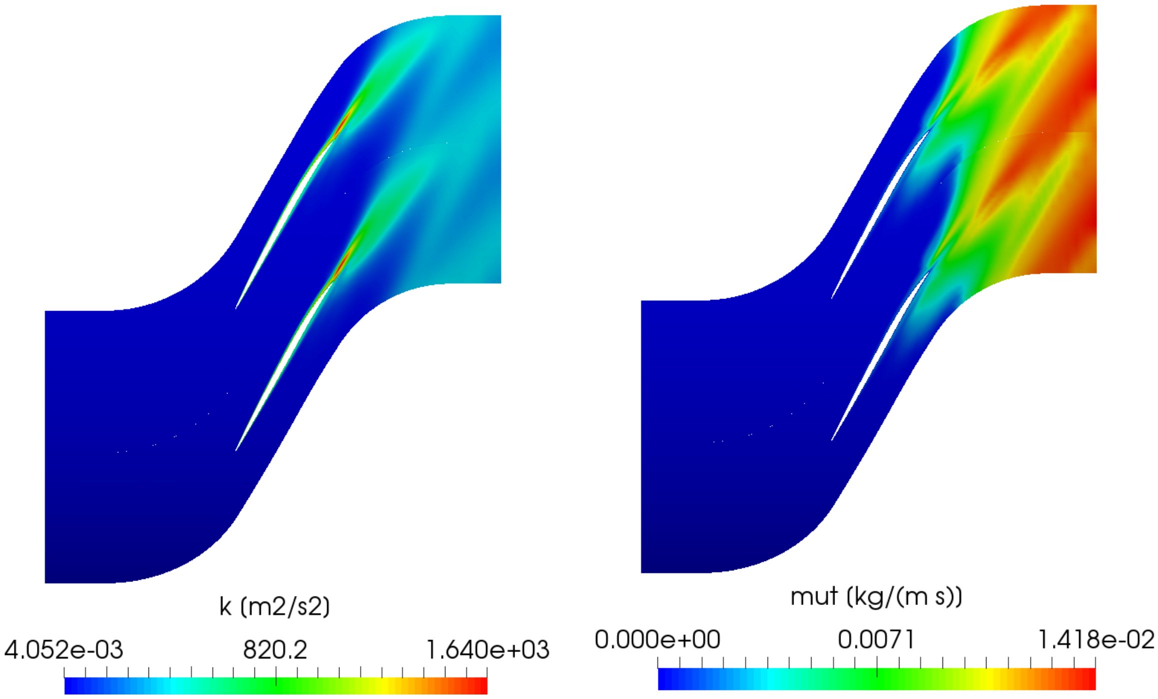

(a) Turbulent kinetic energy field.

(b) Turbulent viscosity field.

Figure 61: Turbulent kinetic energy and turbulent viscosity field representation at the 10% span from shroud for the near-stall operating point.

In Figure (62) a relative Mach number was presented as a function of pitch percentage, while the considered cross-section is the 50% of axial chord at the 10% span from shroud. As can be seen, there is a relatively good agreement between numerical simulation and experiment.

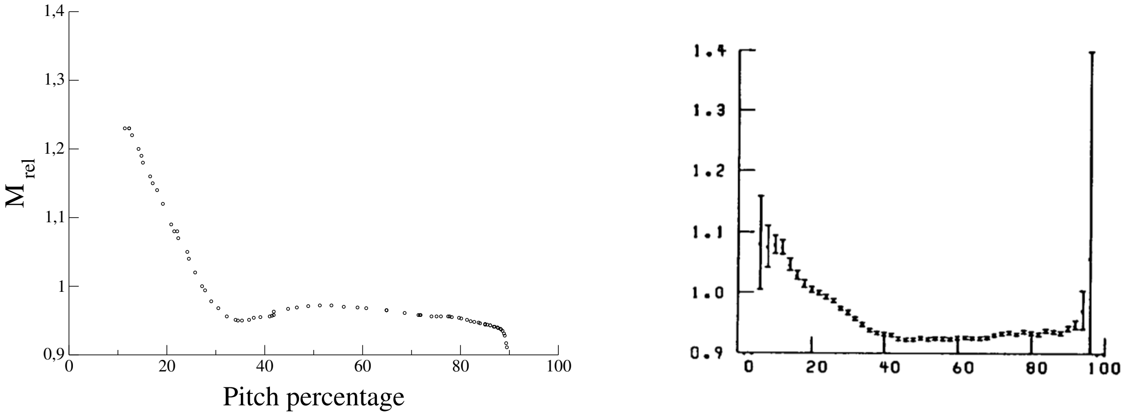

(a) Numerical simulation. **(b)** Experiment [1].

Figure 62: Blade-to-blade comparison of relative Mach number plots between numerical simulation and experiment for 50% axial chord at the 10% span cross-section for the near-stall operating point.

- **Cross-section at 30% span from shroud**

The following figures present the flow field quantities at the cross-section located at 30% span from the shroud. Figure (63) shows the comparison between relative Mach number contours from the experiment and those obtained in the numerical simulation. There is again a good agreement between presented values on Figures representing the experiment (63a) and those representing numerical simulation (63b).

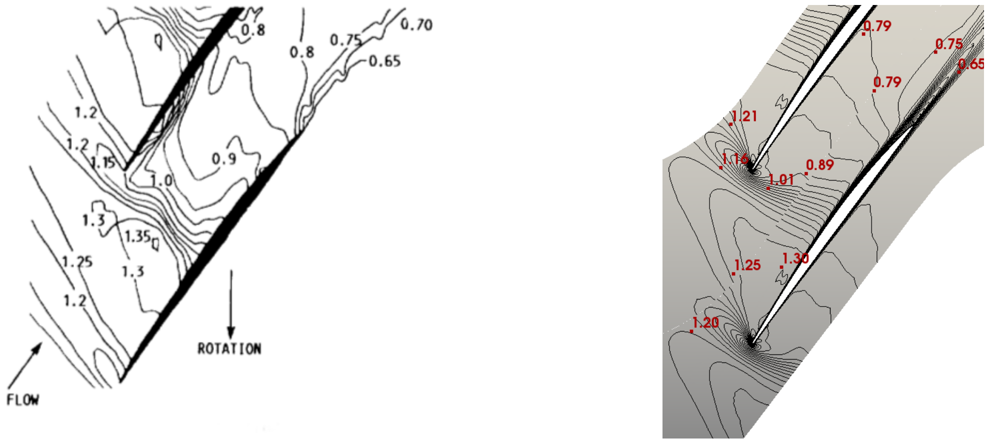

(a) Experiment [1]. **(b)** Numerical simulation.

Figure 63: Comparison of relative Mach number contour plots of experiment and numerical simulation at 30% span from shroud for the near-stall operating point for the near-stall operating point.

Figure (64) shows the pressure and temperature field. Figure (65) presents the absolute velocity and relative Mach number field. Relative Mach number field at the considered cross-section shows that the NASA Rotor 67 turbofan's inflow appears to have supersonic flow conditions in terms of relative velocity. Additionally, the flow through blade passages is transonic, while the outflow is subsonic.

Figure (66) presents turbulent kinetic energy and turbulent viscosity field representation at the 30% span from shroud obtained for the near-stall operating point. It can be seen that the fluid flow is highly turbulent downstream of rotor blades. Turbulent wake spreading downstream of rotor blade row is again clearly presented.

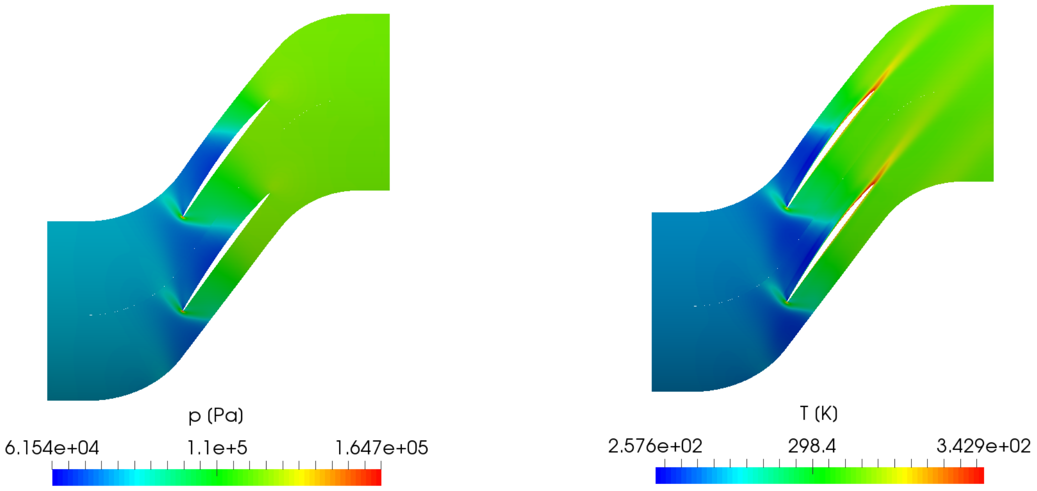

(a) Pressure field. **(b)** Temperature field.

Figure 64: Pressure and temperature field representation at the 30% span from shroud for the near-stall operating point.

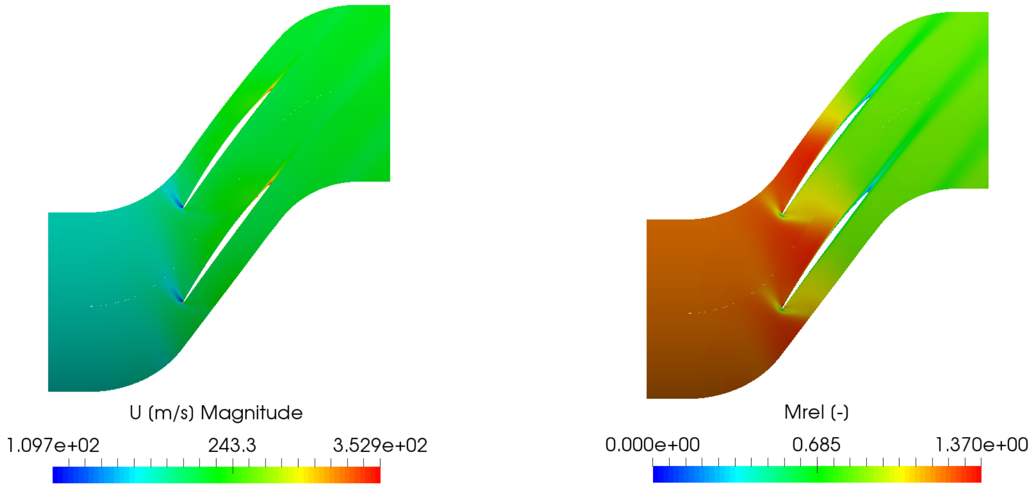

(a) Velocity field. **(b)** Relative Mach number field.

Figure 65: Velocity and relative Mach number field representation at the 30% span from shroud for the near-stall operating point.

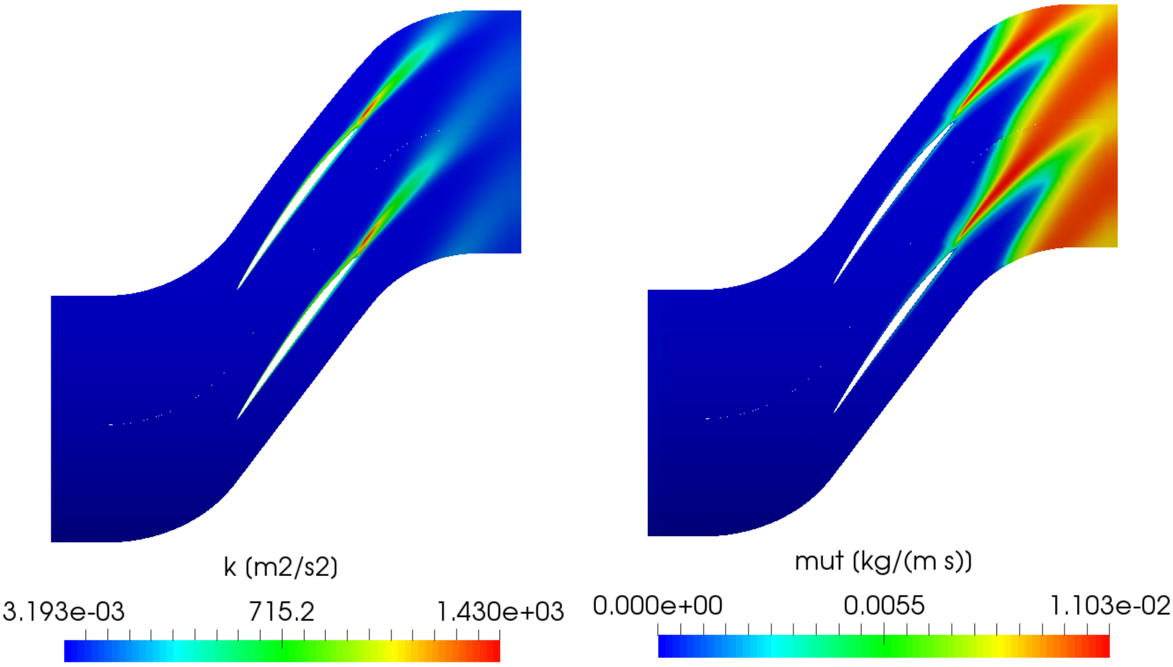

(a) Turbulent kinetic energy field.

(b) Turbulent viscosity field.

Figure 66: Turbulent kinetic energy and turbulent viscosity field representation at the 30% span from shroud for the near-stall operating point.

Figure (67) shows a relative Mach number as a function of pitch percentage at the 50% of axial chord cross-section at the 30% span from shroud. As can be seen, agreement between numerical simulation results and experiment is very high.

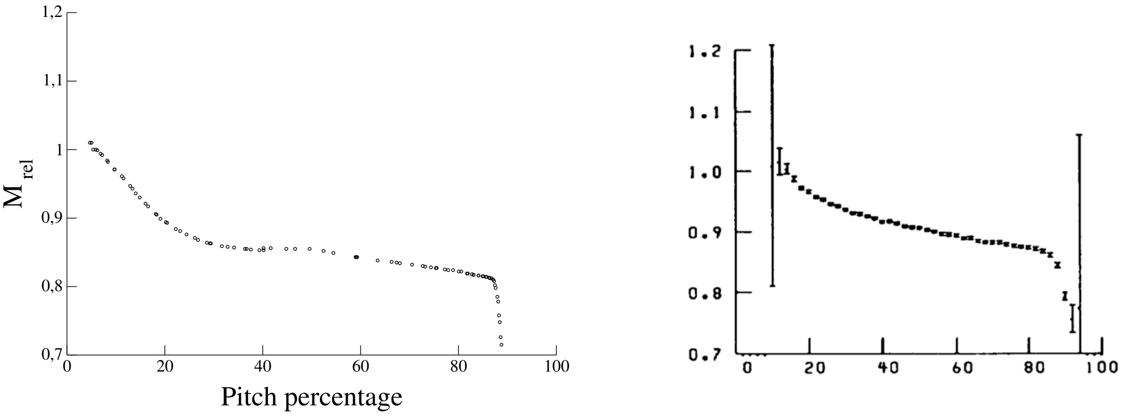

(a) Numerical simulation.

(b) Experiment [1].

Figure 67: Blade-to-blade comparison of relative Mach number plots between numerical simulation and experiment for 50% axial chord at the 30% span cross-section for the near-stall operating point.

- **Cross-section at 70% span from shroud**

The subsequent figures represent the flow field quantities at the cross-section located at 70% span from shroud for the near-stall operating point. The comparison between the relative Mach number contours in the experiment and those obtained in the numerical simulation is shown in Figure (68). Good agreement can be noticed in relative Mach number values on Figures (68a) representing the experiment and numerical simulation (68b).

Furthermore, pressure and temperature fields are shown in Figure (69). In contrast to the temperature fields at preceding cross-sections, a relatively high temperature of the fluid in the turbulent wake spreading downstream of the rotor blade can be observed. Figure (70) shows the absolute velocity and relative Mach number field. Relative Mach number field at the 70% span cross-section shows that the NASA Rotor 67 turbofan's inflow has supersonic flow conditions. Furthermore, the flow through blade passages is transonic, while the outflow is subsonic.

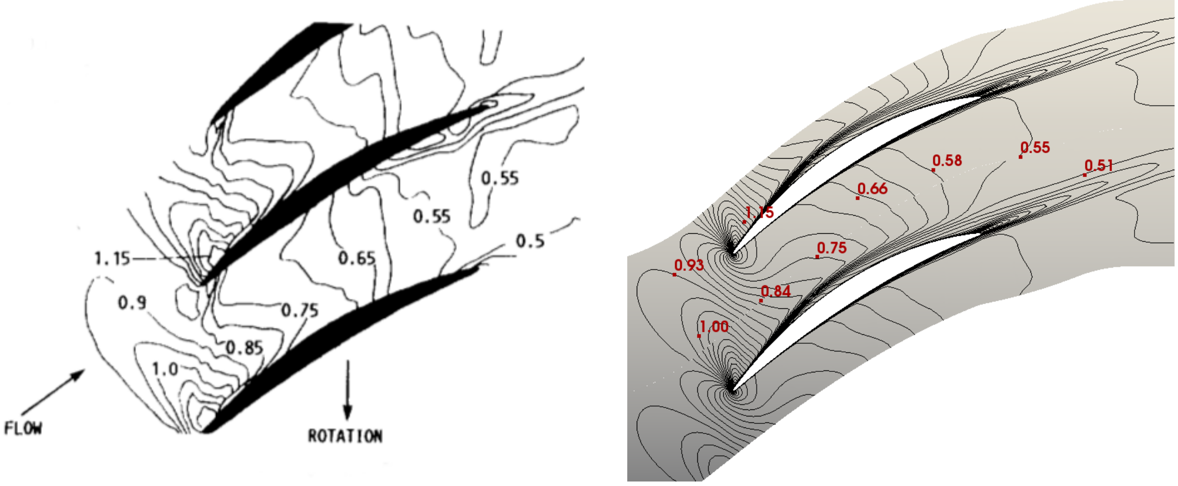

(a) Experiment [1]. **(b)** Numerical simulation.

Figure 68: Comparison of relative Mach number contour plots of experiment and numerical simulation at 70% span from shroud for the near-stall operating point.

Figure (71) shows turbulent kinetic energy and turbulent viscosity field at the 70% span from shroud obtained for the near-stall operating point. It can be seen that the fluid flow is highly turbulent downstream of rotor blades. Turbulent wake spreading downstream of the rotor blade row is clearly seen and the presence of fluid flow separation on the suction side can be observed.

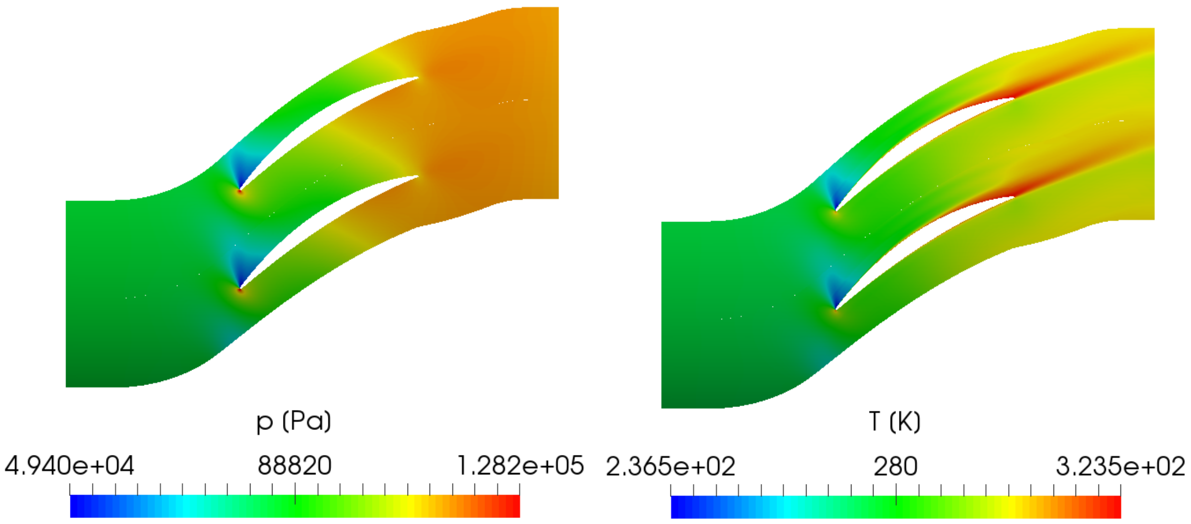

(a) Pressure field. **(b)** Temperature field.

Figure 69: Pressure and temperature field representation at the 70% span from shroud for the near-stall operating point.

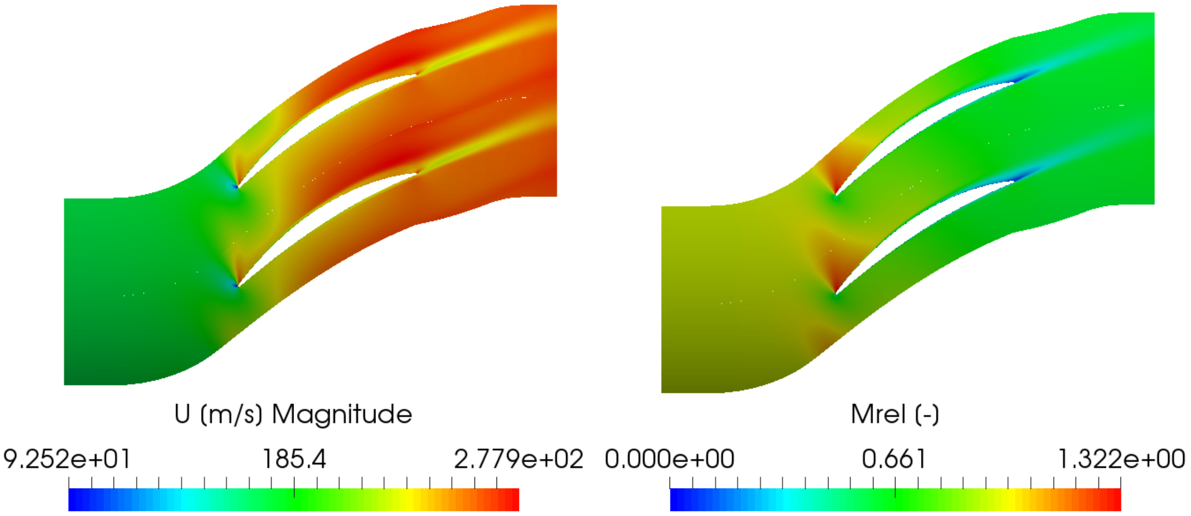

(a) Velocity field. **(b)** Relative Mach number field.

Figure 70: Velocity and relative Mach number field representation at the 70% span from shroud for the near-stall operating point.

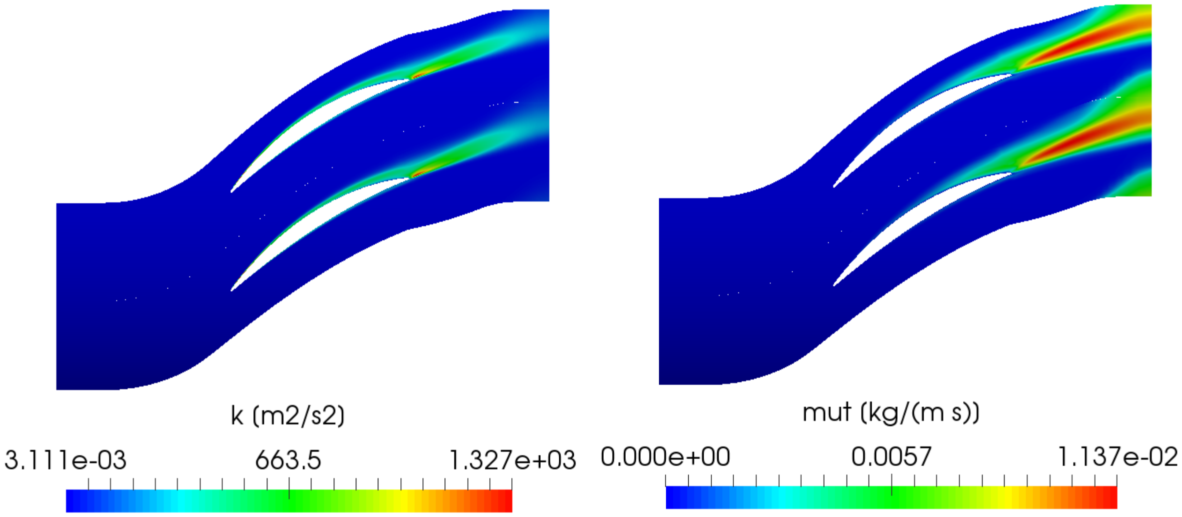

(a) Turbulent kinetic energy field.

(b) Turbulent viscosity field.

Figure 71: Turbulent kinetic energy and turbulent viscosity field representation at the 70% span from shroud for the near-stall operating point.

Figure (72) shows a relative Mach number as a function of pitch percentage at the 50% of axial chord cross-section at the 70% span from shroud. As can be seen, agreement between numerical simulation results and experiment is very high.

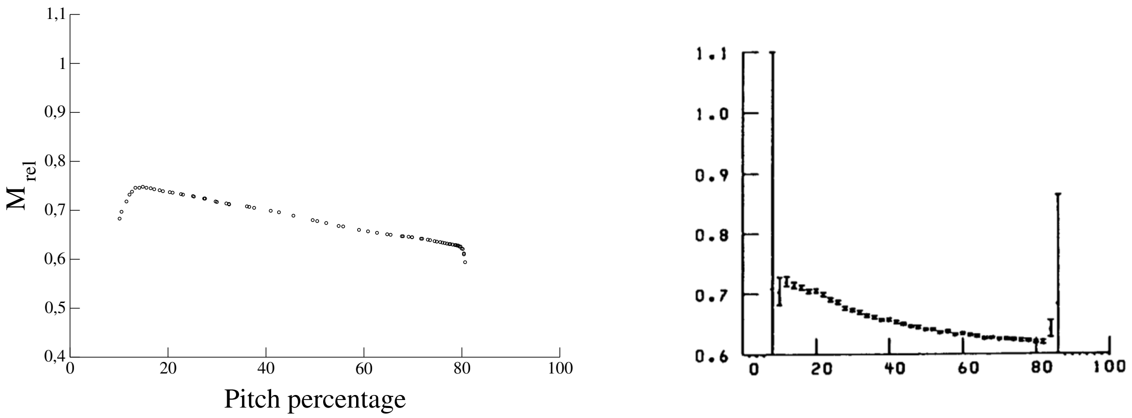

(a) Numerical simulation.

(b) Experiment [1].

Figure 72: Blade-to-blade comparison of relative Mach number plots between numerical simulation and experiment for 50% axial chord at the 70% span cross-section for the near-stall operating point.

- **Axial cross-section upstream of the rotor blade** (cross-section 1 on Figure (15))

The subsequent Figures (73) and (74) present distributions of pressure, temperature, velocity and relative Mach number at the cross-section upstream of the rotor blade. It can be observed that fluid flow quantities are almost undisturbed, except for the pressure and temperature fields presented in Figures (73a) and (74a) where the influence of the low pressure region at the suction side of the rotor blade is noted.

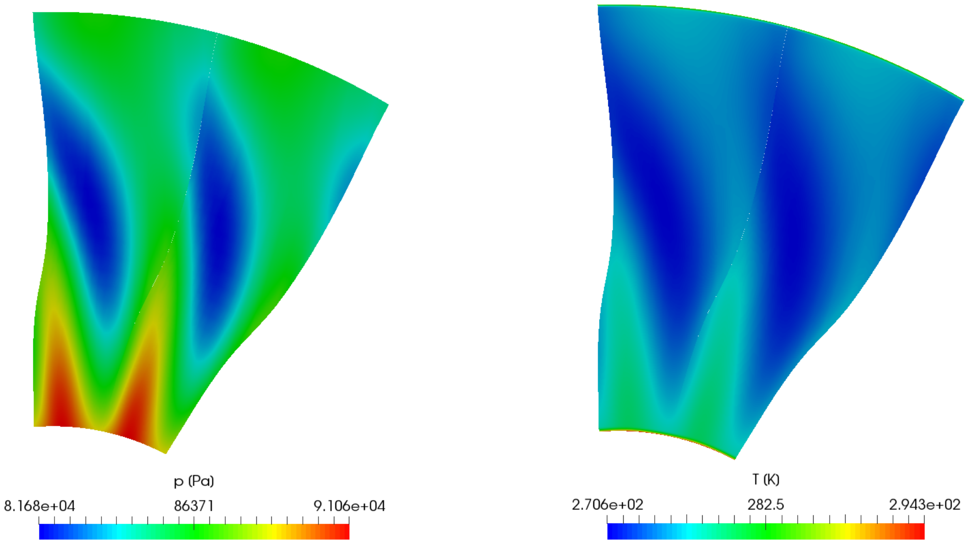

(a) Pressure field.

(b) Temperature field.

Figure 73: Pressure and temperature field representation at the axial cross-section upstream of the rotor blade leading edge for the near-stall operating point.

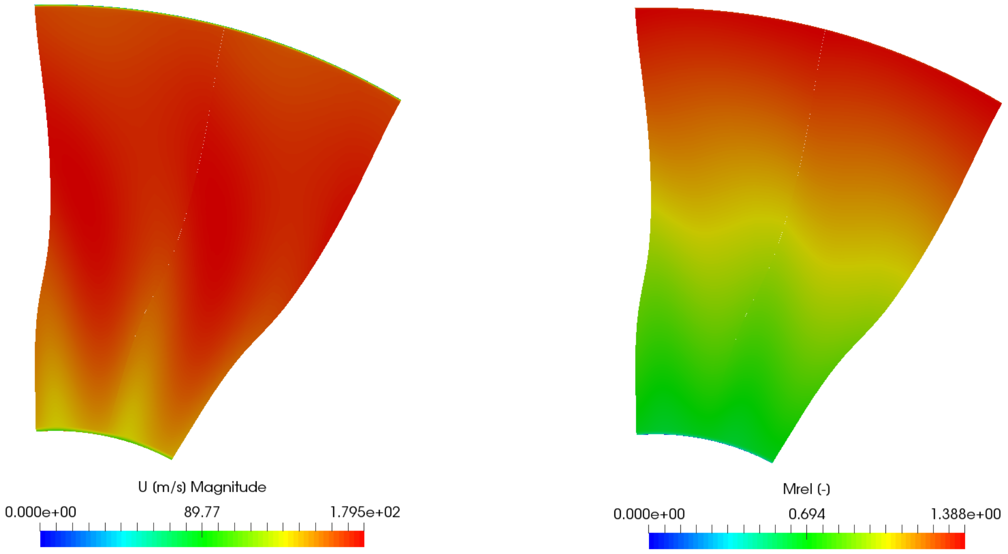

(a) Velocity field.

(b) Relative Mach number field.

Figure 74: Velocity and relative Mach number field representation at the axial cross-section upstream of the rotor blade for the near-stall operating point.

- **Axial cross-section downstream of the rotor blade** (cross-section 2 on Figure (15))

The subsequent Figures (75) and (76) present distributions of pressure, temperature, velocity and turbulent kinetic energy at the cross-section downstream of the rotor blade. It can be observed that fluid flow quantities are completely influenced by turbulent wake spreading downstream of the rotor blade trailing edge. The existence of a trailing edge vortex can be clearly seen in the Figure (76b).

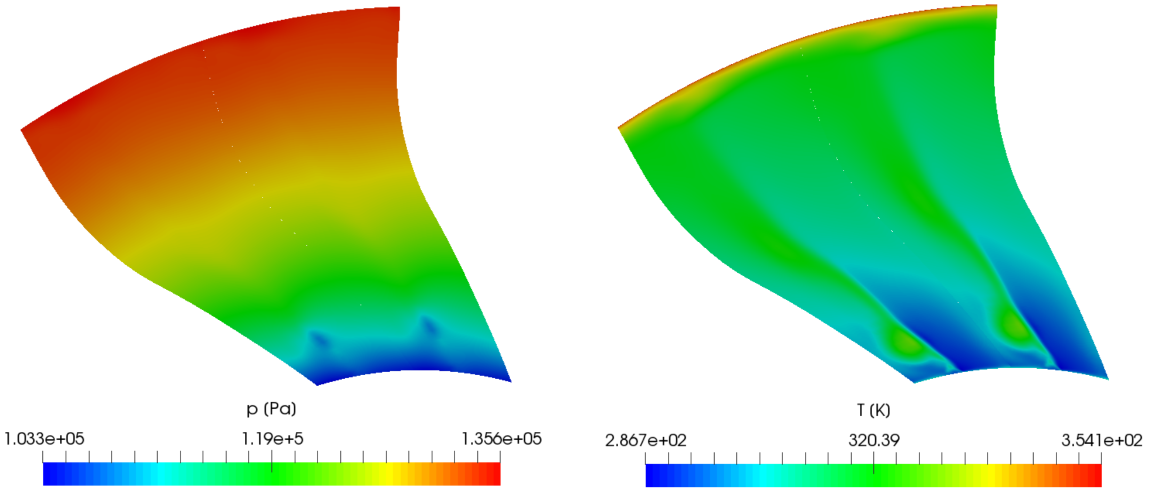

(a) Pressure field.

(b) Temperature field.

Figure 75: Pressure and temperature field representation at the axial cross-section downstream of the rotor blade for the near-stall operating point.

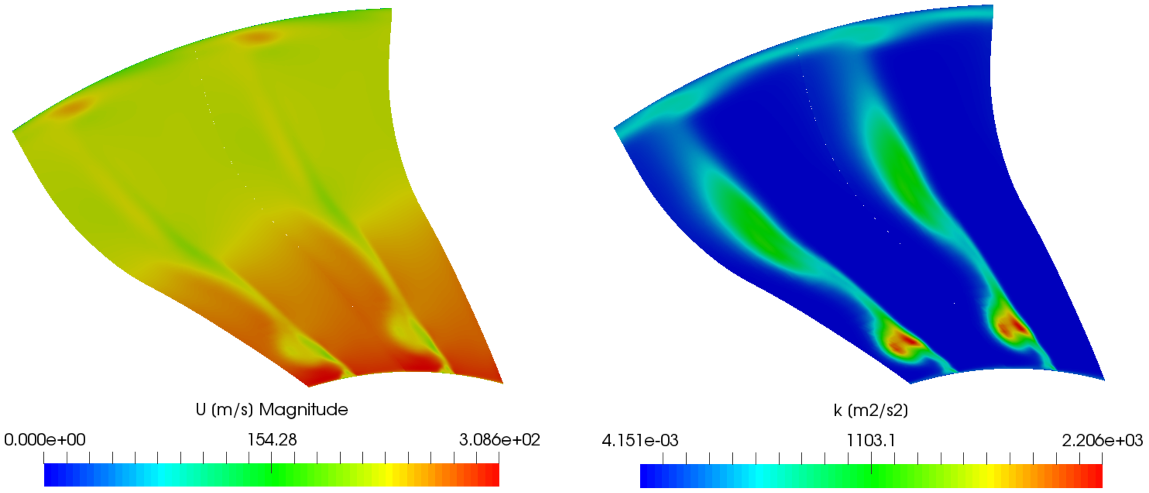

(a) Velocity field.

(b) Turbulent kinetic energy field.

Figure 76: Velocity and turbulent kinetic energy field representation at the axial cross-section downstream of the rotor blade for the near-stall operating point.

- **Axial cross-section 3** (presented on Figure (15))

The following Figures (77 - 80) present profiles of pressure, velocity, temperature, turbulent kinetic energy and turbulent viscosity field at the axial cross-section 3, respectively. The majority of presented fields are shown alongside with the fluid flow detail at the tip-gap. The pressure field in the Figure (77a) presents higher pressure values in the rotor blade passage when compared to pressure distribution on the same axial cross-section for the peak-efficiency operating point (Figure (35)). Higher pressure values are located only locally near the blade tip on the pressure side of a blade, which indicates the vicinity of the stagnation point for the fluid flow.

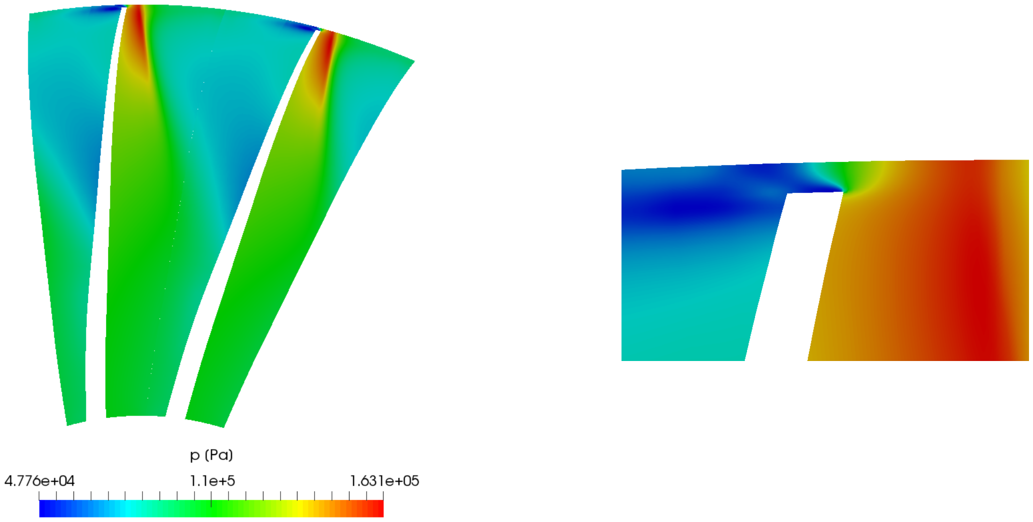

(a) Pressure field. **(b)** Detail of the pressure field in the tip-gap.

Figure 77: Pressure field representation at the axial cross-section 3 for the near-stall operating point.

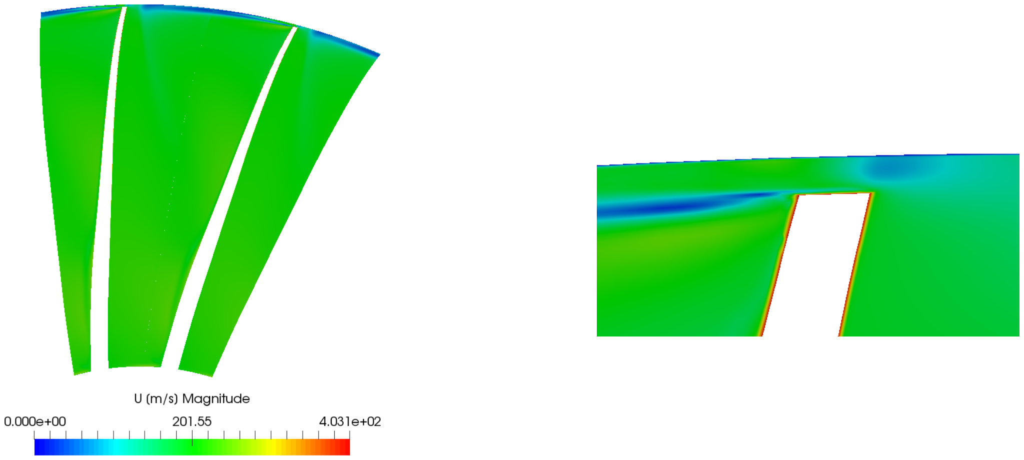

(a) Velocity field. **(b)** Detail of the velocity field in the tip-gap.

Figure 78: Velocity field representation at the axial cross-section 3 for the near-stall operating point.

Tip-gap pressure field detail is presented in the Figure (77b). It can be seen that high pressure gradients are located at the blade tip, which cause a tip-leakage flow. Within the blade passage, there is a sudden transition between a low pressure region at the suction side of a rotor blade and a high pressure region at the pressure side of the subsequent rotor blade in the annulus. Figure (79b) shows temperature field at the axial cross-section 3. It can be observed that the high temperature region is located in the vicinity of a blade tip on the pressure side of a rotor blade. Figure (80a) presents turbulent kinetic energy and turbulent viscosity field and it nicely shows a tip-leakage flow. High values are present near the pressure side blade-tip, which are a source of localised high temperature field shown in Figure (79).

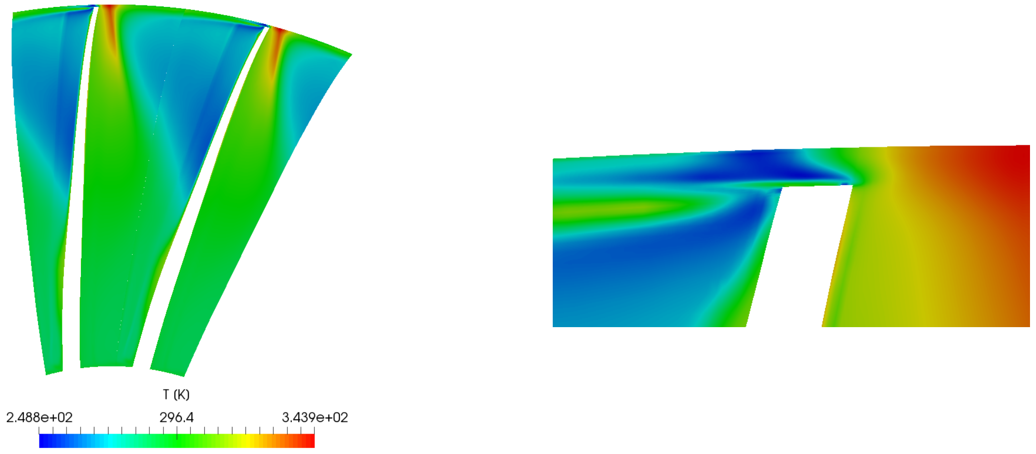

(a) Temperature field.

(b) Detail of the temperature field in the tip-gap.

Figure 79: Temperature field representation at the axial cross-section 3 for the near-stall operating point.

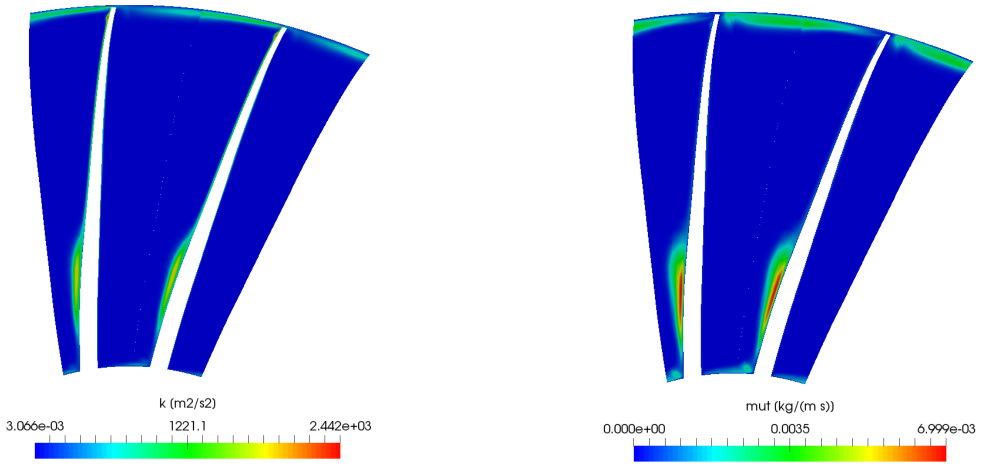

(a) Turbulent kinetic energy.

(b) Turbulent viscosity.

Figure 80: Turbulent kinetic energy and turbulent viscosity field representation at the axial cross-section 3 for the near-stall operating point.

Figures (81) and (82) show the details of Mach number and relative Mach number field in the tip-gap of the axial cross-section 3 for the near-stall operating point. Figure (82) additionally presents the relative velocity vectors in the tip-gap in order to visualise a tip-leakage flow from pressure to the suction side of a rotor blade.

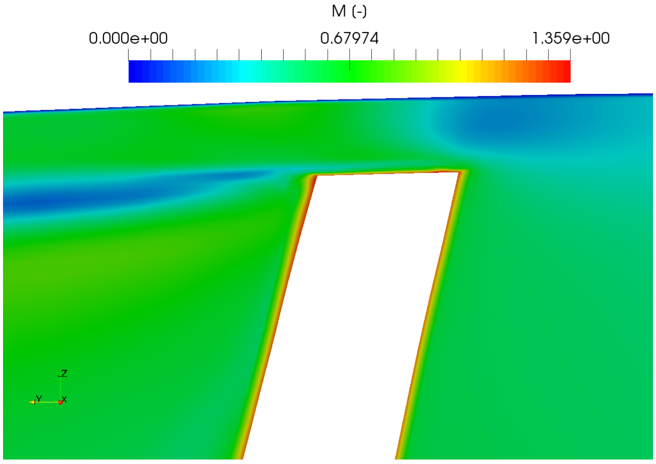

Figure 81: Details of Mach number field at the axial cross-section 3 for the near-stall operating point.

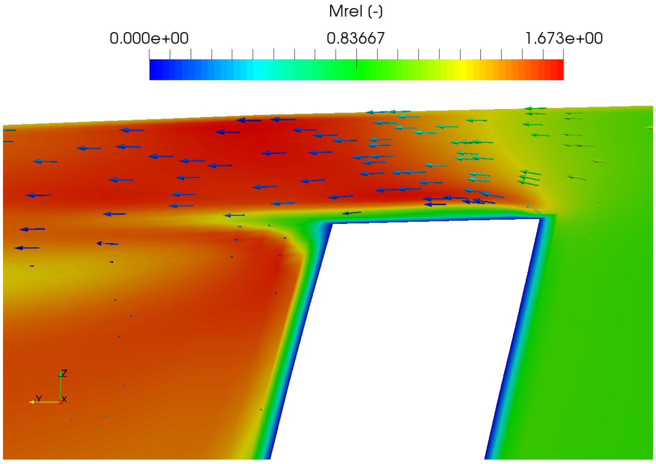

Figure 82: Details of relative Mach number field and relative velocity vectors at the axial cross-section 3 for the near-stall operating point.

- **Axial cross-section 4** (presented on Figure (15))

The following Figures (83 - 86) present profiles of pressure, velocity, temperature, turbulent kinetic energy and turbulent viscosity field at the cross-section in the middle of the rotor blade passage, respectively. Pressure field presented at the Figure (83a) nicely captures the pressure distribution in the blade passage, whereas high pressure region dominates in the considered cross-section. Higher pressure values at the upper part of the rotor blade pressure side influence the whole pressure distribution in the blade passage, while the low pressure region is located only locally at the upper part of the rotor blade suction side.

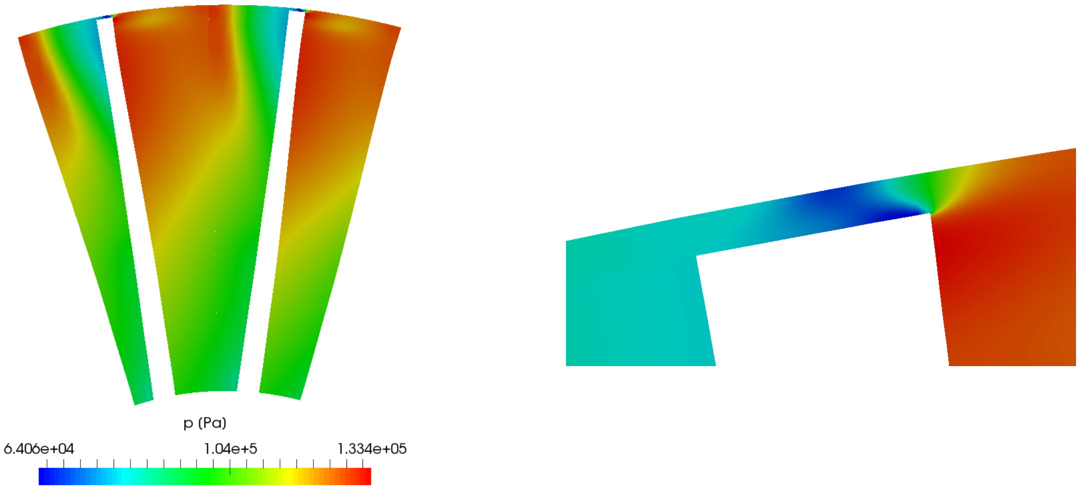

(a) Pressure field.

(b) Detail of the pressure field in the tip-gap.

Figure 83: Pressure field representation at the axial cross-section 4 for the near-stall operating point.

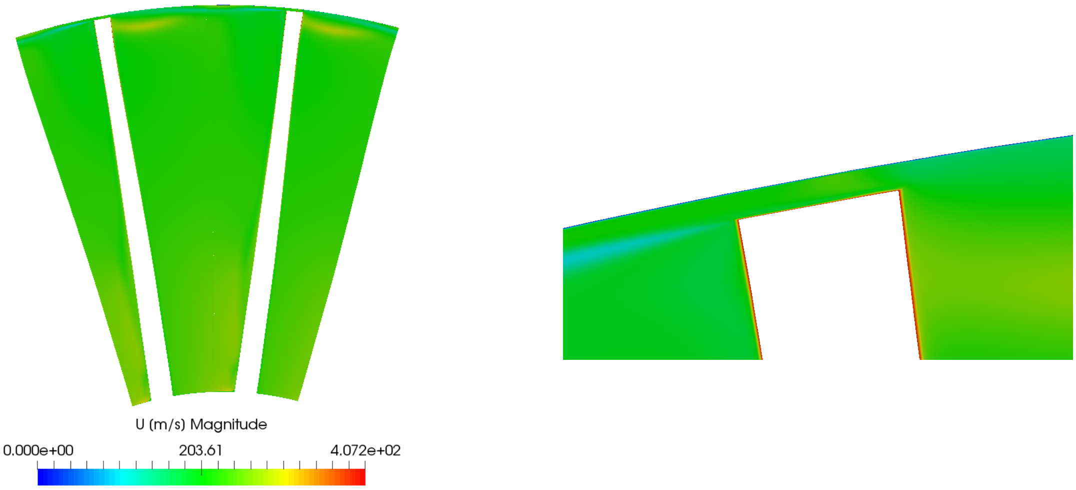

(a) Velocity field.

(b) Detail of the velocity field in the tip-gap.

Figure 84: Velocity field representation at the axial cross-section 4 for the near-stall operating point.

The tip-gap pressure field detail is presented in the Figure (83b). It can be seen that large pressure gradients are located at the blade tip, which cause more abundant tip-leakage flow compared to the tip-leakage flow for the peak-efficiency operating point. Figure (85b) presents the temperature field at the axial cross-section at the middle of a blade passage. It can be observed that the high temperature region is located only locally in the vicinity of a blade tip on the pressure side of a rotor blade. Figure (86a) presents turbulent kinetic energy and turbulent viscosity field and it nicely shows a tip-leakage flow. High values are present near the pressure side blade-tip, which are a source of localised high temperature field shown in Figure (85).

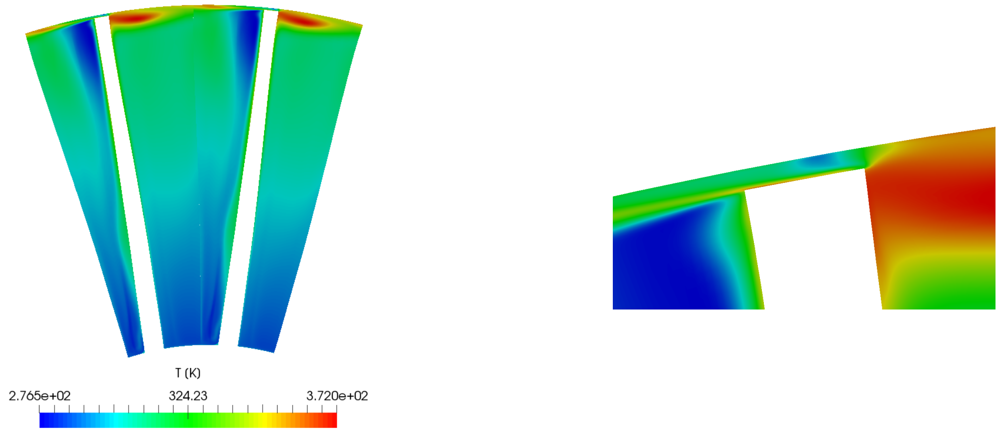

(a) Temperature field. **(b)** Detail of the temperature field in the tip-gap.

Figure 85: Temperature field representation at the axial cross-section 4 for the near-stall operating point.

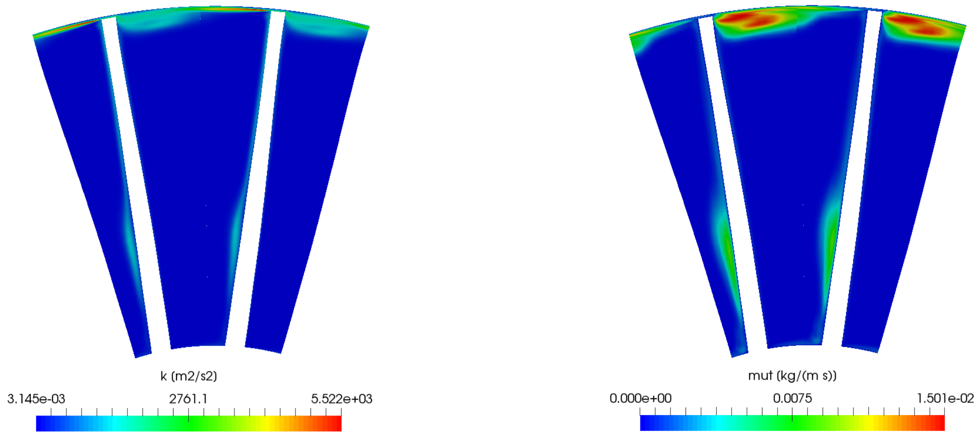

(a) Turbulent kinetic energy. **(b)** Turbulent viscosity.

Figure 86: Turbulent kinetic energy and turbulent viscosity field representation at the axial cross-section 4 for the near-stall operating point.

Figures (87) and (88) show the details of Mach number and relative Mach number field in the tip-gap of the axial cross-section 3 for the near-stall operating point. Figure (88) additionally presents the relative velocity vectors in the tip-gap in order to visualise a tip-leakage flow from pressure to the suction side of a rotor blade.

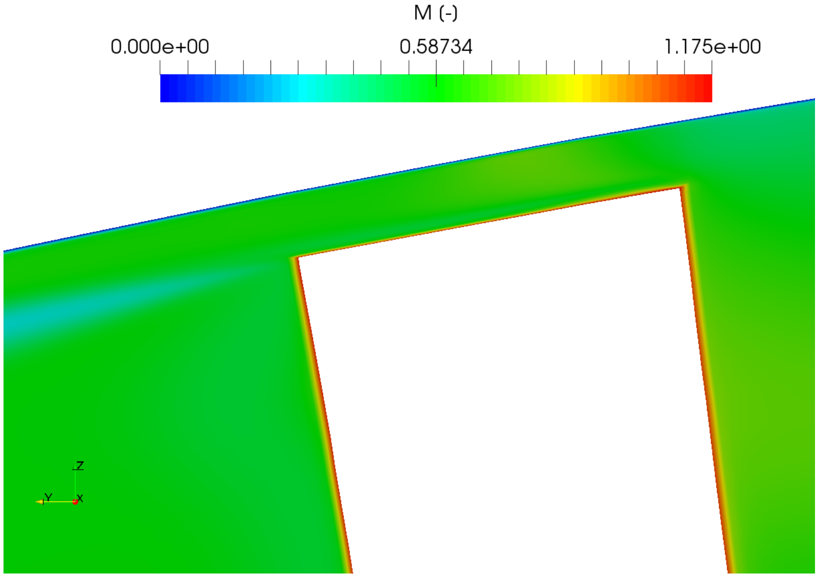

Figure 87: Details of Mach number field at the axial cross-section 4 for the near-stall operating point.

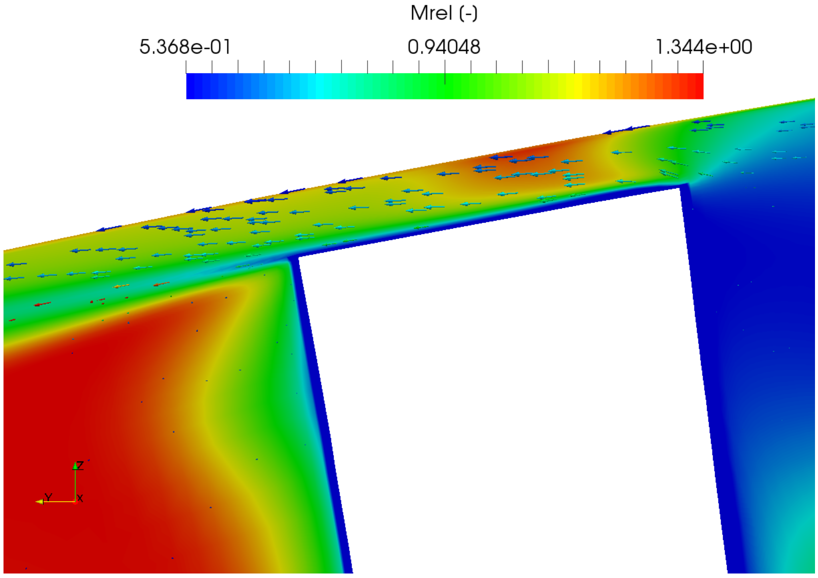

Figure 88: Details of relative Mach number field and relative velocity vectors at the axial cross-section 4 for the near-stall operating point.

- **Axial cross-section 5** (presented on Figure (15))

The following Figures (89 - 92) present profiles of pressure, velocity, temperature, turbulent kinetic energy and turbulent viscosity field at the cross-section 5, respectively. The majority of fields are presented alongside with the fluid flow detail at the tip-gap. Low pressure region is located at the lower part of the rotor blade suction side, at the rotor blade-hub junction.

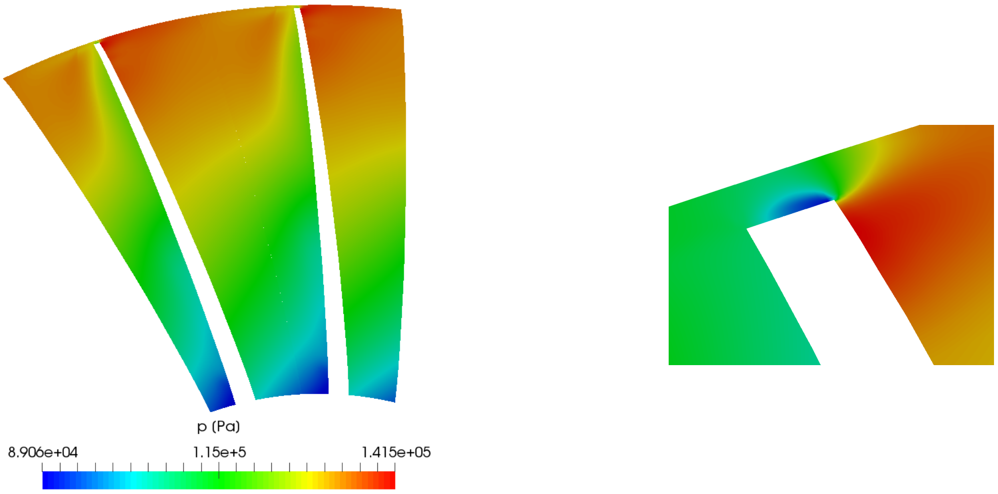

(a) Pressure field. **(b)** Detail of the pressure field in the tip-gap.

Figure 89: Pressure field representation at the axial cross-section 5 for the near-stall operating point.

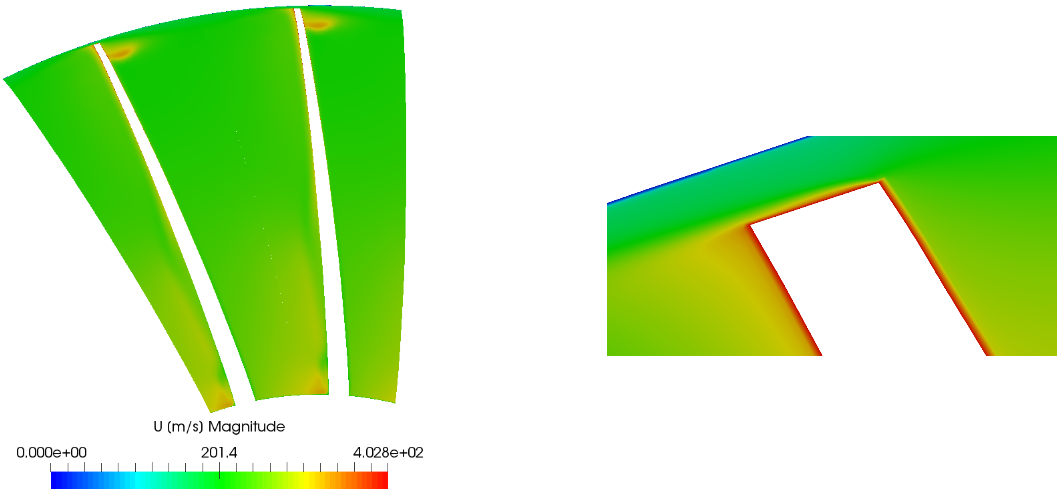

(a) Velocity field. **(b)** Detail of the velocity field in the tip-gap.

Figure 90: Velocity field representation at the axial cross-section 5 for the near-stall operating point.

The tip-gap pressure field detail is presented in the Figure (89b). The figure shows high pressure gradients located at the blade tip, which cause a tip-leakage flow. Low pressure region at the tip-gap is nicely captured. Figure (91b) shows the temperature field at the axial cross-section 5. High temperature region is located in the vicinity of a blade tip on the pressure side of a rotor blade. Figure (92a) presents turbulent kinetic energy and turbulent viscosity field and it nicely shows a tip-leakage flow. High values are present near the pressure side blade-tip, which are a source of localised high temperature field shown in Figure (91).

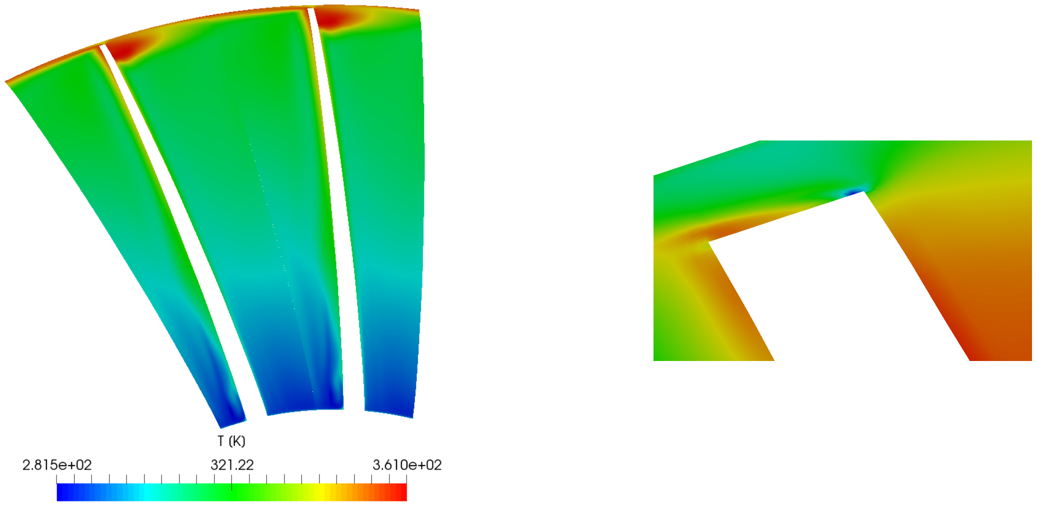

(a) Temperature field. **(b)** Detail of the temperature field in the tip-gap.

Figure 91: Temperature field representation at the axial cross-section 5 for the near-stall operating point.

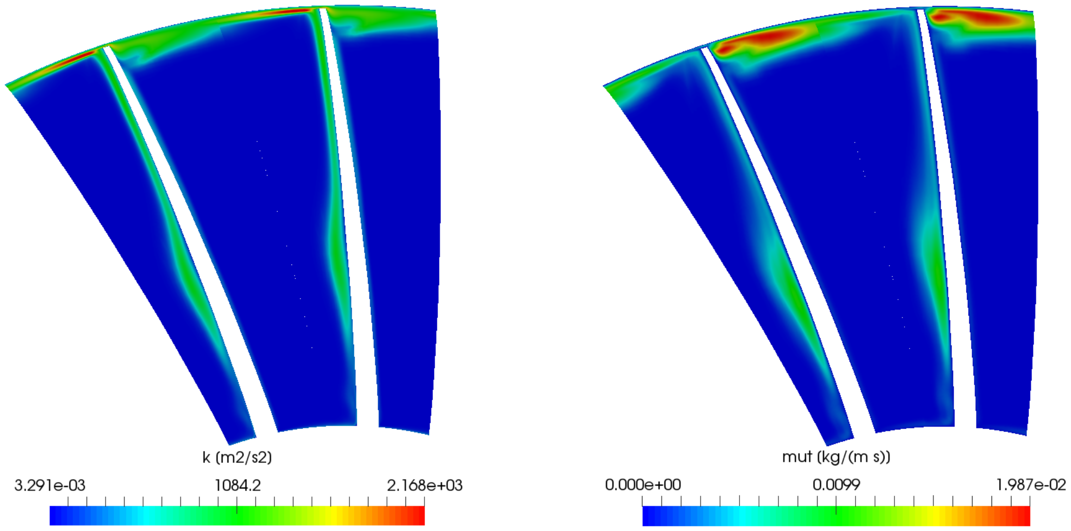

(a) Turbulent kinetic energy. **(b)** Turbulent viscosity.

Figure 92: Turbulent kinetic energy and turbulent viscosity field representation at the axial cross-section 5 for the near-stall operating point.

Figures (93) and (94) show the details of Mach number and relative Mach number field in the tip-gap of the axial cross-section 3 for the near-stall operating point. Figure (94) additionally presents the relative velocity vectors in the tip-gap in order to visualise a tip-leakage flow from pressure to the suction side of a rotor blade.

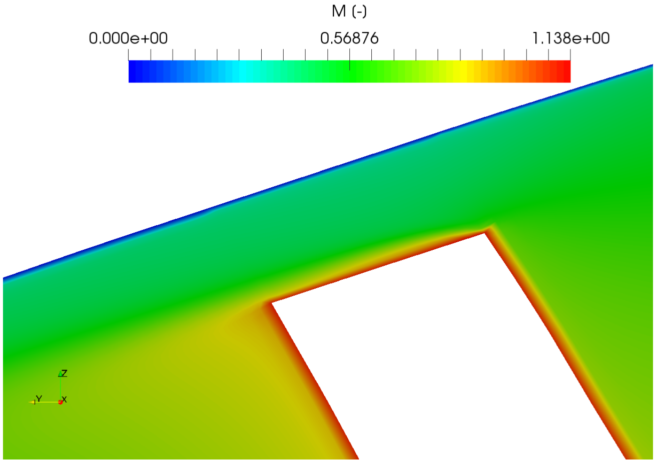

Figure 93: Details of Mach number field at the axial cross-section 5 for the near-stall operating point.

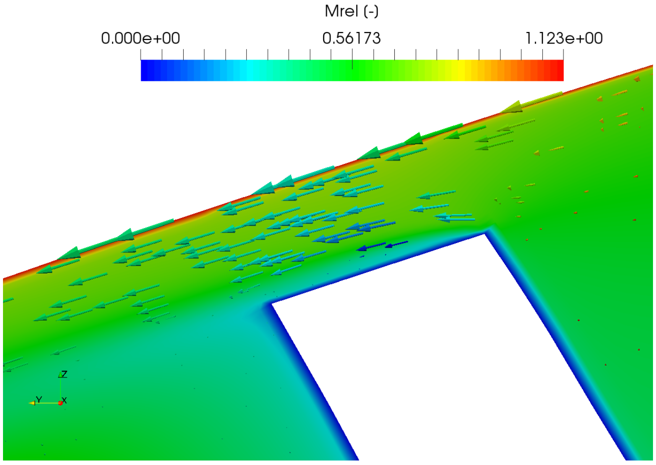

Figure 94: Details of relative Mach number field and relative velocity vectors at the axial cross-section 5 for the near-stall operating point.

Pressure distribution at the each side of rotor blade is presented in Figure (95). Pressure difference between pressure side and suction side for the near-stall operating point is greater than the corresponding pressure difference for the near-peak efficiency operating point presented in Figure (53).

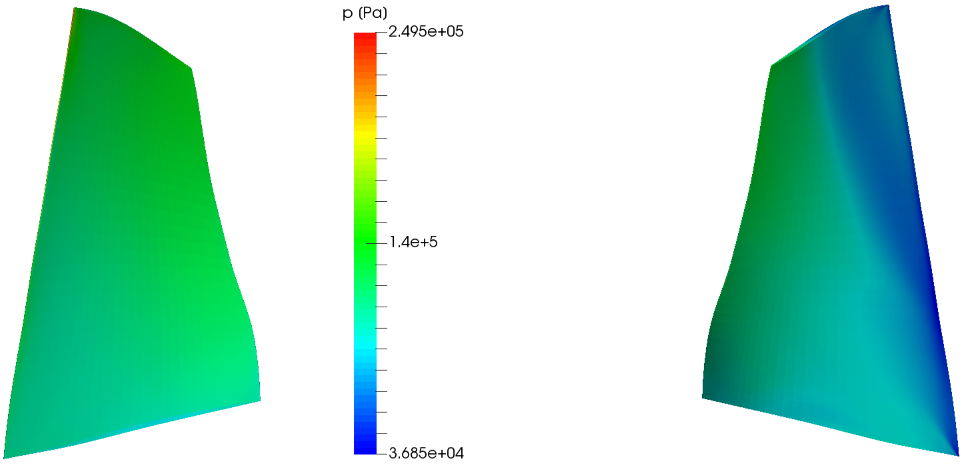

(a) Pressure side. **(b)** Suction side.

Figure 95: Pressure distribution at the rotor blade for the near-stall operating point.

Figure (96) shows a tip-gap leakage flow alongside with the vortex shedding visualised by streamlines, while the Figure (99) shows a trailing edge vortex shedding visualised by streamlines.

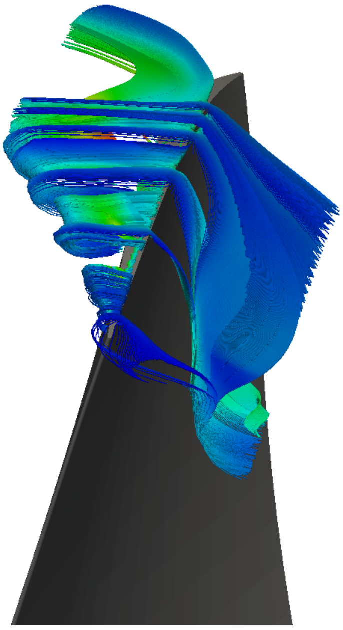

Figure 96: Tip-leakage flow and tip-gap vortex shedding visualised by streamlines at the near-stall operating point.

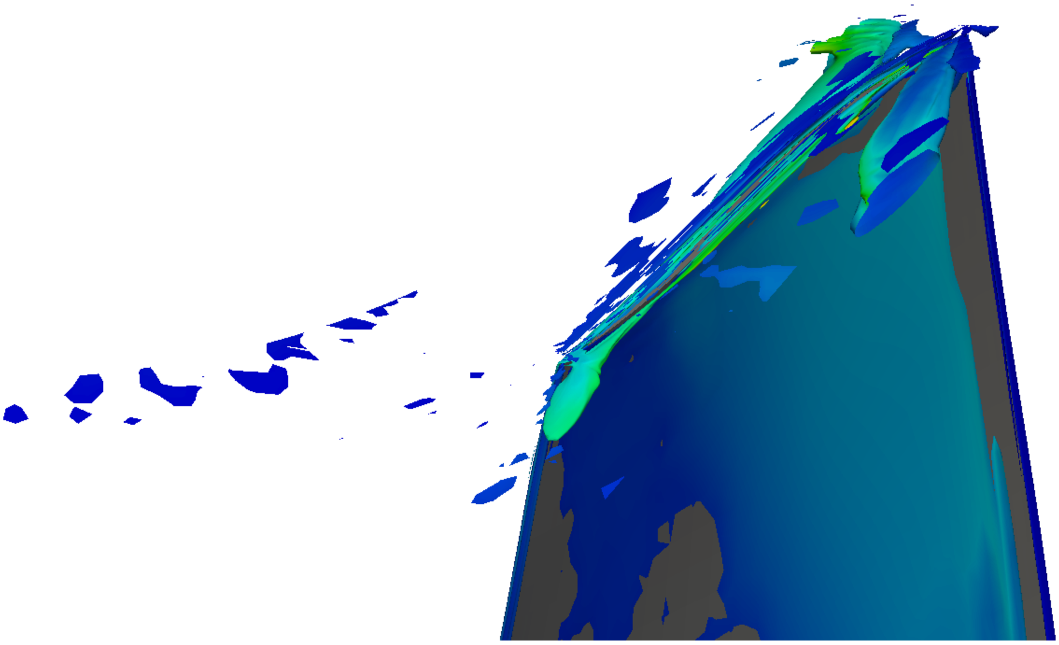

Figure 97: Tip-gap vortex visualisation via Q-contour for the near-stall operating point.

Figure (98) shows the root vortex at the rotor blade trailing edge for the near-stall operating point visualised by streamlines.

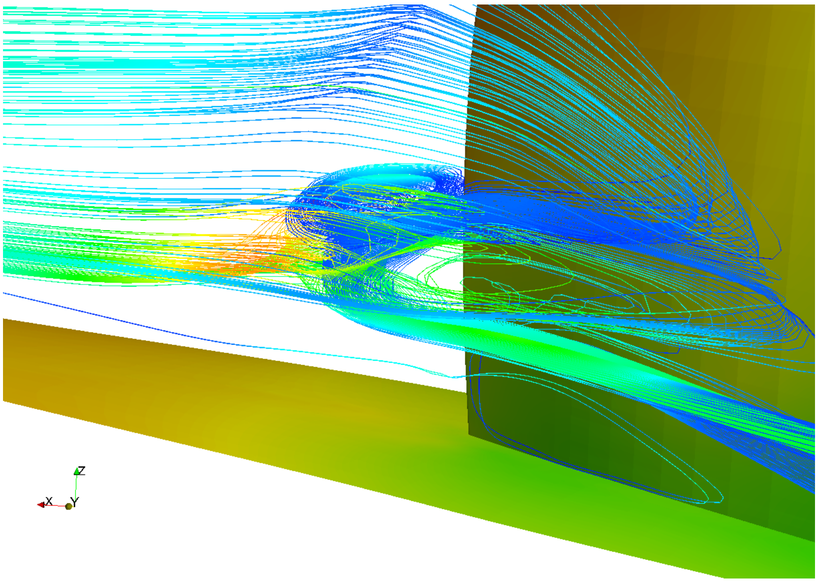

Figure 98: Vortex shedding at the trailing edge of a rotor blade visualised by streamlines for the near-stall operating point.

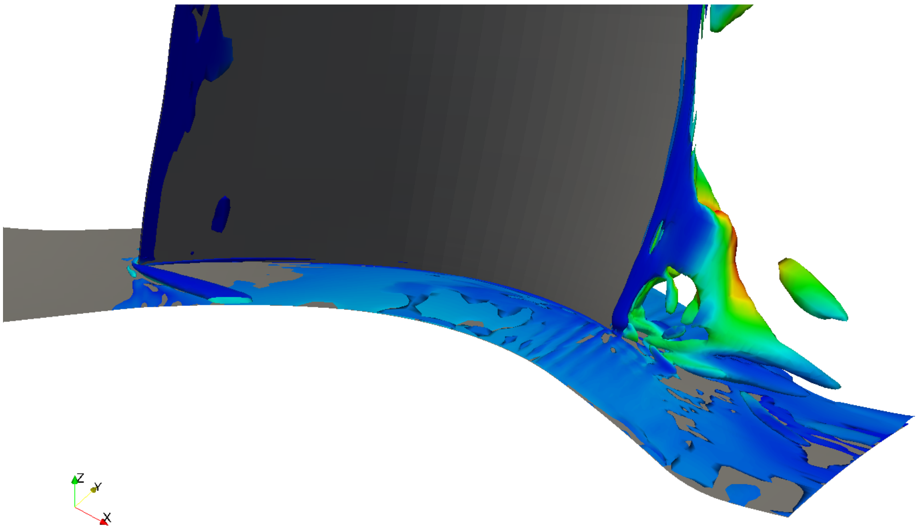

Figure 99: Vortex shedding at the trailing edge of a rotor blade visualised via Q-contour at the near-stall operating point.

Finally, after presenting all significant fluid flow distributions at various cross-sections of the numerical domain for the near-stall operating point, overall performance of the NASA Rotor 67 turbofan can be presented. Thus, the achieved mass flow rate $\dot{m}$ equals 32,23 kg/s, while the obtained total pressure ratio Π is 1,6675. The overall obtained adiabatic efficiency η_{ad} of the NASA Rotor 67 turbofan is 88,49%. Results are summarized in tabular form and presented in Table (9).

Table 9: Overall performance of the NASA Rotor 67 turbofan at the near-stall operating point.

Parameter	Value	Experiment	Error	Relative Error, [%]
Mass flow rate, $\dot{m}$	32,23 kg/s	32,305 kg/s	0,075 kg/s	-0,23
Total pressure ratio, Π	1,6675	1,728	0,0605	3,5
Fan torque, T_{F}	44,7 N m	/	/	/
Axial force, F	-193,3 N	/	/	/
Power, P	75 100 W	/	/	/
Adiabatic efficiency, η_{ad}	88,49%	90,1%	1,61%	1,79

Compared to the experimental data for the near-stall operating point for NASA Rotor 67 [1], obtained numerical performance data is slightly different. There is a good agreement between numerical and experimental data for the mass flow rate, while the calculated total pressure ratio is slightly underestimated according to the experimental data. Since the relative error between calculated and experimental value of total pressure ratio is less than 5%, numerical results are considered satisfactory and acceptable.

5.4.1 Closure

Numerical results of the fluid flow inside the NASA Rotor 67 turbofan at the near-stall operating point were presented within this subsection. Results were presented at various cross-sections of the numerical domain and for various physical quantities. Obtained results were compared to the experiment [1] by means of relative Mach number contours. Presented relative Mach number contours are in agreement with the experiment. Details of the fluid flow in the tip-gap were also presented. Visualisation of the tip-gap flow and tip-gap vortex were presented by streamlines and by Q-contours. Trailing edge vortex was captured and presented by Q-contours likewise. Obtained overall aerodynamic performance of the NASA Rotor 67 axial-flow turbofan was presented in tabular form.

5.5 Evaluation of Performance Curve

Within the previous Subsections (5.3) and (5.4), fluid flow details and overall aerodynamic performance of the NASA Rotor 67 turbofan for two operating points were presented. First one was near-peak efficiency operating point, while the other was located near stall. In addition to numerical results presented for these operating points (Tables (9) and (8)), a number of numerical simulations were carried out in order to assemble a single fan performance curve for a nominal angular velocity. The performance curve represents a total pressure ratio of a turbofan as a function of a mass flow rate. Evaluated perfomance curve for the NASA Rotor 67 axial-flow turbofan is presented in Figure (100). Efficiency characteristic is presented on the same figure likewise.

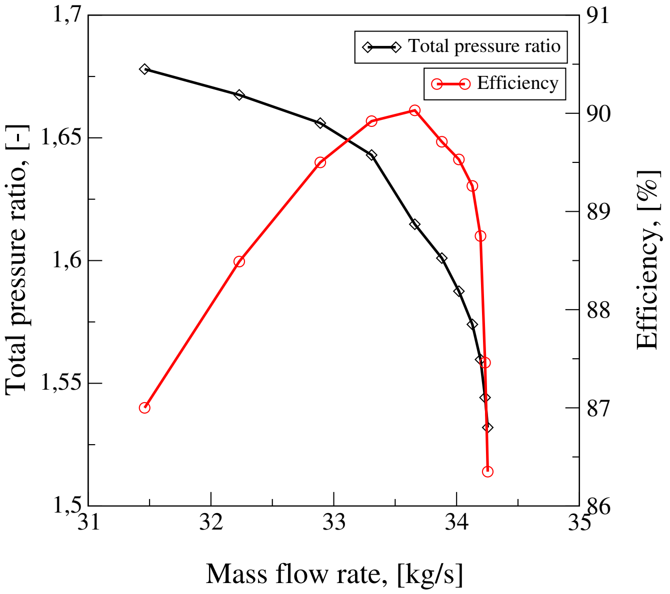

Figure 100: Performance curve of the NASA Rotor 67 turbofan.

According to the Tables (8) and (9) and Figure (100), the operating point near pear efficiency is characterised by mass flow rate for which the efficiency curve reaches the peak. Near-stall operating point is the leftmost operating point on the performance curve. The third characteristic point on the performance curve is the choke point, which is the rightmost point of the given characteristic. NASA Rotor 67 turbofan achieves a total pressure ratio of 1,532 for the mass flow rate of 34,254 kg/s in a choke point.

In order to compare evaluated performance curve of the NASA Rotor 67 turbofan with the perfomance curve obtained by experiment [1], a normalised performance curve was plotted. Performance curve was normalised according to the choke mass flow rate from the experiment, which equals 34,96 kg/s. Comparison of the evaluated performance curve with the experiment is presented in Figure (101).

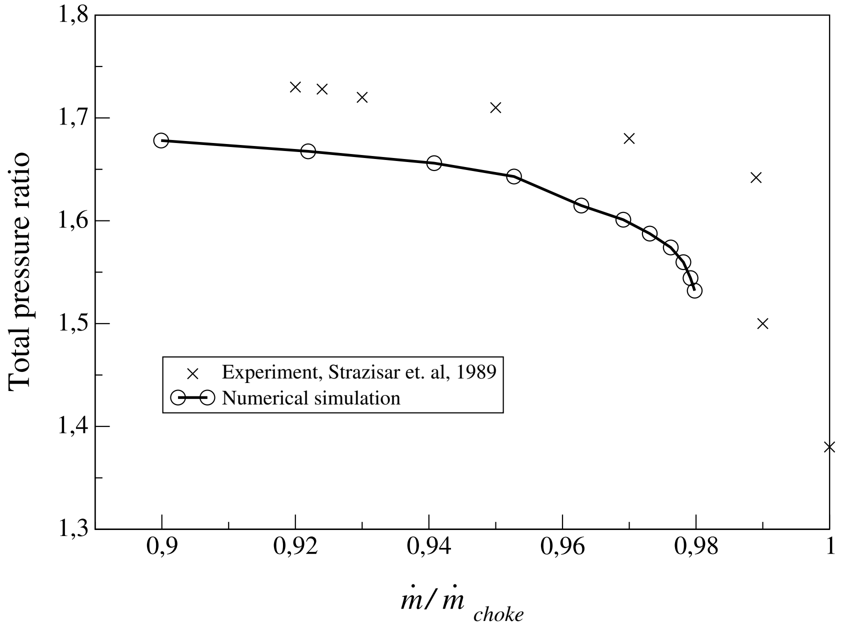

Figure 101: Comparison of the evaluated turbofan performance curve with the experiment.

According to the Figure (101), two performance curves do not overlap, but are relatively close to each other. Therefore, results presented within this thesis appear to be reasonable and accurate enough for a CFD numerical simulation which involves complex physics such as compressible, turbulent and transonic flow inside of turbomachinery.

5.6 Closure

Numerical results of fluid flow inside the NASA Rotor 67 turbofan for two operating points were presented within this section. First, distribution of various fluid flow quantities were presented for a near-peak efficiency operating point and their overall aerodynamic performance data was obtained and presented in tabular form. The near-stall operating point was analysed in the same manner. Tip-leakage flow and tip-vortex were visualised by streamlines and Q-contours. Trailing edge vortex was visualised by Q-contours likewise. Numerical results were compared to the experiment by means of relative Mach number contour plots which indicated a high level of agreement. In addition to the presented operating points, more numerical simulations were carried out by varying the outlet pressure distribution in order to assemble a performance curve for the nominal angular velocity. Generated performance curve was presented along with the efficiency curve. Additionally, a normalised performance curve was plotted with respect to the choke mass flow rate stated in the literature. Therefore, evaluated NASA Rotor 67 performance curve is compared to the the performance curve presented in [1]. Normalised performance curve comparison shows that experimental and numerical curves share the same trend, and that results of numerical simulations were reasonably accurate. Therefore, a newly implemented numerical code within the `foam-extend` CFD package is capable for solving complex physics of transonic fluid flow.

6 Conclusion

This thesis presents the use of newly implemented numerical solver within the CFD package `foam-extend` in order to solve a complex transonic flow inside the turbomachinery. The new formulation of compressible flow solver that uses rothalpy as a conservative quantity in energy conservation equation is tested on a standard test case for compressible, turbulent and transonic flow inside turbomachinery - the NASA Rotor 67 axial-flow turbofan.

In order to perform numerical simulations of fluid flow inside the NASA Rotor 67, a case needs to be prepared by means of geometry and numerical mesh generation. Due to repeating geometry patterns, the geometry and numerical mesh were generated for a single blade passage in order to reduce the computational cost.

Numerical simulations were carried out for many operating points, with the near-peak efficiency and near-stall operating points examined in details. Numerical simulation results for the near-peak efficiency and near-stall operating points were presented at various radial and axial-cross sections of the numerical domain for various physical quantities of interest. Obtained numerical results were compared to the experimental results by means of relative Mach number contour plots at 10%, 30% and 70% span. Since the geometry of NASA Rotor 67 axial-flow fan produces a tip-gap vortex and trailing edge vortex, they were visualised in appropriate way. Therefore, the tip-gap vortex along with the tip-leakage flow were presented by streamlines, while the trailing edge vortex was visualised by Q-contours. Overall aerodynamic performance data in terms of mass flow rate, total pressure ratio, adiabatic efficiency, power, torque and axial force were presented in tabular form for near-peak efficiency and near-stall operating points.

Obtained numerical performance data for NASA Rotor 67 turbofan at various operating points were used in order to assemble a performance curve for the nominal angular velocity. Assembled performance curve was normalised according to the choke mass flow rate and compared to the normalised performance curve presented in the literature [1]. Evaluated performance curve does not significantly differ from the experiment. Regarding the relative Mach number contour plots, they show good agreement with the corresponding experimental data. Therefore, a new compressible solver has proven to be reasonably accurate and capable of solving extremely complex physics such as compressible, turbulent and transonic flow inside turbomachinery.

References

[1] Strazisar, A.J., Wood, J.R., Hathaway, M.D., Suder, K.L., “Laser Anemometer Measurements in a Transonic Axial-Flow Fan Rotor,” NASA Technical Paper 2879, Lewis Research Center, Cleveland, Ohio, 1989.

[2] Versteeg, H.K., Malalasekera, W., “An Introduction to Computational Fluid Dynamics,” Second Edition, 2007.

[3] Dixon, S.L., Hall, C.A., “Fluid Mechanics and Thermodynamics of Turbomachinery,” Seventh Edition, 2014.

[4] Day, I.J., “Stall, Surge and 75 Years of Research,” ASME, Journal of Turbomachinery, 2015.

[5] Jasak, H., “Numerical Solution Algorithms for Compressible Flows,” Lecture Notes, 2007.

[6] Lyman, F. A., “On the Conservation of Rothalpy in Turbomachines,” ASME, Journal of Turbomachinery, 1993.

[7] “foam-extend project,” `https://sourceforge.net/projects/foam-extend/`, last access 14.1.2017.

[8] “See the MRF development,” `http://openfoamwiki.net/index.php/See_the_MRF_development`, 2009., last access 8.2.2017.

[9] Beaudoin M., Jasak H., “Development of a Generalized Grid Interface for Turbomachinery simulations with OpenFOAM,” Open Source CFD International Conference, Berlin, Germany, 2008.

[10] Jasak, H., “Error analysis and estimation for the Finite Volume Method with applications to fluid flows,” PhD Thesis, Imperial College of Science, Technology and Medicine, London, 1996.

[11] De Dominicis, I., Cvijetić, G., Willetts, M., Jasak, H., “Enhanced Turbomachinery Capabilities for foam-extend: Development and Validation,” 11th OpenFOAM Workshop, Guimarães, Portugal, 2016.

[12] “CFD Online,” `https://www.cfd-online.com/Wiki/Favre_averaging`, 2013., last access 9.2.2017.

[13] Wilcox, D.C., “Turbulence Modelling for CFD,” DCW Industries Incorporated, 1994.

[14] Menter, F. R., "Two-equation eddy-viscosity turbulence models for engineering applications," AIAA Journal, 1993.

[15] Robert Keser, "Block-Coupled Solution Algorithms for 2-equation Turbulence Models," Master's Thesis, Faculty of Mechanical Engineering and Naval Architecture, 2016.

[16] Beaudoin M., Jasak H., "OpenFOAM TURBO TOOLS: FROM GENERAL PURPOSE CFD TO TURBOMACHINERY SIMULATIONS," ASME-JSME-KSME 2011 Joint Fluids Engineering Conference, Hamamatsu, Japan, 2011.

[17] ANSYS, "ANSYS Fluent Theory Guide," Release 14.0, November, 2011.

[18] "Sig Turbomachinery MRF Library," `https://openfoamwiki.net/index.php/Sig_Turbomachinery_MRF_Library`, 2010., last access 8.2.2017.

[19] "SolidWorks 2016," `http://www.solidworks.com/`, 2016., last access 8.2.2017.

[20] "Pointwise V18.0R1 Release Notes," `http://www.pointwise.com/support/release-notes.shtml`, 2016., last access 8.2.2017.